



PhD's thesis XXX Cycle

ICE STRUCTURES INSIDE SINGLE WALL CARBON NANOTUBES

A Molecular Dynamics Simulation Study

Pietro Pugliese

Supervisors: Paola Gallo and Maria Martin Conde
Department of Mathematics and Physics
Università degli Studi Roma Tre
Rome, Italy 2017

Contents

Introduction	3
1 Physic of Water	7
1.1 The water molecule	7
1.2 The Anomalous Properties of Water	10
1.3 Supercooled water	18
2 Ice Phases	24
2.1 Ice I_h and Ice XI, the Issue of Proton Ordering	26
2.2 Pauling Entropy	28
2.3 Other Ice Forms	29
3 Molecular Dynamics Simulations	31
3.1 Classical Molecular Dynamic Simulations	31
3.2 Integrate the equations of motion	35
3.3 Thermostats and Barostats	40
3.4 Force fields and Potentials	41
3.5 Ewald summation	43
3.6 The TIP4P/ICE	45
4 L-S Transition Inside SWCNT	48
4.1 Pure Water: Setup of the Simulation	48
4.2 Crystallization of water inside the SWCNT	53
4.3 Analysis of the Freezing Temperatures	58
4.4 Conclusions	60
5 Structure of Ice Nanotube	61
5.1 Distribution of water molecules insde the SWCNT	61
5.2 Ice Nanotube	65
5.3 Proton Ordering	69
5.4 Conclusion	74

<i>CONTENTS</i>	2
6 Ionic Solutions	75
6.1 Simulation Details	75
6.2 Modifications of The Water Structure	76
6.3 Hydration of Ions and Short Range Order	78
7 Confined Aqueous Solutions	82
7.1 NaCl Solutions: Simulation Setup	82
7.2 NaCl Solutions: Results	86
7.3 Methane Solutions: Simulation Setup	89
7.4 Methane Solutions: Results	93
7.5 Conclusion	95
8 Conclusions and Future Outlooks	96
A List of Activities	100

Introduction

Water is the most important liquid present on our planet. It plays a fundamental role in both geological and chemical processes [1] and it is also essential for life [2]. Even if we are familiar with this liquid in our every day life we have not completely understood its properties from a scientific point of view. This is a liquid as important as it is mysterious.

There are more than 60 known anomalies in the water behavior [3, 4]. These anomalies concern its phase, its density, its structure, its thermodynamics and its dynamics and they are encountered over all its puzzling phase diagram. All this anomalies probably come from the capability of water molecule to form hydrogen bonds. Nowadays the study of the water is one of the most interesting field in physics. A huge amount of theoretical, computational and experimental works [1, 3, 4] have been carried out to understand the phase diagram and the peculiar properties of water.

Since most of the liquid water anomalies arise upon cooling when the temperature is near or below to the freezing temperature, an explanation to the anomalies of water can be found in the so called supercooled regime. Water is in the super cooled regime when it is in the liquid state but below the freezing temperature. The supercooled condition is obviously a metastable state. This regime can be achieved with an accurate setup of the experiment, but there are experimental limits that prevent us from going down in temperature at will. This region of the phase space in which is not possible to observe liquid water, in a metastable state, it known as “no man’s land”. However this limit is not due to thermodynamic constraints [4], the homogeneous nucleation is in fact a kinetic constraint and it is function of the cooling rate and of the observation time. This means that in the future it will be possible investigate the no man’s land.

Due to the difficulties of experiments, molecular dynamics simulation are often use in the study of the liquid phase of water upon supercooling and it is possible to investigate the no man’s land. Rahman and Stillinger in the 1971 performed the first molecular dynamics simulation of liquid water [5]. Starting from that first work the contribution of the simulation was crucial

to the development of our knowledge in this field.

In many relevant phenomena in different fields like geology and biology water is confined in different environments. The behavior of water in contact with hydrophilic or hydrophobic surfaces is central in many studies of biological and geological systems. Therefore the study of confined water is an issue of wide interest as it allows us not only to investigate the general properties of water [6, 7] but it also has applicative purposes [8]. Moreover the confinement can prevent the crystallization and make possible to study the no man's land.

The studies of water solution are also very relevant in the understanding of biological and chemical systems. The investigation of aqueous solutions can help to shed light on the numerous mysteries of bulk water. In fact the presence of solutes in water is known to affect thermodynamic quantities such as the boiling point, the freezing point and the vapor-liquid critical point [?, ?, ?]. Solutions of electrolytes are more easily supercooled than bulk water, as the temperature of homogeneous nucleation shifts downward upon increasing the solutes content [?].

Among confining structures carbon nanotubes (CNTs) have attracted in recent times a great interest due to their fascinating properties that made them potentially useful in a wide variety of applications. These cylindrical nanostructures are formed by one or more layers of graphene. Among the numerous applications [9] are the use of CNTs in electronic devices [10] and their usage in Biology and Medicine [11, 12]. There are also a considerable number of applications connected to water. For example, the study of the water flow through atomic smooth surface of a carbon nanotubes [13] and its enhancement found by both theoretical calculations [14] and experiments [15], or the study of membranes made by carbon nanotubes that can be also used as filter in desalination mechanisms for different solutions like the NaCl aqueous solution [16, 17].

Water can fill the space inside a single walled carbon nanotube (SWCNT) [18, 19] and it was found both experimentally [20–22] and by simulation [23, 24] that it easily crystallizes. The water ordered structures that form inside the SWCNTs are called ice nanotubes [25].

Importantly and unexpectedly it was recently experimentally discovered by an MIT group [26] that water freezes already at boiling conditions inside the nanotube. Thus, the hydrated SWCNTs can be considered as possible candidates for the latent thermal storage in diverse systems [27].

The main theme in this PhD thesis is the study of confined water in SWCNT's, with particular focus on the structures of ice nanotubes. I performed molecular dynamics simulations using for water molecule, for the first time inside SWCNT, a very realistic potential: the TIP4P/ICE [28]. This

model was designed to study the solid phases of water and gives also the best overall ices phase diagram and the best predictions for the densities of several ice forms. Other molecular dynamics simulations on water in carbon nanotubes focusing on solid/liquid transition [23, 25] have used a model, TIP4P, that has a freezing temperature in the bulk phase 42.65 K lower than experimental bulk water at ambient pressure [29]. This inevitably leads also to a downward displacement of the freezing temperatures inside the carbon nanotubes.

I also studied aqueous solutions in this thesis. I participated to an analysis on anion hydration aqueous ionic solutions. Then I also performed two preliminary study on two other systems composed by a ionic aqueous solution of NaCl and an aqueous solution of methane in SWCNT. In the case of the sodium chloride we were interested to the possible inclusion of ions in the structure of ice nanotubes and more in general on the effect of the ions in the freezing. In the case of CH₄ our goal was to study the effect of a strong confinement in the process of hydrates formation. An hydrate is a water cage of water molecules that surrounds the methane and it usually forms under extreme condition of pressure.

This thesis is structured as follows.

In **Chapter 1** a general picture of the scientific background of our knowledge of the water physics is provided. In this chapter is illustrated how the structure of water is connected to its capability to form an hydrogen bond network. The central part of this chapter is dedicated to the water anomalies. In this section are presented the most known of the several anomalies of water as: the density anomaly, the behavior of the thermodynamic response functions and the anomaly of the diffusion coefficient. The last section is dedicated to the supercooled regime and is presented one of possible explanations of the anomalous behavior of water. This theory considers the presence of a liquid-liquid critical point in the no man's land.

In **Chapter 2** is presented an overview of the solid phase of water and the so called ice rules. The only two phases that will be illustrated in detail are the ice I_h and the ice XI, in order to present the issue of proton ordering that was crucial for our work. In the last section are presented the main characteristic of the sixteen ice forms that are actually known.

In **Chapter 3** I illustrate the methodology used in this work. Starting from the main elements of the molecular dynamic technique I enter in the details of the potentials used. The last section is dedicated to the TIP4P/ICE that is the water model that I used for our study.

The main argument of **Chapter 4** is the liquid solid transition of water inside SWCNT's. After a detailed discussion of the model used for the nanotube, describing the geometry and the potential used, the details of the

simulation are reported. We simulated the cooling process along the ambient pressure isobar of water confined in nanotubes of five different diameters. In the last part of this chapter we compare our results to the recent experimental result of the MIT group and the previous MD study.

Chapter 5 is about the analysis of the ice nanotubes structures. In the first part is illustrated how the ordering of water grows upon decreasing temperature. The structures of the ice nanotubes are discussed in the central part of this chapter where the theoretical structures of ice nanotubes are compared with the radial distribution function obtained in our simulations. Finally in the last section I discuss the issue of proton ordering that we found in the ice nanotube structure.

In **Chapter 6** it is reported an analysis done on the effect that ions solution have on bulk water. It is shown how the ions alter the radial distribution function of the water atoms. In this chapter it is also discussed the issue of the ions hydration.

In **Chapter 7** I discuss the simulation details and the preliminary results of our study of systems made by an NaCl ionic aqueous solution confined in a SWCNT. The simulation of solutions with two different concentration was designed according to the result presented in the previous chapters. The last part of this chapter deals with the simulation details and the results of our study on CH₄ and water solution confined in a SWCNT. Two systems made by nanotubes of different diameter and filled with an aqueous solution of methane are studied, the concentration of the methane in the solution was the same.

The **Last Chapter** contains the final remarks and general conclusions of the present Thesis. Possible outlooks are also outlined, especially on the Chapter 7 whose results are preliminary.

Chapter 1

Physic of Water

1.1 The water molecule

The water is composed by one oxygen and two hydrogens forming a planar v-shaped molecule. The two hydrogen atoms occupy the external vertices and one oxygen atom occupies the central vertex. The geometry of the molecule can be described using the value of the H–O–H angle and the O–H distance. In the gas phases the angle is 104.5° and the intramolecular distance is 0.957\AA [30, 31]. A schematic picture of the water molecule is shown in Figure 1.1

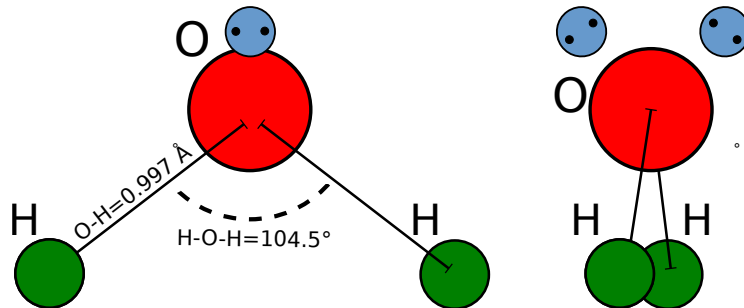


Figure 1.1: *Schematic picture of water molecule. On the left we can see a frontal view of the molecule in which are reported the experimental value of the HOH angle and the intramolecular distance OH. On the right it is possible to observe the position of the lone pairs of oxygen electrons. The position of the lone pairs arranges together with the two hydrogen atoms into a tetrahedral structure.*

There is a large electronegativity difference $\Delta\chi = 1.24$ between the oxygen and the hydrogens, this implies that the total electronic molecular distri-

bution is strongly condensed towards the oxygen atom [32]. This distribution of the charge in the water molecule and the mutual geometrical arrangement of the atoms make water a polar molecule with a dipole moment of 1.84 D in the vapour phase [33]. The valence electrons of the oxygen atom form two lone pairs that dispose together with the hydrogens in a tetrahedral structure, a sketch of this structure is reported in Fig. 1.1 .

The structure of water make this molecule capable to form the so called hydrogen bonds (HB) aligning one of his hydrogen with the lone pair of another water molecule. The formation of this kind of bond implies that the ionic character of the covalent O–H bond of the molecule decreases, and so the water molecule structure in the liquid phase is quite different with respect to the isolated molecule. The formation of the HBs is probably the most important feature of water and play an important role in both the liquid and the solid phase The energy associated at the formation of an HB (20 kJ/mol at ambient temperature) is higher than a typical intramolecular interaction, as the dipole-dipole van der Waals (1 kJ/mol). The HBs are strongly directional and tend to be aligned on the O–H \cdots O axis.

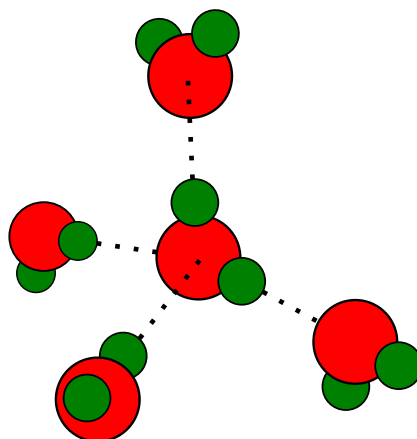


Figure 1.2: Picture of the tetrahedral hydrogen bond network that water locally forms, where the symbol \cdots indicates the HB formed by the two molecules.

When a water molecule forms an hydrogen bond then it is most likely that it forms other HBs with other water molecules. This cooperative nature of the HBs lead to the formation of a so called hydrogen bond network. A single molecule of water can form two bond as a donor and other two as acceptor for a total of four HBs. The HB network formed by the water molecules becomes more stable in the crystalline phases, with the typical tetrahedral symmetry

shown in Fig. 1.2 . The formation of HBs network is at the base of most of the peculiar properties showed by the liquid water that we discuss in the next section.

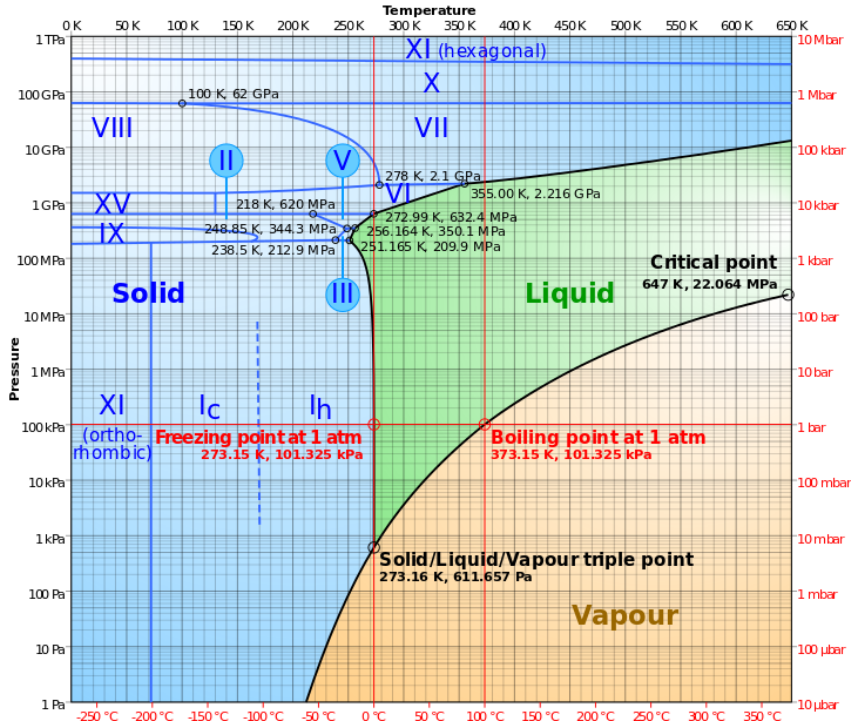


Figure 1.3: Phase diagram of the stable phases of water in the $P - T$ plane. Figure from Ref. [34].

In the Fig. 1.3 is showed the phase diagram of all the stable phases of water. The water at ambient conditions ($T \approx 298,15$ K and $P = 1$ bar) is stable only in the liquid phase. When the temperature drops below the 273 K at ambient pressure the HBs network becomes more stable and the water freezes in the ice phase known as I_h . We will discuss in the next section the difference between various ice phase, that can be found in the phase diagram, for now it is only important to underline that the ice I_h is the most common form of ice on the Earth. Conversely when the temperature is raised above 373 K the HBs are broken and the water becomes steam. this means that above this temperature water is stable in the only gas phase. If we look at the whole phase diagram we can see that is extremely complex. There are several triple points, besides solid-liquid-vapor one, due to the polymorphism of crystalline water. Indeed the hexagonal ring in the ice I_h is not the only configuration that water can assume in the solid phase. There are sixteen

different crystalline stable phases known up today, and each of them is stable in a certain p - T region. The peculiarities of water are not limited to the solid stable phases but extend over all the phase diagram, and include its metastable region as will see in the next section.

1.2 The Anomalous Properties of Water

Water exhibits several thermodynamic and dynamical anomalies [1, 4, 35, 36] A sketch of the main thermodynamic water anomalies is reported in Fig. 1.4 . In this figure is shown how the behaviour of water deviate from the one of a simple liquid. Each panel shows the temperature dependence at ambient pressure of different physical quantities: the density ρ , the isothermal compressibility κ_T , the coefficient of thermal expansion α_P and the isobaric specific heat c_P respectively.

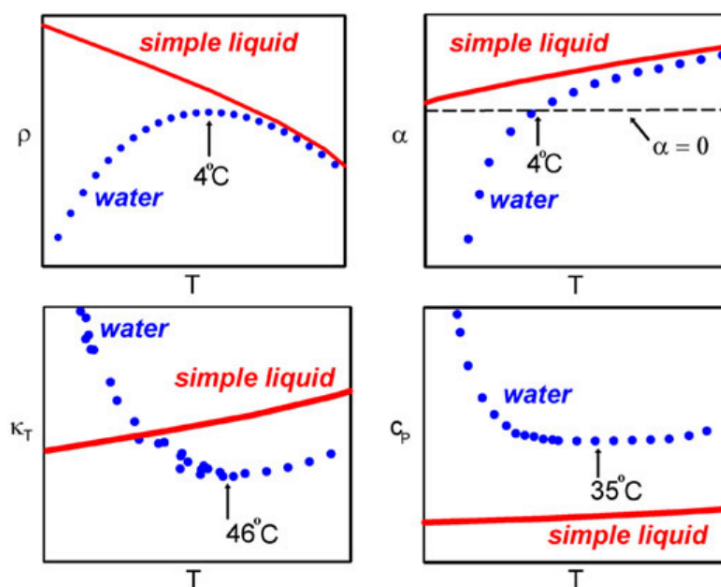


Figure 1.4: Comparison between water and a simple liquid for four different physical quantities at ambient pressure ($P = 1$ bar): density ρ (top left), thermal expansion coefficient α_P (top right), isothermal compressibility κ_T (bottom left) and isobaric heat capacity c_P . Figure from Ref. [1]

In Fig. 1.4 we can observe that the density ρ shows a maximum for $T = 4$ °C, this is probably the most know of the water anomalies. Whereas in a simple liquid the density increases upon decreasing temperature, the

behaviour of water is drastically different. Water in fact behaves as a simple liquid at high temperature than when the temperature decrease density exhibits a maximum is called temperature of maximum density (**TMD**). It is particularly interesting observe how the position of the **TMD** change on varying the pressure In Fig. 1.5 are reported the behaviour of the **TMD** for the SPC/E model (left panel) in the p - T palne and for the TIP4P model in the ρ - T palne (right panel). An interesting feature that can be observed is the change of curvature of the **TMD** line at negative pressures ($\rho < 1$). The **TMD** line shows a changing of curvature for negative pressures the same happen for the melting line. The origin of this reentrant behavior in the melting line is the higher compressibility of the liquid with respect to the solid phase [37, 38]. Fig. 1.5 suggest that there is a connection or relationship between the two line the **TMD** and the melting one. Notice that this particular behavior, of both the **TMD** and the liquid-ice I_h coexistence curve, is not a particular behavior of the SPC/EĤt has also been found in the TIP4P model [38, 39]demonstrating that is a general feature of water models and likely of real water. The **TMD** line marks the border between the region where water behaves as simple liquids and the region where the liquid anomalously expands on cooling.

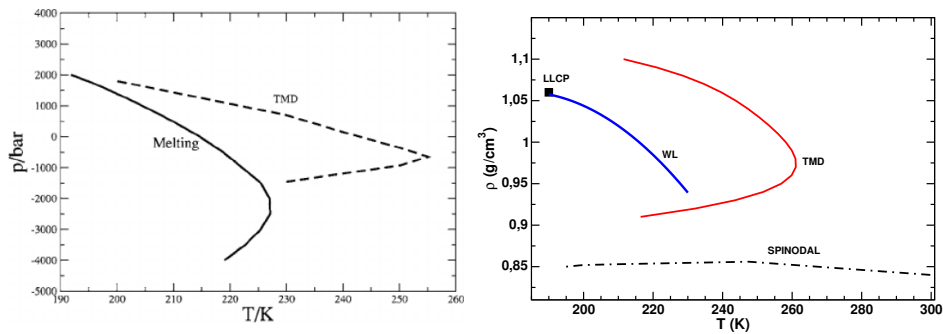


Figure 1.5: Behaviour **TMD** in the p - T plane for SPC/E model (left panel) and in the ρ - T palne (right panel). In the left panel is also reported the behavior of hte melting line. the right panle shows the behavior of the TMD line (red solid) the Widom Line (blue dolid) and the spinodal (black dot-dashed). Left panel figure from Ref. [40], the data of this figure was extrapolated by the Ref. [41]. Right panel figure from Ref. [?].

As a consequence of the presence of the **TMD** also the thermodynamic response functions show an anomalous behaviour. The thermal expansion

coefficient α_P for a fixed pressure P linearly depend from $\partial\rho/\partial T$

$$\alpha_P = \frac{1}{V} \left(\frac{\partial V}{\partial T} \right)_P = -\frac{1}{\rho} \left(\frac{\partial \rho}{\partial T} \right)_P,$$

consequently vanishes at the temperature of maximum density and becomes negative below it. Since for positive pressure the **TMD** is negatively sloped (see Fig. 1.5), the values of temperatures at which α_P vanish goes down upon compression of the system, as shown in Fig. 1.6

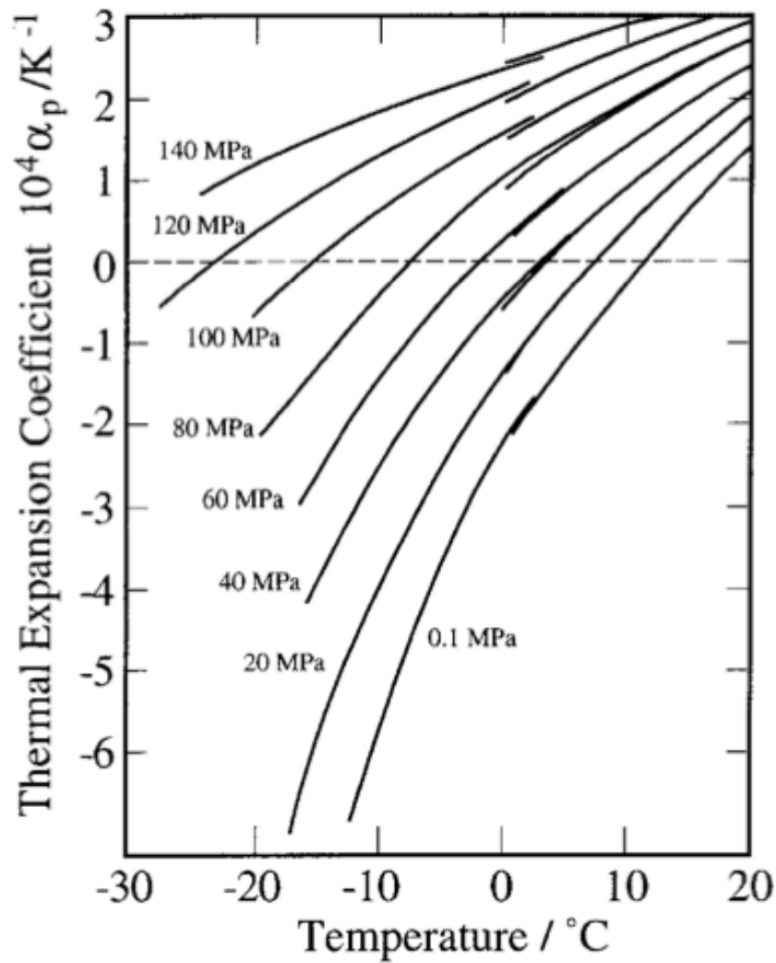


Figure 1.6: Behavior **TMD** in the P - T plane for SPC/E model. Figure from Ref. [40], the data of this figure was extrapolated by the Ref. [41]

Also for the the isothermal compressibility κ_T the behavior of water at high temperature is slightly decreasing upon cooling as in a simple liquid, .

Nevertheless, an abrupt and rapid increase of κ_T occurs when temperature became lower than $T = 46^\circ\text{C}$ and the behaviour of the isothermal compressibility strongly deviates from the monotonic decrease (see Fig. 1.4 bottom left). Upon increasing pressure the minimum in the isothermal compressibility moves towards lower temperatures as shown to see in the Fig. 1.7, where the experimental behaviour of the κ_T at several pressures is reported [42].

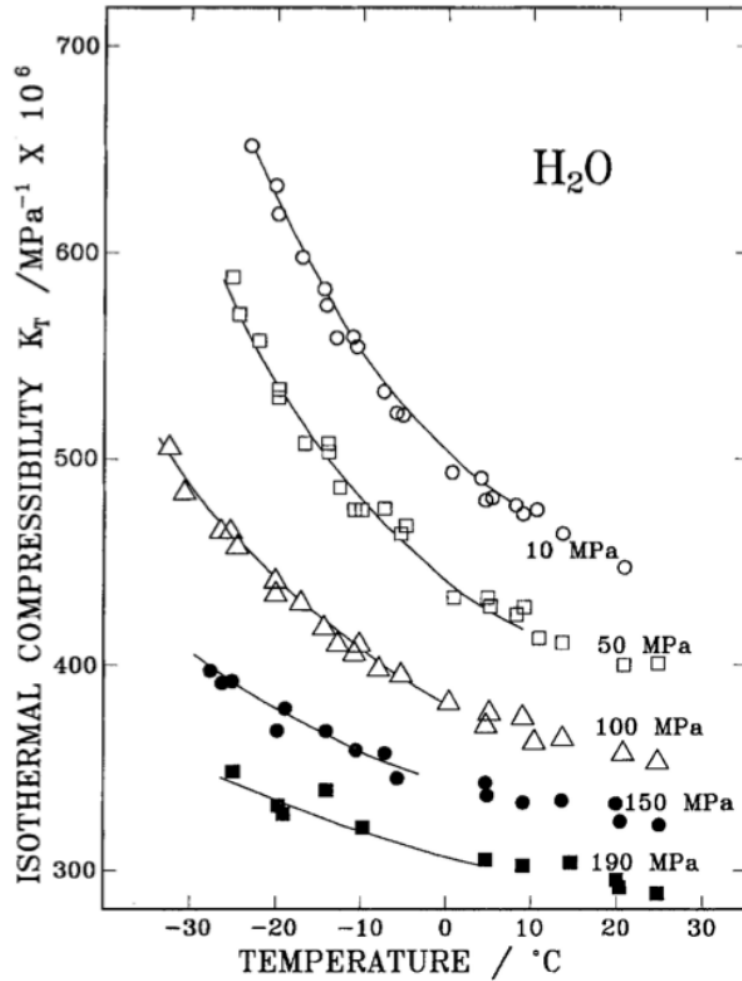


Figure 1.7: Experimental isothermal compressibility for several pressures. Curves are fit of experimental data with power law relations. Data from Ref. [42] and Figure from Ref. [3].

The minimum of κ_T in the phase diagram of water is directly connected to the presence of the **TMD** line. Using the following thermodynamic identity it is possible to connect the slope of the **TMD** to the temperature dependence

of κ_T :

$$\left(\frac{\partial \kappa_T}{\partial T}\right)_{P, \text{ at TDM}} = v^{-1} \left(\frac{\partial^2 v}{\partial T^2}\right)_{P, \text{ at TMD}} \left(\frac{dP}{dT}\right)_{TMD}^{-1} \quad (1.1)$$

where v is the molar volume, the subscript “at **TMD**” signifies that the partial derivative is evaluated at a point on the **TMD** locus, and the subscript **TMD** signifies that the derivative is evaluated along the **TMD** locus, at the state point of interest. Since the numerator at the right hand side of (1.1) is positive at **TMD** [43] and the slope of the **TMD** is negative in the $P - T$ plane the overall trend of the isothermal compressibility at **TMD** is to increase upon isobarically decreasing temperature. The behaviour of the isothermal compressibility is strongly connected also to the presence of the liquid-vapor critical point. The presence of this critical point in the high temperature range causes an asymptotic increase of the thermodynamic response functions. The occurrence of κ_T minimum is connected to both the liquid-vapor second order critical point and the presence of the **TMD**.

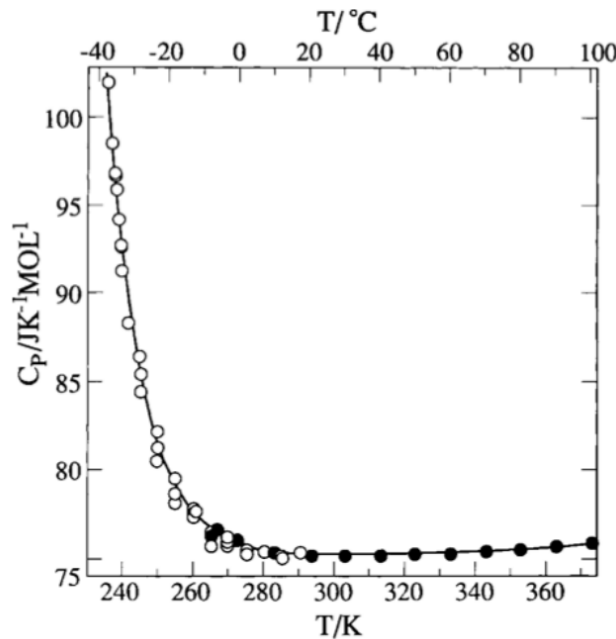


Figure 1.8: *Experimental isobaric specific heat c_P at ambient pressure. Data from Ref. [44] and Figure from Ref. [3].*

The behaviour of the isobaric specific heat also shows an high temperature regime similar to the ones of a simple liquid and deviates from it when the

temperature became lower than $T = 35^\circ\text{C}$. At ambient pressure if we cool water below that temperature c_P shows a sharp increase as reported in the Fig. 1.8 (see also the Fig. 1.4 Bottom right).

It is possible to connect the anomalies in the behaviour of the different thermodynamic response function of water in terms of the fluctuations of the liquid. Starting from the following relations:

$$\kappa_T = -\frac{1}{V} \left(\frac{\partial V}{\partial P} \right)_T, \quad (1.2)$$

$$c_P = \frac{T}{N} \left(\frac{\partial S}{\partial T} \right)_P, \quad (1.3)$$

$$\alpha_P = \frac{1}{V} \left(\frac{\partial V}{\partial T} \right)_P, \quad (1.4)$$

that are connected to the fluctuations of volume and entropy by the equations:

$$\langle (\delta V)^2 \rangle = V k_B T \kappa_T, \quad (1.5)$$

$$\langle (\delta S)^2 \rangle = N k_B C_P, \quad (1.6)$$

$$\langle \delta V \delta S \rangle = V k_B T \alpha_P, \quad (1.7)$$

These equations connect the thermodynamic response functions to the volume and entropy fluctuations of the system. The anomalous increase of these functions corresponds, therefore, to an increase in the self correlations of the liquid upon decreasing temperature, contrary to normal liquids where lower temperatures are associated to smaller fluctuations. Moreover last equation on α_P expresses the thermal expansion coefficient as a measure of the cross-correlations between volume and entropy. It follows that the transition from positive to negative values of α_P imposes a loss of entropy by increasing volume, differently to what happens in simple liquids. The anti-correlation between entropy and volume is a direct consequence of the formation of hydrogen bonds, for which a decrease in orientational entropy is accompanied by an increase in volume. The anomalies in the response function continue also below the melting temperature T_F . In fact it is possible to observe liquid water also at temperature were water should be freeze, this metastable phase is called supercooled water and will discussed in the next section.

It is possible to generalize the divergent behavior upon cooling of the response function using a power law. Considering a generic response function X , near the singular temperature T_S the behaviour of X can be represented as:

$$X = A \left(\frac{T - T_S}{T_S} \right)^{\lambda_X}, \quad (1.8)$$

λ_X is the relative exponent of the divergence. Water is an anomalous liquid not only from the thermodynamic point of view, in fact shows an anomalous behavior also in the dynamics. In particular is interesting to observe the behavior of the self diffusion coefficient D upon increasing of the pressure. We can define D through the mean square displacement (MSD) as:

$$D = \lim_{t \rightarrow \infty} \frac{\langle |r_j(t+t) - r_j(t)|^2 \rangle}{6t}. \quad (1.9)$$

The self diffusion coefficient D it is also related to the liquid viscosity through the Stokes-Einstein relations:

$$D = \mu k_B T. \quad (1.10)$$

where μ is the mobility coefficient. For a liquid made by spherical particles the value of the mobility coefficient is $\mu = 1/(6\pi\eta r)$, where η is the viscosity and r is the radius of the particles.

Since compression is usually correlated to a loss of fluidity, the coefficient D should decrease upon increasing pressure. While this happens for a simple liquid water deviates from this behaviour. In Fig. 1.9 is showed that increasing the pressure the self-diffusion decreases, but at sufficiently low temperatures a change occurs and D shows a maximum. This behaviour start at $T = 283$ K where the maximum is at a $P \simeq 150$ MPa. This anomaly is called *diffusivity anomaly* and it has been observed in several water potentials [45–48] and experiments [49, 50]. Like in the case of the thermodynamic response functions, the anomaly in the self diffusion coefficient can be explained with the presence of an HB network. When the pressure is increased a major number of HBs are broken, implying an overall greater mobility of particles within the liquid.

The series of all the anomalies that were discussed in this section clearly shows the importance of investigate the property of water, not only in its stable phases but also in the metastable ones, like supercooled water. For this reason even though the main part of this work is about the formation of ice structure it is however interesting to mention briefly the definition of supercooled liquid and the reasons that make possible the existence of such a state.

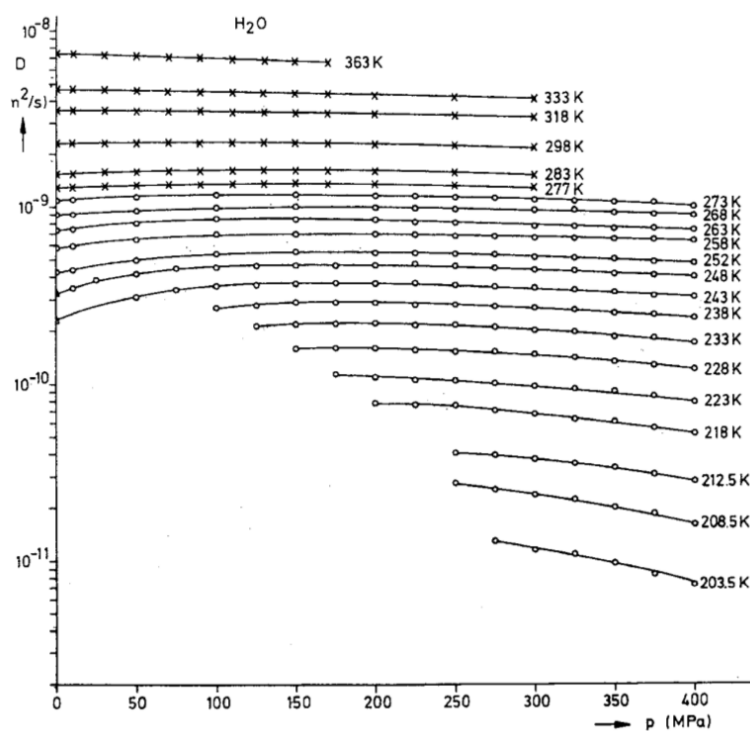


Figure 1.9: Experimental self-diffusion coefficient D of water, at constant temperature, as a function of the pressure. Figure from Ref. [4].

Core-soften potentials

A possible explanation of the water anomalies is the competition between two local structures as in the case of the core-soften potential. This model is simple enough as to permit a qualitative discussion of the origin of the anomalies, and the identification of its ultimate physical origin. Core-softened potentials were first considered by Stell and Hemmer [51] in the 1970. However, it has been recognized only after some years that these models reproduce most of the anomalous properties found in water [52, 53].

In this model, the energy between two spherical particles in the system is composed of a hard core at some distance r_0 plus a shoulder that extends up to some other distance r_1 Fig. 1.10. The details of the potential are not relevant for the discussion. For instance, some people have studied it using a square shoulder instead of a linear one, and others using a smoothed version of the linear shoulder case. However, the crucial point is that there should be an abrupt transition between low energy-high volume configurations (represented by particles at relative distance r_1) and high energy-low volume

configurations (represented by particles at relative distance r_0). Simulating a classical model of particles interacting with this potential we do observe anomalous melting [54]. The core-soften potentials are also today used for a several different studies as low dimensional liquid [55, 56], the flowing in nanotube [57] or to study hydrophobicity [58].

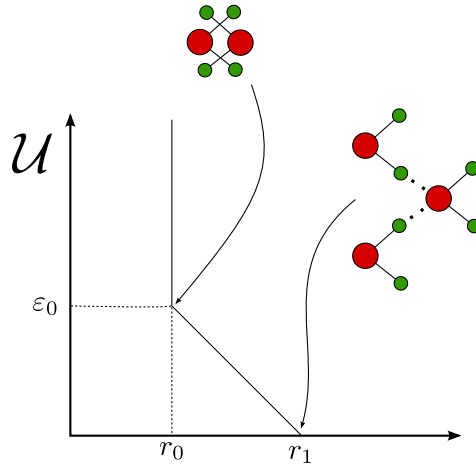


Figure 1.10: Two types of local arrangement between water molecules: high energy-low volume (left) and low energy-high-volume (right); continuous line indicate intramolecular bond and dotted lines hydrogen bond. This configuration are putted in relation with the point in a core soften potentials \mathcal{U}

1.3 Supercooled water

To observe liquid water at temperature below the melting temperature T_F special conditions are necessary. Such as the extreme purity of the sample, the absence of external mechanical and thermal perturbations, the high degree of smoothness of the walls of the container. At ambient pressure the freezing temperature is $T_F = 273$ K and under the mentioned conditions it is possible to observe liquid water until $T_h = 227$ K [59] that is the temperature of homogeneous nucleation. Liquid water below the freezing point is called supercooled water. A sketch of the range of existence at different pressure of these phases is reported in Fig. 1.11 .

In order to delay the onset of crystallization in an experiment it is necessary to decrease the concentration of impurities, because they are possible centres of nucleation of the solid phase. Dividing the sample in small droplets,

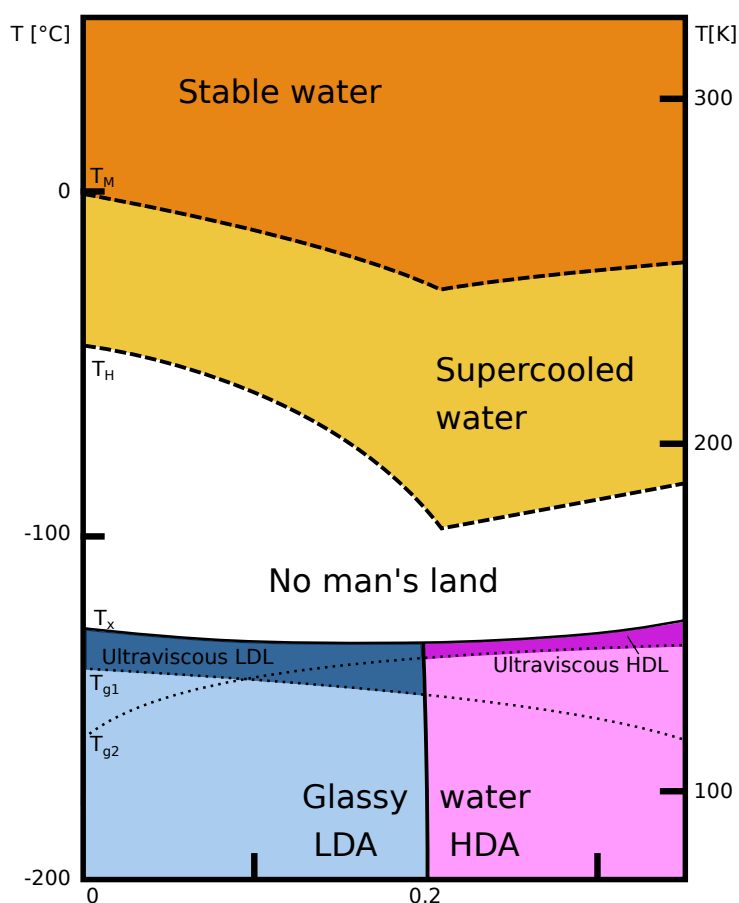


Figure 1.11: Representation of the non-crystalline forms of water. No-man's land indicates the region in which only crystalline ices have been observed so far. It is enclosed by the homogeneous crystallization line T_H from the top and the crystallization line T_X from the bottom. Two ultraviscous liquid domains, low- and high-density liquid water (LDL and HDL), can be found just below T_X . The two corresponding glass transition temperatures T_{g1} and T_{g2} separating the glassy solids LDA and HDA from the ultraviscous liquids LDL and HDL. Figure adapted from Ref. [1].

with dimensions of around $10 \mu\text{m}$, it is possible to obtain droplets that will contain, on average, less than one impurity each. The limit of this technique is reached when the intrinsic rate of crystallization becomes so fast that the lifetime of the droplets falls below the observation time [60]. Since this can be considered as a practical limit function of the cooling rate and of the observation time [4]. If the cooling rate is fast enough, the homogeneous nucleation can be bypassed and water can be brought to the glass transi-

tion. The resulting solid state without long range order, is in an amorphous state or a glass. According to the definition of Angell the glass transition temperature is located at the temperature at which the viscosity of the system becomes $\eta = 10^{13}$ poise (10^{12} Pa·s). The experimental value of T_G of water however is controversial: the general consensus is that water vitrifies around 136 K [61, 62] but latest measurements would relocate T_G at 165 K [63, 64]. The main implication of the kinetic nature of the glass transition is that different cooling procedures can produce slightly different glass transition temperatures. As it is possible to see in Fig. 1.11 above the glass transition temperature, up to the temperature of spontaneous crystallization T_X , water can exist in an extremely viscous liquid state [4]. In this small region water is defined ultraviscous. The region between T_h and T_X is often denoted as *no man's land* [35]. In this region liquid water cannot be observed with available experimental techniques because of the tremendous increase of the crystallization rate and the consequent decrease of the lifetime of the liquid state. However it is not in principle forbidden by thermodynamic constraints the existence of metastable liquid water below the homogeneous nucleation temperature [4]. In Fig. 1.11 we can observe that water also shows two amorphous phases. the most known forms of glassy water are the High Density Amorphous (HDA) and the Low Density Amorphous (LDA). Besides the HDA and the LDA a third amorphous phase was identified the Very High Density amorphous (VHDA) [65]. The presence of so many amorphous phases is known as polyamorphism of water. Has been shown that the amorphous states formed starting from the liquid or the vapour, through the hyperquenching of small droplets or the deposition of the vapour on a metal plate at very low temperatures, correspond to the LDA. While the HDA amorphous states is formed starting from the solid, through compression [3, 4, 66, 67]. Furthermore it has been shown that a first-order-like transition exists between LDA and HDA with a discontinuous jump in the density when the coexistence line is crossed [68]. This suggests that two distinct liquid phases could exist in the no man's land, the low density liquid (LDL) and the high density liquid (HDL), corresponding respectively to their amorphous counterparts LDA and HDA. This implies the existence of liquid-liquid critical point (LLCP), this scenario is a possible solution to the several anomalies that was illustrated before.

The LLCPP scenario

The origin of the LLCPP scenario are the paper of Poole et al. [69]. This was a study made by computer simulations on ST2 water by the Stanley's group at Boston University. In this paper was hypothesized the existence of two

distinct phases of water in the deep supercooled region (the no man's land). In this hypothesis the two liquid are the counterpart of the two amorphous phase the low density liquid (LDL) and the high density liquid (HDL), corresponding respectively to the experimentally observed amorphous phases LDA and HDA. We recall that crossing the separation line between the LDA and HDA a first order phase transition occurs. The analogy in this hypothesis the two phases of supercooled water would be separated by a first order phase transition line. Since was not observed the presence of two liquid phases at high temperature this line have to end in a LLCPP, above which the distinction between the two phases disappears. In analogy with what happen for the ordinary liquid-vapour critical point from the LLCPP a line of maxima of the thermodynamic response functions is emanated. This line, called Widom line, can be thought as an extension of the coexistence line in the one phase region [70,71]. The LLCPP scenario can provide an explanation of the anomalies in the response function presented before (see Section 1.2) The anomalies of the thermodynamic response functions would be due to the progressive increase of the correlation length upon approaching the critical point. The correlation length and the trends of thermodynamic response functions are supposed to diverge only at the critical point. The Widom line can be an useful tools to detect the presence or not of the LLCPP. Widom line flow close to the upper bound of the noman's land, so if water is supercooled from above toward the no man's land, the Widom line is the first detectable feature that one encounters upon cooling and that indicates the presence of the LLCPP.

In the work of Poole et al. [69], the evidence of the existence of LLCPP came out from four points:

- low-temperature isotherms showing inflection point at $\rho \approx 1$ g/cm.
- observation of two distinct phases below the estimated critical point.
- observation of the phase transition HDL-LDL.
- validation of ST2 model versus experimental results above the no-man's land .

The four points were robust and had a huge impact on the community. In successive years, much work has been done from the experimental, theoretical and computational physics communities to enrich the scenario [4, 35, 48, 69]. All the important contributions on the implication of a LLCPP in the phase diagram of supercooled water, as well as supporting and contesting works have been reviewed the last by Gallo et al. [1].

There are several experiments proof that confirm the LLCP scenario, the most important is probably the one performed by Mishima and Stanley [35, 72]. In this work they studied the melting induced by decompression of different high-pressure crystalline phases of water in oil emulsion. Mishima and Stanley also located the LLCP of water at $T = 220$ K and $P = 100$ MPa, which is today generally considered the estimated position of the liquid-liquid critical point of bulk real water (the one reported in Fig. 1.12).

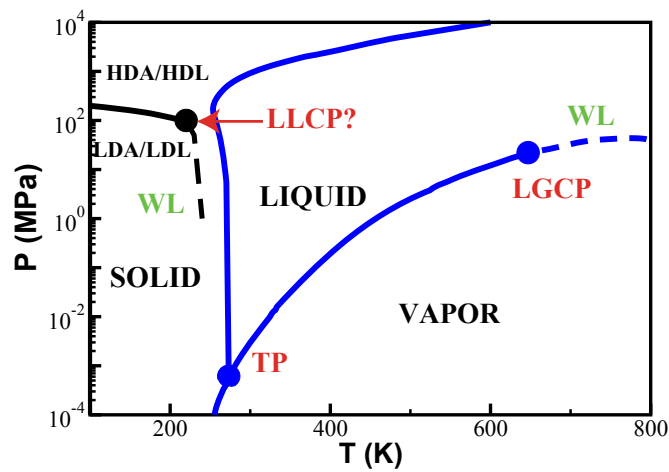


Figure 1.12: Representation of the phase diagram in the p - T plane, showing the position of the LLCP respect to the solid-liquid coexistence line (Blue line). The black line is the LDL-HDL coexistence line. The dashed line represent the Whidom line for the LLCP (Black dashed) and for the liquid-gas critical point LGGP (blue dashed). Figure adapted from Ref. [1].

In particular must be highlighted also the contribution of MD simulations. As was stated the LLCP hypothesis was based on a computational work, but computer simulations gives also other important contributes to the study of supercooled water. In fact since computational studies overcome the experimental issues of crystallization, using this technique it is possible to investigate the no-man's land. The LLCP location has been, up to date, located in the supercooled region of the phase diagram of water simulated with several different potentials. These include this include models like SPC/E, TIP4P and TIP5P and more recently TIP4P/2005 potentials (See Ref. [1] and Refs. therein). In particular was shown that SPC/E potential phase diagram is consistent with the presence of a LLCP [41] and its

location was estimated on free energy based calculations [47]. This type of computational studies can be a guide to detect experimentally viable routes aimed to the detection of the liquid-liquid transition. Several experiments are performed, following their example: supercooled water in confinement, nanodroplets, water at negative pressure and water solutions of salts.

Chapter 2

Ice Phases

Other sixteen ice phases were experimentally found other than the ice I_h . In Fig. 2.1 is reported the experimental phase space of the ice in the p - T plane.

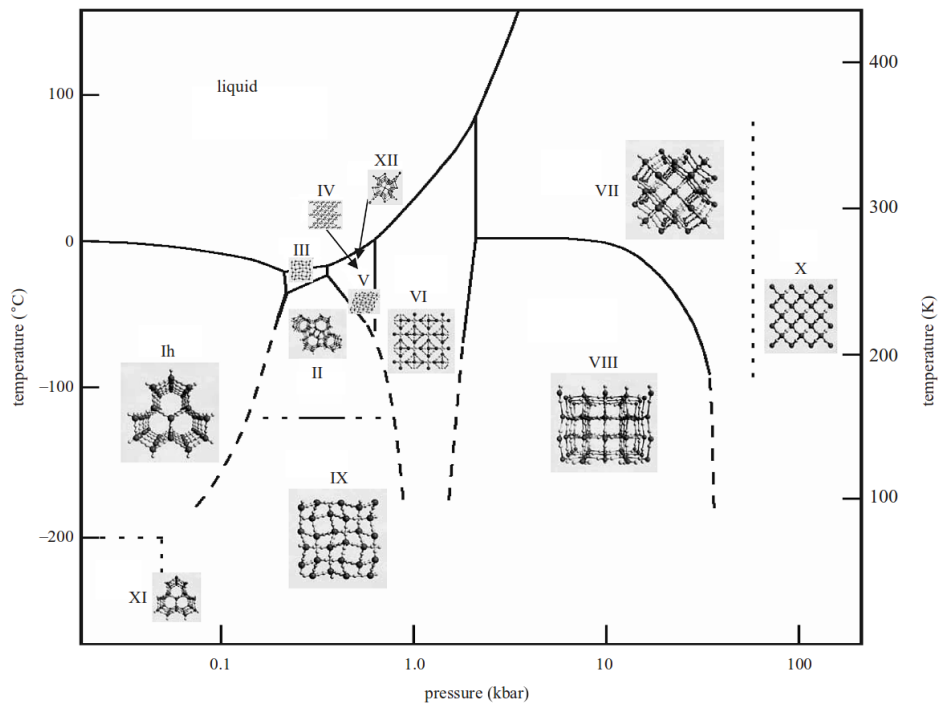


Figure 2.1: Phase diagram of the solid water in the p - T plane. Figure from Ref. [?].

We can see in Fig. 2.1 that only I_h , III, V, VI and VII have a coexistence line with liquid water in the interval of temperature reported. The ice X can have a coexistence line at very high temperature even that was not proved

by experiment. In Fig. 2.1 we can see the several triple point of the ice phases. We recall that a triple point is the only point in the p - T where three phase can coexist.

Even that Ice can assume several crystalline forms; hexagonal, cubic, tetragonal, rhombohedral or monoclinic (see Fig. 2.2 for more details). there are some common features that all the ice forms share (with the exception of ice X):

- The position of the oxygen forms an ordered network, as usual for a solid. The position of the hydrogen instead is a more delicate issue. There some forms of ice (II, VII, IX, XI, XIII, XIV and XV) in which the hydrogens have a well defined crystallographic structure. Nevertheless in the other forms of ice the hydrogens do not show any regular pattern. This issue is called “proton ordering” and we will discuss more in details in the next section.
- Each oxygen is surrounded by other four oxygens in the first shell of coordination, forming a tetrahedral structure that can be more or less distorted depending on the ice forms.
- Ice are formed by water molecules. Between two oxygen there is always an hydrogen. This hydrogen has a covalent bond with the oxygen with which forms the water molecule and an HB with the other.

The rules previously described summarize the structures of the ice forms and are commonly known as rules of Bernal and Fowler [?] or generally ice rules. According of this rules each oxygen in ice is surrounded by four hydrogens, with two of them forms a water molecules and with the other two forms an hydrogen bond.

The only phase of ice that dose not follow this rules is the Ice X, that has a completely symmetric structure. we will discus of this ice phase in the last section of this chapter.

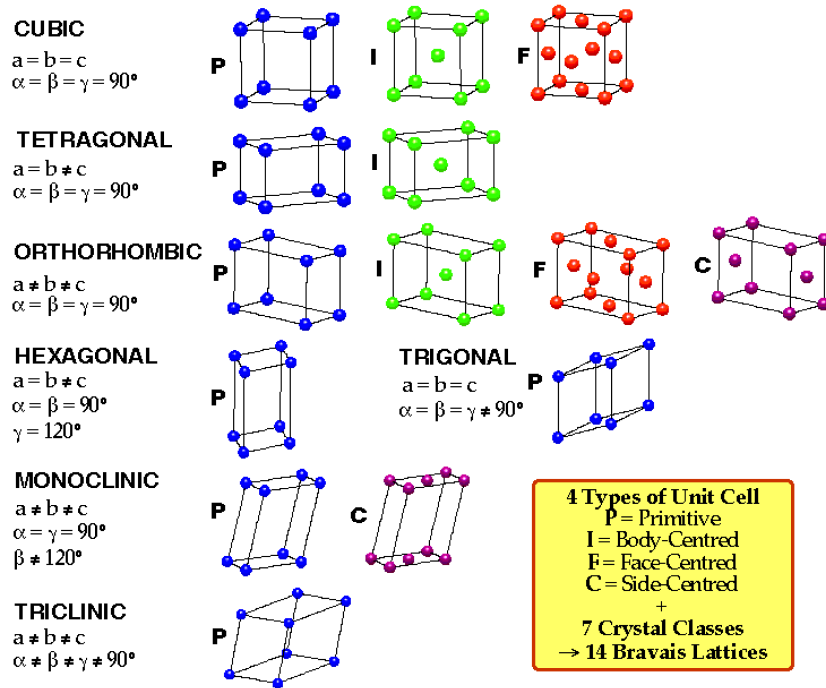


Figure 2.2: Representation of the 7 crystal system and the 14 Bravais lattice. Each crystal system is characterized by a different value of the edge length and angle of the unitary cell.

2.1 Ice I_h and Ice XI, the Issue of Proton Ordering

The ice I_h is the most known phase of ice since is the one formed at the freezing temperature ($T_F = 273$ K) at ambient pressure ($p = 1$ kPa). This ice phase was the first classified by Tamman *et al.* [?] for this reason was assigned to him the symbol I. To distinguish two phase of ice I, the stable and the metastable, was later added a letter. For the one with the hexagon structure the letter was h and c for the one with a cubic structure that are respectively the stable and the metastable ice phase. The structure of the ice I_h was established in the 1935 by Pauling [73]. The oxygen atoms form an hexagonal ordered structure. The hydrogen atoms occupy the space between two oxygens but do not show any ordered structure. The ice I_h can be in equilibrium with both the liquid and the vapor phase of water and in particular shows a triple point in the p - T plane for a temperature of 273.16

K and a pressure of 611.7 Pa. For pressure lower than 611.7 Pa the water sublimates upon the increase of the temperature.

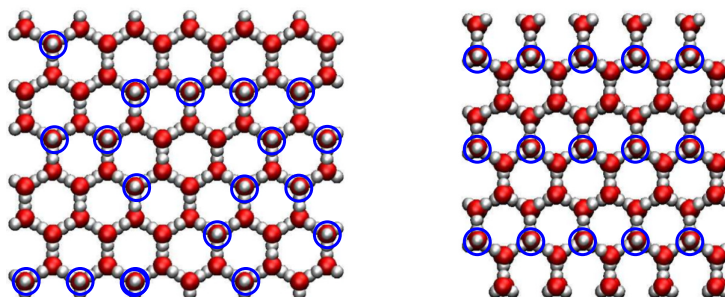


Figure 2.3: (Right) Schematic picture of the hexagonal structures of ice I_h frontal view of the basal plane. (Left) Schematic picture of the orthorhombic structures of ice XI proton ordered partner of the ice I_h . In both cases the oxygen are represented as red spheres and the hydrogen as white spheres. The blue circle highlight the hydrogen that point in the same direction.

As we stated before the ice I_h have an hexagonal structures well described by the space group $P6_3/mmc$ with four atoms for unitary cell. In the right panel of Fig. 2.3 it is showed the disordered structures of the hydrogens and it is possible to observe the presence of hexagonal channel. The presence of this channels lead to the low density of this structures. The density for the I_h is in fact lower than the density of liquid water.

In left panel of Fig. 2.3 is reported the structure of the ice XI, this ice phase is the ordered partner of ice I_h . This phase of ice was observed in the 1972 by Kawada [?]. This ice have an orthorhombic structures and belong to the spacial group $Cmc2_1$, its unitary cell contain 8 water molecules. present a triple point with the ice I_h and the vapor at $T = 72$ K and $p \approx 0$ Pa. This ice can be obtained starting from dilute KOH solution kept just below 72 K at ambient pressure for about a week [?]. Ice XI can also be produced from a thin film (20 nm) of pure solute-free cubic ice (I_c) under electron beam irradiation [?].

In Fig. 2.3 it is possible to observe the difference in the order of the hydrogens between the two forms of ice. If the structures of the oxygens is the same for the two forms of Ice, it is evident that there is a difference in the position of the hydrogens. We have highlighted in Fig. 2.3 the hydrogens in a positions that point out of the plane with a blue circle. In the right panel there is ice I_h that present a random distribution of hydrogens that point out, instead in the ice XI there is an succession of row wit an hydrogen that point out and one one that point in.

2.2 Pauling Entropy

An argument that is strictly connected to the proton ordering is the zero point entropy or Pauling entropy. Following the ice rules presented in the previous section in ice a water molecule is surrounded by 4 hydrogen atoms two hydrogens of the same molecule while the other two belong to the adjacent water molecule this lead to have different configuration with the same energy as showed in Fig. 2.4 .

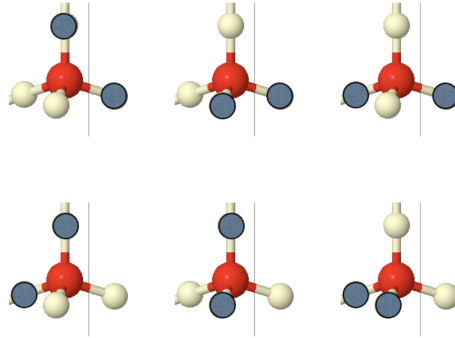


Figure 2.4: *Cartoon of all possible configuration of a water molecule.*

In 1935 Pauling used the ice rules to calculate the residual entropy (zero temperature entropy) of ice from the of Boltzmann's relation.

$$S_0 = k_B \ln W, \quad (2.1)$$

were W is total number of configurations of the hydrogen (H) positions. Considerer a crystal of N molecules large enough to ignore the surface, there will be $2N$ bonds between these molecules with one H. Each molecule have 6 possible orientations that satisfy the ice rules (see Fig. 2.4). For each one of the two H positions it is necessary that the adjacent molecule have to be in a configuration (of the 6 available) that have lone pair in correspondence. There is so a probability equal to $1/2$ that a given direction is available for each H of the original molecule $1/2$ and the chance that both can be located in accordance with the given orientation is $1/4$.

$$W = \left(\frac{6}{4}\right)^N = \left(\frac{3}{2}\right)^N \quad (2.2)$$

giving that in the simple Pauling approximation the zero-point entropy of one mole of ice is:

$$S_0 = N_A k_B \ln \left(\frac{3}{2}\right) = 3.371 \text{ J K}^{-1} \text{ mol}^{-1}. \quad (2.3)$$

2.3 Other Ice Forms

There are other fifteen phases of ice beside the two described before. We do not enter in the detail of each structure we just report the main features of each type of ice in Tab. 2.1. However something can be said on the most peculiar of the various ice forms the ice X.

As we said above the ice X is the only ordered structure of solid water that does not follow the ice rules. Ice-X cubic structure consisting of 8 unit cells of two water molecules plus extra atoms found within the basic cubic structure. This type of ice can be obtained starting from the ice VII and increasing the pressure, when the O-O distance contracts, ice VII appears to undergo a continuous transition into cubic ice-X. In this structure the hydrogens are equispaced (and equally bonded) between the oxygen atoms in a molecular crystal [?]. Thus each oxygen atom has four equidistantly tetrahedrally placed nearest neighbor hydrogen atoms. The oxygen atoms are arranged in a body-centered cubic arrangement. The hydrogen atoms instead have 12 nearest neighbor hydrogen atoms arranged in a body-centered truncated cube. this structure is obtained at extreme value of pressure and is the ice phase with the highest density, as it is possible to see in Tab. 2.1. Ice X is a solid structure composed by oxygens and hydrogens but not from water molecules since all the hydrogens are placed between the two oxygens. This also imply that the ice X can not be obtained in MD simulations that use a rigid model for water.

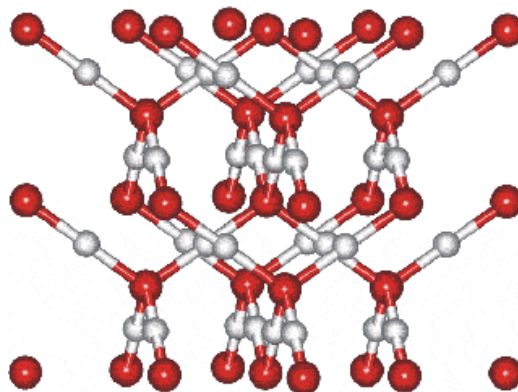


Figure 2.5: *Cartoon of the ice X structure. The reds and the white spheres are respectively the oxygen and the hydrogens.*

Table 2.1: List of all the ice that was found experimentally. The density was the experimental value. The Protons column is reported the ordering of the hydrogens. The Crystal and Symmetry columns report the information about the structure.

Ice	Density [g/cm ³]	Protons	Crystal	Symmetry
Ih	0.92	D	Hexagonal	$P6_3/mmc$ one C_6
Ic	0.93	D	Cubic	$Fd\bar{3}m$ four C_3
II	1.17	O	Rhombohedral	$R\bar{3}$ one C_3
III	1.14	D	Tetragonal	$P4_12_12$ one C_4
IV	1.27	D	Rhombohedral	$R\bar{3}$ one C_3
V	1.23	D	Monoclinic	$C2/c$ one C_2
VI	1.31	D	Tetragonal	$P4_2/nmc$ one C_4
VII	1.50	D	Cubic	$Pn\bar{3}$ four C_3
VIII	1.46	O	Tetragonal	$I4_1/amd$ one C_4
IX	1.16	O	Tetragonal	$P4_12_12$ one C_4
X	2.51	S	Cubic	$Pn\bar{3}$ four C_3
XI	0.92	O	Orthorhombic	$Cmc2_1$ three C_2
XII	1.29	D	Tetragonal	$I\bar{4}2d$ one C_4
XIII	1.23	O	Monoclinic	$P2_1/a$ one C_2
XIV	1.29	O	Orthorhombic	$P2_12_12_1$ one C_4
XV	1.30	O	Pseudo-orthorhombic	$P\bar{1}$ one C_4
XVI	0.81	D	Cubic	$Fd\bar{3}m$

D disordered structure of the hydrogens.

O ordered structure of the hydrogens.

S symmetric structure.

Chapter 3

Molecular Dynamics Simulations

3.1 Classical Molecular Dynamic Simulations

Molecular Dynamics (MD) is one of the most diffuse computational techniques used in physics. This technique was developed in the late 1950s within the field of theoretical physics [74, 75] but is applied today in large number of other fields like: chemical physics, materials science and biophysics. In MD is used an numerical integration of the Newton's law of motion to evolve the system. In this way a series of trajectories are obtained, providing a description how the positions and velocities of the particles in the system vary with time.

Since it is complicated to treat with analytic techniques the liquid state MD techniques are often used in this field. The use of continuous potentials to describe the intermolecular interactions produce very realistic results, since the forces that act on a particle are recalculated at each changing of configuration [76]. The use of continuous potential had a constant improvement since was employed the first time by Rahman in the 1964 [75]. In that work Rahman use the Lennard Jones potential to perform an MD study on liquid argon. Few years lather Rahman, together with Stillinger, perform the first MD simulation of liquid water [5]. Several step forward was made in MD from that first work. The evolution of this technique is due not only to an improvement of the machine hardware, but mostly to the improvement of the interaction potentials and the computational methods.

The starting point of a MD simulation is the Hamiltonian \mathcal{H} . For a simulated system which contains a fixed number of particles N the Hamiltonian is in general given by:

$$\mathcal{H}(\{\mathbf{r}_i\}_N, \{\mathbf{p}_i\}_N) = \mathcal{K}(\{\mathbf{p}_i\}_N) + \mathcal{U}(\{\mathbf{r}_i\}_N), \quad (3.1)$$

where \mathcal{K} is kinetic energy and \mathcal{U} is the many-body interaction potential. The

potential \mathcal{U} can be assumed to be approximated with the sum of the radial potentials u_{ij} between pairs of particles.

$$\mathcal{U}(\{\mathbf{r}_i\}_N) = \frac{1}{2} \sum_i \sum_{j \neq i} u_{ij}(|\mathbf{r}_i - \mathbf{r}_j|).$$

As previously stated, the trajectory of the particles are obtained by solving the differential equations embodied in Newton's second law:

$$m_i \ddot{\mathbf{r}}_i = \dot{\mathbf{p}}_i = \mathbf{F}_i = -\nabla_{\mathbf{r}_i} \mathcal{U}, \quad (3.2)$$

$$v_i = \dot{\mathbf{r}}_i = \frac{\mathbf{p}_i}{m_i}. \quad (3.3)$$

The use of a finite difference method to integrate this equation a discretization δt of the temporal axis. Given the positions and the velocities of the particles at time t , the positions and the velocities of the particles at time $t + \delta t$ can be computed. Thus positions and velocities of particles are calculated in a deterministic way. Details about integration algorithms are given in Section 3.2

To perform an MD simulation it is necessary to provide an initial configuration of the particles. Suitable initial space configurations are usually assembled by placing the particle at the vertices of standard lattices. In more complex solute-solvent systems it is necessary to provide a more realistic conformations of molecules, this configuration are taken from crystallographic data. Stated the relation between temperature and kinetic energy, the velocity configurations was created according to random values from the Maxwell-Boltzmann distribution centered at the temperature of interest:

$$P(v_{ix}) = \sqrt{\frac{m_i}{2\pi k_B T}} \exp\left[-\frac{m_i v_{ix}^2}{2k_B T}\right], \quad (3.4)$$

which provides the probability that at the temperature T , the particle i of mass m_i has a velocity v_{ix} along the x axis.

After the initial conditions are given, the first stage of the MD simulation is the equilibration of the system. Starting from the initial configuration, the system is then allowed to run for periods of time long enough to fully relax. Once the energy is minimized, all counters are set to zero and the system is allowed to evolve. This last stage is commonly named production run.

The trajectories produced by MD simulations correspond to a sequence of points in the phase space as a function of time. In order to face off experimental data it is necessary to evaluate from this microscopic quantities macroscopic properties as energy or other thermodynamic functions of the

system. To convert from microscopic to macroscopic properties we can use the statistical mechanics.

In statistical mechanics, average values are defined as ensemble averages. The ensemble average of the observable of interest $A = A(\mathbf{r}, \mathbf{p})$ is given by:

$$\langle A \rangle = \int \int d\mathbf{r}^N d\mathbf{p}^N A(\{\mathbf{d}\mathbf{r}_i\}_N, \{\mathbf{d}\mathbf{p}_i\}_N) \rho(\{\mathbf{d}\mathbf{r}_i\}_N, \{\mathbf{d}\mathbf{p}_i\}_N), \quad (3.5)$$

where integrations are over all possible variables of \mathbf{r} and \mathbf{p} of the phase space and $\rho(\mathbf{r}, \mathbf{p})$ is the probability density of the ensemble. This can be written through the the partition function \mathcal{Z} of the ensemble as:

$$\rho(\mathbf{r}, \mathbf{p}) = \frac{1}{\mathcal{Z}} \exp(-\beta \mathcal{H}(\mathbf{r}, \mathbf{p})) \quad (3.6)$$

where \mathcal{H} is the Hamiltonian, k_B the Boltzmann constant and T the temperature. The the ergodic hypothesis have crucial implication in the MD. Then the ensemble average is equal to time average:

$$\langle A \rangle = \langle A \rangle_{time} \quad (3.7)$$

and the ensemble average of the quantity A can be therefore written as:

$$\langle A \rangle = \langle A \rangle_{time} = \lim_{t \rightarrow \infty} \frac{1}{t} \int_0^t A(\mathbf{r}^N, \mathbf{p}^N) d\tau \simeq \frac{1}{M} \sum_{t=1}^M A(\mathbf{r}^N, \mathbf{p}^N) \quad (3.8)$$

where t is the length of the simulation, M is the number of time steps in the simulation and $A(\mathbf{r}, \mathbf{p})$ is the instantaneous value of A . The validity of the ergodic hypothesis in MD simulations is strictly related to the generation of enough representative conformations of the phase space. If this is the case, the equality (3.7) is satisfied and the significant observables regarding structure, dynamics and thermodynamics can be calculated via Eq. (3.8).

The sampling of enough phase space during a MD simulation requires that the simulation time exceeds by far the characteristic time of molecular motion. For this reason the MD simulation of a given state point is divided in two part previously discussed, i.e. the equilibration runs during which trajectories are evolved until the equilibrium is reached (typically with algorithms that rescale velocities), and production runs during which equilibrated trajectories are stored.

The Microcanonical Ensemble (NVE), when the thermodynamic state is characterized by a fixed number of particles N , a fixed volume V , and a fixed total energy E . Since the total energy of the system $E = \mathcal{K} + \mathcal{U}$ is conserved, this is the natural ensemble of MD. The temperature of the system can be calculated with the equipartition theorem by:

$$T = \frac{2\langle\mathcal{K}\rangle}{(3N - N_C)k_B}, \quad (3.9)$$

where N_C is the number of constraints (for example $N_C = 3$ if the the system center of mass motion is removed). The pressure can be calculated using the virial theorem:

$$P = \frac{Nk_B - \frac{1}{3}\langle\mathcal{V}\rangle}{V}, \quad (3.10)$$

where $\mathcal{V} = \sum_{i=1}^N \mathbf{r}_i \cdot \mathbf{F}_i$ is the virial. MD simulations can run in different ensemble such the (NPT) and (NVT) introducing thermostats and barostats, this tools will be discussed in Section 3.3.

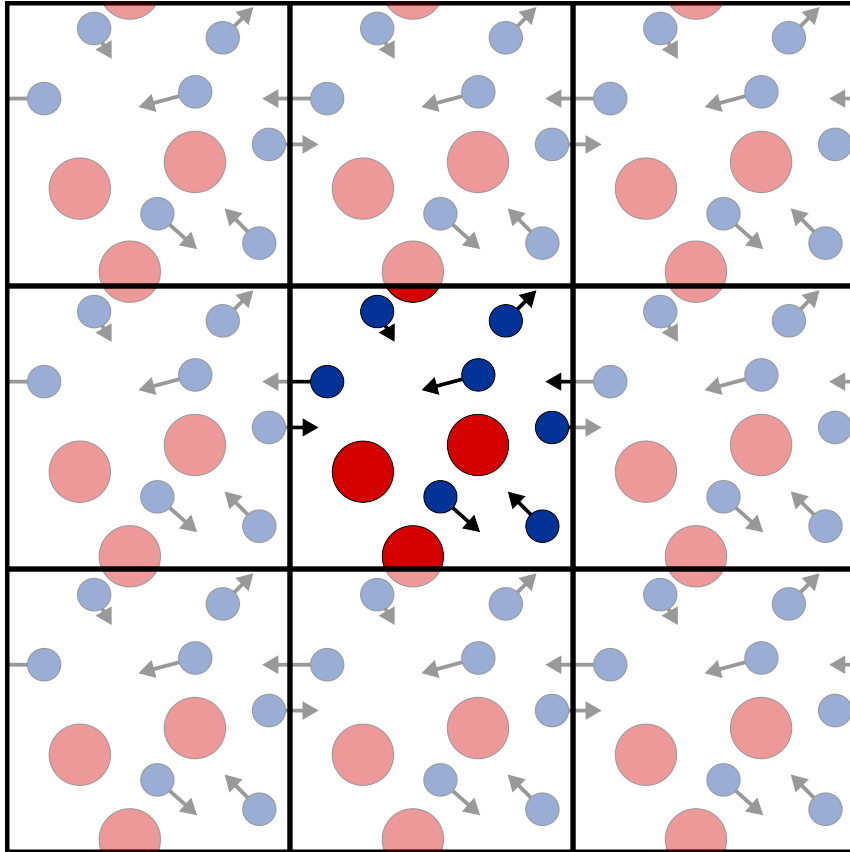


Figure 3.1: *Illustration of PBC in MD simulations.*

Relevant to MD simulations is the suitable treatment of boundaries. Periodic boundary conditions (PBC) are usually applied to calculate bulk gases, liquids and crystals. This has indeed a twofold importance, because it

avoids artifacts due to the boundaries of the finite simulation box (that can act as an external field) and, from the computational point of view, it enables to perform MD simulations with a relatively small number of molecules. Figure 2.1 shows the common form of PBC applied for particle balance in a 2D system. The central simulation box is replicated in all directions to construct image boxes, which give rise to a periodic lattice. Consequently, to each particle leaving the central box always corresponds one of its image entering the box from the opposite side. This preserves the number of particles in box.

3.2 Integrate the equations of motion

As was explained in the previous section the core of the Molecular Dynamic is the numerical integration of equations of motions in order to calculate the trajectories of the particles. The integration time step must be much less than the time taken by the molecule to cover a distance equal to its own length. Typically $\delta t = 10^{-15}$ s = 1 fs for phenomena that take place at the picoseconds or nanoseconds scale. In the case of rigid molecules, like water, the motion can be separated into translational and rotational motion. The most common algorithm used to integrate the translational motion is the so called “leap-frog” algorithm. This algorithm is a derivation of Verlet’s algorithm [77]. In order to better understand how the “leap-frog” work, is useful to start describing this latter algorithm. The Verlet’s algorithm consider the Taylor expansion for the position, the velocity and the acceleration of a molecule:

$$\mathbf{r}_i(t + \delta t) = \mathbf{r}_i(t) + \mathbf{v}_i(t)\delta t + \frac{1}{2}\mathbf{a}_i(t)\delta t^2 + o(\delta t^3) \quad (3.11)$$

$$\mathbf{v}_i(t + \delta t) = \mathbf{v}_i(t) + \mathbf{a}_i(t)\delta t + \frac{1}{2}\mathbf{b}_i(t)\delta t^2 + o(\delta t^3) \quad (3.12)$$

$$\mathbf{a}_i(t + \delta t) = \mathbf{a}_i(t) + \mathbf{b}_i(t)\delta t + o(\delta t^2) \quad (3.13)$$

To simplify the previous equations we can consider:

$$\mathbf{r}_i(t - \delta t) = \mathbf{r}_i(t) - \mathbf{v}_i(t)\delta t + \mathbf{a}_i(t)\delta t^2 + o(\delta t^3), \quad (3.14)$$

now summing the Eq.3.11 with the Eq.3.14 we obtain:

$$\mathbf{r}_i(t + \delta t) = 2\mathbf{r}_i(t) - \mathbf{r}_i(t - \delta t) + \mathbf{a}_i(t)\delta t^2 + o(\delta t^4). \quad (3.15)$$

In this way the velocity term from the equation for the position can be eliminated, making the algorithm faster. In the Verlet procedure the velocity

can be recovered calculating

$$\mathbf{v}_i = \frac{\mathbf{r}_i(t + \delta t) - \mathbf{r}_i(t - \delta t)}{2\delta t} \quad (3.16)$$

Verlet's algorithm is fast and robust but it does not allow an accurate computation of the velocities. This can be amended with the leap-frog algorithm.

Given the quantities $\mathbf{r}_i(t)$, $\mathbf{a}_i(t)$ and $\mathbf{v}_i(t - \frac{1}{2}\delta t)$ a two step iteration is made, in which first the velocities are updated through

$$\mathbf{v}_i\left(t + \frac{1}{2}\delta t\right) = \mathbf{v}_i\left(t - \frac{1}{2}\delta t\right) + \mathbf{a}_i(t)\delta t \quad (3.17)$$

then the positions of the particles are calculated with:

$$\mathbf{r}_i(t + \delta t) = \mathbf{r}_i(t) + \mathbf{v}_i\left(t + \frac{1}{2}\right)\delta t \quad (3.18)$$

The forces are calculated after the second step and the new accelerations can be put into Eq. (3.17) to begin a new iteration. A diagram of the leap-frog iteration algorithm is depicted in Fig. 3.2 .

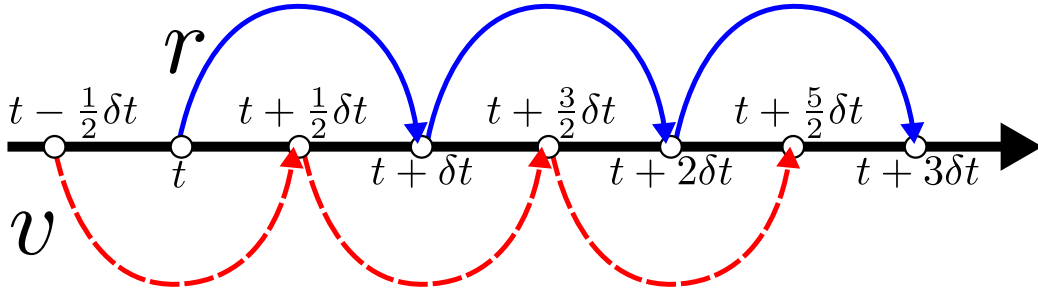


Figure 3.2: Schematic representation of the leap-frog algorithm. Dashed red lines represent the first step, Eq. (3.17), with the calculation of the velocities while solid blue lines represent the second step, Eq.(3.18), with the calculation of the positions.

Respect to the Verlet algorithm the leap-frog yields a more accurate positions. They are in fact calculated using a velocity at a time closer to $t + \delta t$. The forces are computed taking the derivative of the potential generated by the distribution of particles ensuing from Eq. (3.18). Velocities at time t can be simply obtained from the relation

$$\mathbf{v}_i = \frac{\mathbf{v}_i\left(t + \frac{1}{2}\delta t\right) - \mathbf{v}_i\left(t - \frac{1}{2}\delta t\right)}{2\delta t}, \quad (3.19)$$

While the integration of the translational motion is quite straightforward. The rotational motion of molecules requires a more complex treatment. The vector τ_i , the torque with respect to the center of mass of the molecule positioned at \mathbf{r}_i , is defined by

$$\tau_i = \sum_a (\mathbf{r}_{ia} - \mathbf{r}_i) \times \mathbf{F}_{ia} \equiv \sum_a \mathbf{d}_i \times \mathbf{F}_{ia} \quad (3.20)$$

where \mathbf{d}_{ia} denotes the position of the atom a within the molecule i with respect to its center of mass. The orientation of a rigid body in the space can be defined by a rotation matrix that consents the transformation from the frame of reference of the laboratory to the one of the center of mass. This matrix is usually defined in terms of three independent angular parameters, the *Euler angles* (ϕ, θ, ψ) . A quadri-dimensional vector, with unitary norm, can be defined as a function of the Euler angles. This vector is called quaternion and it permits to have convergent equations of motion. Defined \mathbf{q} as

$$\mathbf{q} = (q_0, q_1, q_2, q_3) \quad (3.21)$$

with $q_0^2 + q_1^2 + q_2^2 + q_3^2 = 1$, the rotation matrix can be written in terms of \mathbf{q} . It reads

$$\mathcal{R} = \begin{pmatrix} q_0^2 + q_1^2 - q_2^2 - q_3^2 & 2(q_1q_2 + q_0q_3) & 2(q_1q_3 - q_0q_2) \\ 2(q_1q_2 - q_0q_3) & q_0^2 - q_1^2 + q_2^2 - q_3^2 & 2(q_2q_3 + q_0q_1) \\ 2(q_1q_3 + q_0q_2) & 2(q_2q_3 + q_0q_1) & q_0^2 - q_1^2 - q_2^2 + q_3^2 \end{pmatrix} \quad (3.22)$$

and if $\hat{\mathbf{d}}_{ia}$ is the position of the atom i in the center of mass frame, its position in the laboratory frame is obtained by $\mathbf{d}_{ia} = \mathcal{R}^T \hat{\mathbf{d}}_{ia}$. The quaternion for each molecule satisfies the equations of motion:

$$\begin{pmatrix} \dot{q}_0 \\ \dot{q}_1 \\ \dot{q}_2 \\ \dot{q}_3 \end{pmatrix} = \begin{pmatrix} q_0 & -q_1 & -q_2 & -q_3 \\ q_1 & q_0 & -q_3 & q_2 \\ q_2 & q_3 & q_0 & -q_1 \\ q_3 & -q_2 & q_1 & q_0 \end{pmatrix} \cdot \begin{pmatrix} 0 \\ \omega_x \\ \omega_y \\ \omega_z \end{pmatrix} \quad (3.23)$$

where $(0, \omega_x, \omega_y, \omega_z)$ are the components of the angular velocity vector $\boldsymbol{\omega}$ in the center of mass frame. This system does not possess singularities and it can be solved with a procedure similar to the one applied for the integration of the translational motion. To solve the rotational motion the following equation can be used:

$$\frac{d\mathbf{J}}{dt} = \frac{d}{dt}(I\boldsymbol{\omega}) = \boldsymbol{\tau} \quad (3.24)$$

where \mathbf{J} is the total angular momentum of the molecule, I the moment of inertia matrix and $\boldsymbol{\tau}$ the torque of the molecule (for convenience here the

subscript i indicating each molecule is dropped). This equation is evidently coupled to Eq. (3.23) Having stored $J(t - \delta t)$, $\mathbf{q}(t)$ and $\boldsymbol{\tau}(t)$ the equations for the rotational motion can be solved iteratively, first updating the angular momentum through:

$$\mathbf{J} = \mathbf{J} \left(t - \frac{1}{2} \delta t \right) + \boldsymbol{\tau}(t) \frac{1}{2} \delta t \quad (3.25)$$

Then the $\dot{\mathbf{q}}$ can be calculated from Eq. (3.23) and a guess for $\mathbf{q} \left(t + \frac{1}{2} \delta t \right)$ is given by:

$$\mathbf{q} \left(t + \frac{1}{2} \delta t \right) = \mathbf{q}(t) + \dot{\mathbf{q}}(t) \frac{1}{2} \delta t \quad (3.26)$$

The last two are auxiliary equations to estimate $\mathbf{q} \left(t + \frac{1}{2} \delta t \right)$ and calculate \mathbf{q} at the half-step time. Now the new \mathbf{J} and \mathbf{q} can be calculated through the relations:

$$\mathbf{J} \left(t + \frac{1}{2} \delta t \right) = \mathbf{J} \left(t - \frac{1}{2} \delta t \right) + \boldsymbol{\tau}(t) \delta t \quad (3.27)$$

$$\mathbf{q}(t + \delta t) = \mathbf{q}(t) + \dot{\mathbf{q}} \left(t + \frac{1}{2} \delta t \right) \delta t \quad (3.28)$$

Another way to reproduce the motion of a rigid body are the constraint algorithms, now day are probably the most used method. This method involve the introduction of a constraint in the distance between the sites of the molecule. The general steps involved are the follows:

1. Let the particle move separately.
2. Introduce explicit constraint forces.
3. Minimize this forces using the technique of Lagrange multipliers or another method.

Lagrangian Multipliers

The method of the Lagrangian multipliers is the most used in MD simulations to minimize the force of the constraints. We introduce a set of n linear (holonomic) constraints at the time t ,

$$\sigma_k(t) := \|\mathbf{x}_{k\alpha}(t) - \mathbf{x}_{k\beta}(t)\|^2 - d_k^2 = 0, \quad k = 1 \dots n \quad (3.29)$$

where $\mathbf{x}_{k\alpha}(t)$ and $\mathbf{x}_{k\beta}(t)$ are the positions of the two particles involved in the constraint k and d_k is the intramolecular distance fixed by the constraint. The

equations of motion have to take in account the force due to this constraints. Is important to note that adding the constraint forces does not change the total energy, as the total work done by the constraint forces is zero as act is the same for the two particles with opposite direction. For each one of the N particles in the system the force is given from:

$$\frac{\partial^2 \mathbf{x}_i(t)}{\partial t^2} m_i = -\frac{\partial}{\partial \mathbf{x}_i} \left[V(\mathbf{x}_i(t)) + \sum_{k=1}^n \lambda_k \sigma_k(t) \right], \quad i = 1 \dots N. \quad (3.30)$$

From integrating both sides of the equation with respect to the time, the constrained coordinates of particles at the time, $t + \delta t$, are given,

$$\mathbf{x}_i(t + \delta t) = \mathbf{x}_i^f(t + \delta t) + \sum_{k=1}^n \lambda_k \frac{\partial \sigma_k(t)}{\partial \mathbf{x}_i} (\delta t)^2 m_i^{-1}, \quad i = 1 \dots N \quad (3.31)$$

where $\mathbf{x}_i^f(t + \delta t)$ is the free position of the particle i after integrating the unconstrained equations of motion.

To satisfy the constraints $\sigma_k(t + \delta t)$ in the next timestep, the Lagrange multipliers should be determined as the following equation,

$$\sigma_k(t + \delta t) := \|\mathbf{x}_{k\alpha}(t + \delta t) - \mathbf{x}_{k\beta}(t + \delta t)\|^2 - d_k^2 = 0. \quad (3.32)$$

This implies solving a system of n non-linear equations simultaneously for the n unknown Lagrange multipliers λ_k . This system of n non-linear equations in n unknowns is commonly solved using Newton-Raphson method.

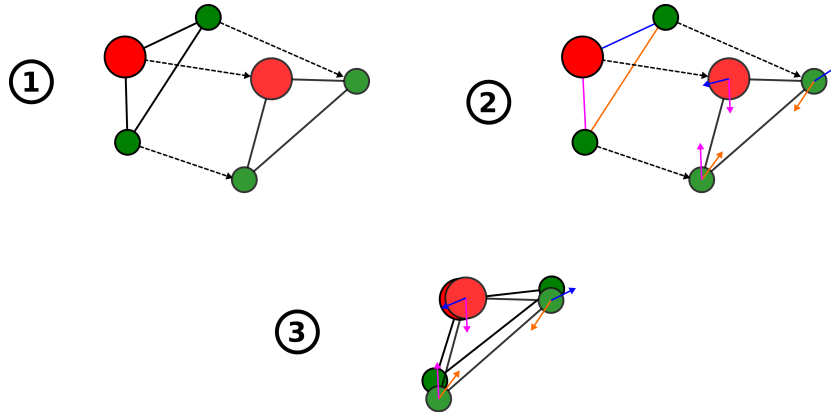


Figure 3.3: Schematic representation of the steps involved in the constraint method.

3.3 Thermostats and Barostats

As stated in section 3.1, the NVE is the natural ensemble of basic MD. Often it is necessary to keep temperature and/or pressure fixed in a simulation, for example to mimic real thermodynamic condition of an experiment. Even in the constant NVE simulation, it is however common to regulate the temperature during the equilibration phase. Fortunately nowadays are actually available several of thermostats and barostats to accomplished this need.

We know that the temperature of the system is connected to the average of the kinetic energy \mathcal{K} by the equation (3.9). This give us a simple way to control the temperature of the system rescaling the velocities in order to obtain the desired temperature. In fact if the velocities are multiplied by a factor λ at time t , the variation of the temperature in the unconstrained system is given by:

$$\Delta T = \frac{1}{2} \sum_{i=1}^N \frac{2 m_i (\lambda v_i)^2}{3 N k_B} - \frac{1}{2} \sum_{i=1}^N \frac{2 m_i \lambda v_i^2}{3 N k_B} = (\lambda^2 - 1) T(t) \quad (3.33)$$

Thus in order to drive the current temperature of the system $T(t)$ to the desired value T_D , velocities must be multiplied at each time step by a factor λ given by:

$$\lambda = \sqrt{\frac{T_D}{T(t)}} \quad (3.34)$$

One of the most used thermostats is the one proposed by Berendsen et al. [78] in 1984. In that paper was proposed an alternative way to control the temperature, coupling the system whit an external heat bath at fixed temperature. In this way the external bath supply or remove heat from the system, bringing it to the desired temperature. This method gives an exponential decay of the temperature of the system towards the desired temperature value. The change in temperature between two successive time step is given by:

$$\frac{dT(t)}{dt} = \frac{1}{\tau} (T_B - T(t)) \rightarrow \delta T = \frac{\delta t}{\tau} (T_B - T(t)) \quad (3.35)$$

where τ is the coupling parameter between the bath and the system and T_B the temperature of the external bath. The velocities are then scaled at each time step by a quantity proportional to the difference of the temperature between the bath and the system:

$$\lambda = \left[1 + \frac{\delta t}{\tau} \left(\frac{T_B}{T(t)} - 1 \right) \right]^{\frac{1}{2}} \quad (3.36)$$

The problem with the Berendsen method is that does not generate a rigorous canonical averages, but they differ from the values of canonical ensemble typically of $\mathcal{O}(1/N)$ [77]. In most cases this accuracy is enough and the Berendsen method is indeed common used in MD simulations.

The same procedure can be used also to control the pressure of the system. As in the case of the thermostats we act on the velocities in order to keep fixed the temperature to maintain a constant pressure we need to change the volume of the system. The factor lambda in this case have to be multiplied to the volume as follows

$$\dot{\mathbf{r}}_i = \lambda^{1/3} \mathbf{r}_i \quad (3.37)$$

The Berendsen method can be applied also in this case coupling the system to a “pressure bath”, analogous to the temperature bath, thus the change of pressure can be obtained as follows:

$$\frac{dp(t)}{dt} = \frac{1}{\tau_p} (p - p_B) \quad (3.38)$$

where τ is the coupling pressure constant, p_B the pressure of the bath and $p(t)$ the instantaneous value of the pressure in the system. Volume is then rescaled by a factor:

$$\lambda = 1 - \kappa_T \frac{\delta t}{\tau_p} (p - p_B) \quad (3.39)$$

where κ_T is the isothermal compressibility describing the change of volume as response to the pressure.

$$\kappa_T = -\frac{1}{V} \left(\frac{\partial V}{\partial P} \right)_T \quad (3.40)$$

The Nosé–Hoover thermostat is a deterministic algorithm for constant-temperature molecular dynamics simulations. It was originally developed by Nosé and was improved further by Hoover. Although the heat bath of Nosé–Hoover thermostat consists of only one imaginary particle, simulation systems achieve realistic constant-temperature condition (canonical ensemble). Therefore, the Nosé–Hoover thermostat has been commonly used as one of the most accurate and efficient methods for constant-temperature molecular dynamics simulations.

3.4 Force fields and Potentials

Potential energy terms can be split in the two term relative to the intramolecular interactions (bonded interactions) and the intermolecular interactions (non-bonded interactions):

$$\mathcal{U} = \mathcal{U}_{bonded} + \mathcal{U}_{non-bonded} \quad (3.41)$$

The general form of the intramolecular part is:

$$\mathcal{U}_{bonded} = \mathcal{U}_{stretch} + \mathcal{U}_{bend} + \mathcal{U}_{torsion} \quad (3.42)$$

where $\mathcal{U}_{stretch}$ describes oscillations about the equilibrium bond length, \mathcal{U}_{bend} describes oscillations of three atoms about an equilibrium bond angle, and $\mathcal{U}_{torsion}$ describes the torsional rotation of four atoms about a central bond. Rigid potential, like the SPC/E or the TIP4P constrain the internal motions of particles.

The intermolecular part of the potential is typically written as:

$$\mathcal{U}_{non-bonded} = \mathcal{U}_{LJ} + \mathcal{U}_{Coulomb} \quad (3.43)$$

where \mathcal{U}_{LJ} is the Lennard-Jones (LJ) potential:

$$\mathcal{U}_{LJ} = 4\varepsilon \left[\left(\frac{\sigma}{r} \right)^{12} - \left(\frac{\sigma}{r} \right)^6 \right] \quad (3.44)$$

and $\mathcal{U}_{Coulomb}$ is the electrostatic potential:

$$\mathcal{U}_{Coulomb} = \frac{e^2}{4\pi\varepsilon_0} \frac{q_i q_j}{r} \quad (3.45)$$

The most consuming part of the MD simulation is the calculation of non-bonded interactions, which, in the most cases have a pairwise form. Typically, non-bonded interaction are handled with a non-bonded cutoff and with the minimum image convention. According to this convention each particle in the simulation box interacts only with the closest image of the remaining particles in the system. When the non-bonded cutoff is employed, the interaction between pairs at distance major than the cutoff value are set to zero and are therefore calculated only for distance $r = |r - r| \neq r_{cut} < L/2$, where L is the linear dimension of the box and the upper limit is introduced to avoid considering the same particle twice due to the PBC. With the introduction of the cut-off scheme for non-bonded interactions, corrections must be in general introduced in the interaction potentials [77]. For short range potential, as the Lennard-Jones potential, corrections are typically performed in the real space. For long range potential, as the electrostatic interactions, corrections are often handled in the Fourier space with the Particle Mesh Ewald method (see next section).

3.5 Ewald summation

In order to perform simulation of large system in a reasonable time there is the necessity of introduce a cutoff in the interaction. This for long range interactions, such as the electrostatic interactions, the cutoff plus corrections method (see section 3.4) have not enough accuracy. So in this case, special care is needed in dealing with potential truncation and long range contributions. It is known that the inadequate treatment of electrostatic interactions can lead to severe artifacts in the results of the simulations [79]. There exist several methods for the treatment of the electrostatic interactions. In the following the general ideas of the most used method, the Ewald summation method, are described. Taking into account the periodic boundary conditions, the electrostatic energy term of the interaction potential can be written as

$$\mathcal{U}_E = \frac{1}{2} \sum_{i=1}^N q_i \phi_E(\mathbf{r}_i) \quad (3.46)$$

and ϕ_E is given by

$$\phi_E = \sum_{j=1}^N \sum_{\mathbf{R}} \frac{q_j}{|\mathbf{r}_{ij} + \mathbf{R}|} \quad (3.47)$$

where $\mathbf{R} = \mathbf{n}L$, $\mathbf{n} = (n_x, n_y, n_z)$, with $n_x, n_y, n_z \in \mathbf{Z}$. The sum is performed with the convention that $i = j$ if $\mathbf{R} = 0$. By adding and subtracting screening charges, the sum can be broken into two parts, $\mathcal{U}_E = \mathcal{U}_{SR} + \mathcal{U}_{LR}$. The first part contains the original point charges screened by diffuse clouds of opposite charges; this part becomes short ranged and can be evaluated in the real space. The second part compensates for the added screening charges and it is generated by the sum of the screening charge densities (with opposite charge); it is evaluated in the Fourier space. The screening charges are typically taken with a Gaussian distribution:

$$\rho_s(r) = q_i \left(\frac{\alpha}{\pi}\right)^{3/2} e^{-\alpha r^2} \quad (3.48)$$

First the long range part of the sum must be calculated. Having taken the screening charges as in Eq. (3.48), the compensating charge distribution can be written as

$$\rho_c(\mathbf{r}) = \sum_{j=1}^N \sum_{\mathbf{R}} q_j \left(\frac{\alpha}{\pi}\right)^{3/2} \exp[-\alpha |\mathbf{r} - (\mathbf{r}_j + \mathbf{R})|^2] \quad (3.49)$$

and its Fourier transform is given by

$$\tilde{\rho}_c(\mathbf{k}) = \int_V d\mathbf{r} e^{-i\mathbf{k}\cdot\mathbf{r}} \rho_c(\mathbf{r}) = \sum_{j=1}^N q_j e^{-i\mathbf{k}\cdot\mathbf{r}_j} e^{-k^2/4\alpha} \quad (3.50)$$

The field generated by this charge distribution can be calculated using the Poisson's equation in the Fourier space, $k^2 \tilde{\phi}(\mathbf{k}) = 4\pi \tilde{\rho}(\mathbf{k})$. Antitransforming the field thus obtained and plugging it into the long range part of the sum, it follows:

$$\mathcal{U}_{LR} = \frac{1}{2} \sum_{i=1}^N q_i \phi_c(\mathbf{r}_i) = \frac{1}{2V} \sum_{k \neq 0} \frac{a\pi}{k^2} |\tilde{\rho}(\mathbf{k})|^2 e^{-k^2/4\alpha} \quad (3.51)$$

where $\tilde{\rho}(\mathbf{k}) = \sum_{i=1}^N q_i e^{-i\mathbf{k}\cdot\mathbf{r}_i}$ interactions terms as the point charges at \mathbf{r}_i interact with the compensating charges also at \mathbf{r}_i . The self interactions terms represent the potential at center of the Gaussian charge distributions and they are to be subtracted from the final expression to recover the correct Coulombic energy. Now the short range part of the sum is calculated. Using the Poisson's equation in the real space $-\nabla^2 \phi(\mathbf{r}) = 4\pi \rho(\mathbf{r})$ it is possible to demonstrate that the screening potential can be written as

$$\phi_s(r) = \frac{q_i f_{er}(\alpha^{1/2} r)}{r} \quad (3.52)$$

where f_{er} is the error function. It is defined by

$$f_{er}(x) = \frac{2}{\pi^{1/2}} \int_0^x e^{-t^2} dt. \quad (3.53)$$

The self-interaction terms correspond to $\varphi_{self} = \varphi_s(0) = 2 \left(\frac{\alpha}{\pi}\right)^{1/2} q_i$ and the total self-interaction energy becomes

$$\mathcal{U}_{self} = \left(\frac{\alpha}{\pi}\right)^{1/2} \sum_{i=1}^N q_i \quad (3.54)$$

which must be subtracted from the total electrostatic energy. Using the result 4.37, the short range part of the sum can be rewritten as

$$\begin{aligned} \mathcal{U}_{SR} &= \frac{1}{2} \sum_{\mathbf{R}} \sum_{i \neq j}^N q_i q_j \frac{1 - f_{er}(\alpha^{1/2} |\mathbf{r}_{ij} + \mathbf{R}|)}{|\mathbf{r}_{ij} + \mathbf{R}|} = \\ &= \frac{1}{2} \sum_{\mathbf{R}} \sum_{i \neq j}^N q_i q_j \frac{f_{er}^c(\alpha^{1/2} |\mathbf{r}_{ij} + \mathbf{R}|)}{|\mathbf{r}_{ij} + \mathbf{R}|} \end{aligned} \quad (3.55)$$

with the f_{er}^c is the complementary error function defined by

$$f_{er}^c(x) = 1 - f_{er}(x) = \frac{2}{\pi^{1/2}} \int_x^\infty e^{-t^2} dt. \quad (3.56)$$

Putting all the terms together the final result is obtained:

$$\begin{aligned} \mathcal{U}_E = \mathcal{U}_{SR} + \mathcal{U}_{LR} - \mathcal{U}_{self} &= \frac{1}{2} \sum_{\mathbf{R}} \sum_{i \neq j}^N q_i q_j \frac{f_{er}^c(\alpha^{1/2} |\mathbf{r}_{ij} + \mathbf{R}|)}{|\mathbf{r}_{ij} + \mathbf{R}|} \\ &+ \frac{1}{2V} \sum_{\mathbf{k} \neq 0} \frac{a\pi}{k^2} |\tilde{\rho}(\mathbf{k})|^2 e^{-k^2/4\alpha} - \left(\frac{\alpha}{\pi}\right)^{1/2} \sum_{i=1}^N q_i \end{aligned} \quad (3.57)$$

The original sum has been thus separated into two parts. The short range sum is performed in the real space while the long range sum is performed in the Fourier space. The tuning of the parameter α results particularly important in determining the convergence of the integrals. In order to get fast convergence α should be large in the real space and small in the Fourier space. A balance of these needs is usually considered and typically α is set to values of the order of $5/L$ [77], taking a number of wave vectors of the order of ten for the computation of the sums over \mathbf{k} .

3.6 The TIP4P/ICE

The TIP4P/ICE is a four sites model for the water [28]. This model is a new parameterization of the TIP4P potential that was specifically designed to represent the properties of water in the solid phases. As we have previously said there are four interaction sites. Three of them are placed in correspondence of the atoms the oxygen and the two hydrogen. The other one, often called the M site, is placed on the plane formed by the H–O–H angle and is located at the bisector of this angle. Like in the original Bernal-Fowler and TIP4P models, the O–H distance and H–O–H angle are fixed to the experimental values, respectively 0.9572 Å and 104.52° (see Figure 3.4).

The pair interactions between molecules is given by two contributions, a Lennard-Jones term and an electrostatic interaction. An important feature of this model is that the oxygen site has no charge, and contributes to the interactions only by to the LJ term. We recall now the expression for the LJ potential showed before (3.4)

$$\mathcal{U}_{LJ}(r) = 4\varepsilon \left[\left(\frac{\sigma}{r}\right)^{12} - \left(\frac{\sigma}{r}\right)^6 \right].$$

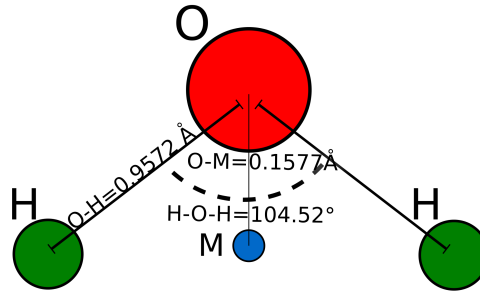


Figure 3.4: Schematic picture of a TIP4P/ICEwater molecule. The two green and the red circles represent respectively the hydrogens and the oxygen atom. The blue circle instead is the dummy sites.

where r is the distance between the two atoms. In the case of the TIP4P/ICE r is the distance between oxygen sites of two molecules. Conversely, the H and M sites are charged, but do not contribute to the LJ term. The electrostatic potential (3.45) between molecules i and j can be written as

$$\mathcal{U}_{Culomb}(r) = \frac{e^2}{4\pi\epsilon_0} \sum_{a,b} \frac{q_a q_b}{r_{ab}}. \quad (3.58)$$

where e is the proton charge, ϵ_0 is the permittivity of vacuum, and a and b stands for the charged sites of molecules i and j , respectively.

The consequence of using this potentials coupled with four sites geometry described before fix the number of unknown parameters, namely, the strength ϵ_0 and size σ of the LJ center, the hydrogen site charge or the charge of the M site, $q_H = -q_M/2$, and the distance d_{OM} between the oxygen and the M site. Table 3.1 shows the value of the different parameters of the two models TIP4P and TIP4P/ICE.

Model	σ [nm]	ϵ_0 [kcal/mol]	q_H [e]	d_{OM} [nm]
TIP4P	0.3154	0.155	0.52	0.0150
TIP4P/ICE	0.31668	0.88218	0.5897	0.01577

Table 3.1: Comparison between the value of the parameters for the two potential TIP4P and TIP4P/ICE. The values are the same of ref. [28] but are reported in unit measure used by GROMACS.

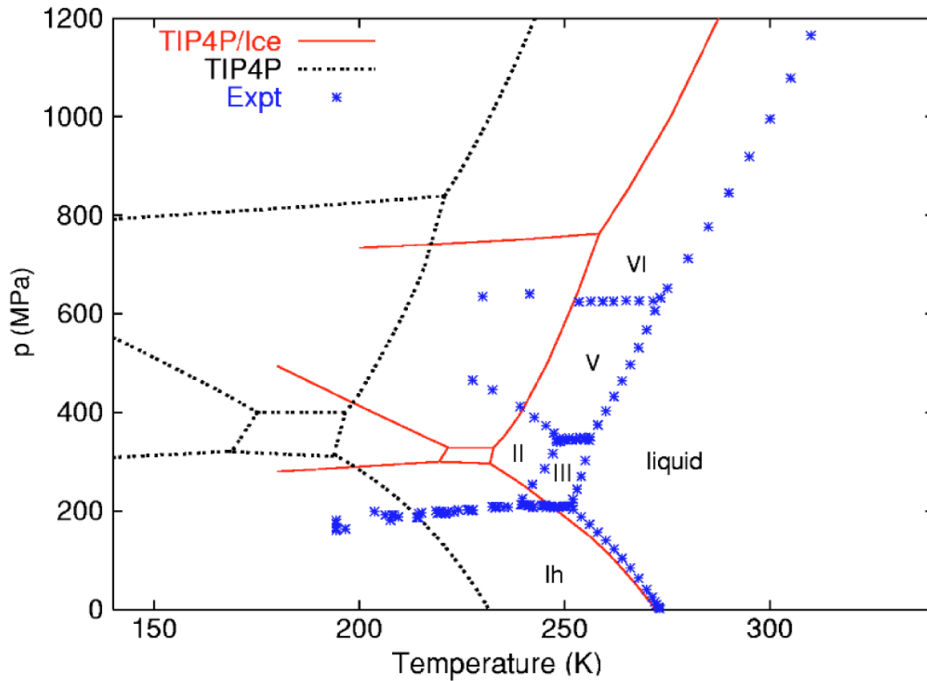


Figure 3.5: Phase diagram of the water for the TIP4P/ICE (solid red lines), TIP4P (black dashed lines) compared with the experimental data (blue stars). Figure from ref. [28]

This re-parameterization of the 4 site potential TIP4P was designed with the purpose of better reproduce the Ice phase of the water. In the figure 3.5 is shown the phase diagram of the two models TIP4P and TIP4P/ICE compared to the experimental data. As for the TIP4P potential the phase diagram of TIP4P/ICE shows all the experimental stable ices. The TIP4P/ICE however provide a better predictions for the coexistence lines which are shifted approximately 30-40 K in the direction of the experimental data. Also the values of the coexistence pressures of ice Ih-ice III, ice III-ice V, and ice V-ice VI are lower than the ones for TIP4P and are so in better agreement with the experiment.

In particular is interesting to note that at ambient pressure ($P = 1$ bar) the freezing temperature of bulk TIP4P/ICE water is $T_F = 270 \pm 3$ K [29] so only 3.15 K below the experimental value. Instead the freezing temperature for bulk TIP4P water is $T_F = 230.5 \pm 3$ K [29] so it is 39.50 K below the TIP4P/ICE freezing temperature and 42.65 K below the experimental values for the water freezing temperature.

Chapter 4

Liquid-Solid Transition Inside Single Wall Carbon Nanotube

In this Chapter results of our study on the freezing process of water inside SWCNTs are presented. In the Sec. 4.1 is given a description of the SWCNTs structure and are reported the choice made for this study for the potential parameters of nanotube. Also the technical details of the simulation can be found in this section. The Sec. 4.2 describe the analysis performed to locate the freezing temperatures of the different systems. The first analysis is the one performed on the potential energy and the second is the analysis of the behavior of the radial distribution g_{OO} , g_{OH} and g_{HH} . A comparison between our results and the ones of the literature is reported in Sec. 4.3 . Finally in Sec. 4.4 a summary of all the argument discussed in this chapter is presented.

4.1 Pure Water: Setup of the Simulation

Single Walled Carbon Nanotube

A Single Walled Carbon Nanotube (SWCNT) can be conceptualized as a slice of graphene wrapped forming a seamless cylinder (see Fig. 4.1). Each nanotube can be identified by the way in which the graphene sheet is cut before wrapping. To obtain a seamless cylinder the cut must be a linear combination of unit vectors \mathbf{a}_1 and \mathbf{a}_2 . For a two dimensional hexagonal lattice the base vectors are:

$$\mathbf{a}_1 = \sqrt{3} a (1, 0); \quad (4.1)$$

$$\mathbf{a}_2 = \frac{\sqrt{3}}{2} a (1, -\sqrt{3}); \quad (4.2)$$

where $a = 0.142$ nm is the value for the lattice space between the carbon atoms (the length of the side of the hexagon) [80,81]. Stated the equations 4.1 and 4.2 a generical cut C can be write in the form

$$\mathbf{C} = n \cdot \mathbf{a}_1 + m \cdot \mathbf{a}_2. \quad (4.3)$$

The integers n and m denote the linear combination of the unit vector. We can classify each different geometry of a SWCNT with this couple of indices (n, m) . For an (n, m) SWCNT we can calculate the value of the diameter starting from the Eq.(4.3). The circumference of the nanotube will be equal to the modulus of the vector that describe the cut $Cr = |\mathbf{C}|$ and consequently

$$d = \frac{Cr}{\pi} = \frac{\sqrt{3}}{\pi} a \sqrt{n^2 + nm + m^2}. \quad (4.4)$$

In this work we used a particular choice for this two indices, we set $m = 0$ producing what is called a *zigzag* SWCNT. The diameter of the nanotube for this configuration is given by the value of n through the relation

$$d = \frac{\sqrt{3}}{\pi} a \cdot n, \quad (4.5)$$

One of the most important implication of the equation (4.4), and also of the Eq. (4.5), is that we cannot change continuously the diameter of the SWCNT in order to produce a completely ordered structure.

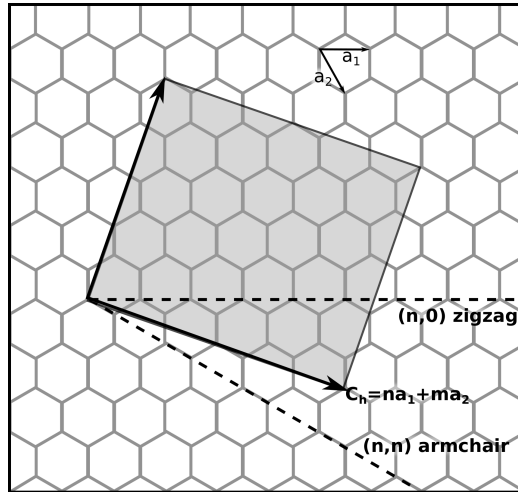


Figure 4.1: Example of a generic cut C_h of the honeycomb lattice of graphene to form a SWCNT. In this figure there are also reported the cuts that produce the two most common configurations, *zigzag* and *armchair*.

After the sheet was wrapped the two long side of the rectangular sheet are joined to form a seamless cylinder. The two extremes of the nanotube are formed by the carbon atoms that are on the short edge of the sheet. This atoms presents dangling bonds that we saturated with hydrogens as common practice [82,83]. In Fig. 4.2 is reported a snapshot of a SWCNT used in the simulation in wich it is possible to see the presence of the hydrogen that saturete the dangling bond.

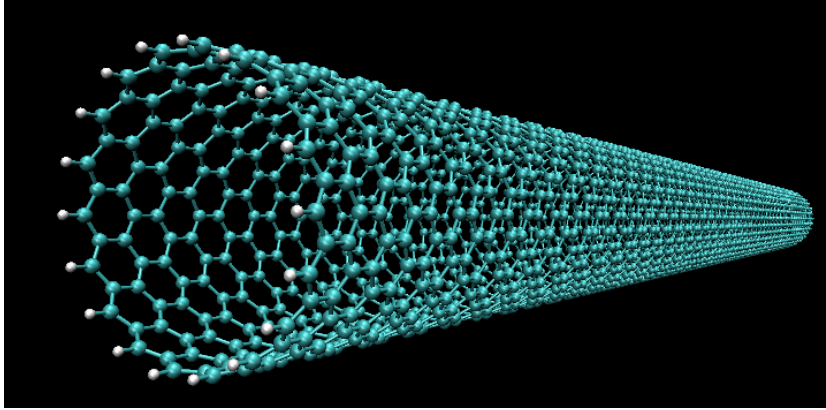


Figure 4.2: Snapshot of a zigzag SWCNT with $n = 18$. The cyan spheres are the carbon atoms that lay on the the hexagonal lattice sites. The white spheres are the hydrogens that saturate the dangling bonds.

Graphene is a very stable material and interacts very weakly with external molecules. For this reason we choose, as also done in literature [25], to reproduce the interactions of the SWCNT and the water molecules a Lennard Jones (3.4). We used the OPLS all atom potential parameters [84] to simulate the SWCNT interaction between the nanotube and water. The SWCNT lattice was kept rigid. The details of the potential parameters used for this work can be found in Tab. 4.1 in the next section.

Simulation Details

The nanotube previously described was inserted in a water box, so that the SWCNT was completely surrounded and filled by water molecules as it is possible to see from Fig. 4.3. The water molecules in our system are described by the TIP4P/ICE potential [28]. The details of this potential was provided in the previous chapter in the Sec. 3.6. The Lennard Jones potential parameters (see eq.3.4) that we have used in our simulations, for both water and SWCNT, are reported in Tab. 4.2. The cross-interaction parameters are calculated with the Lorentz-Berthelot mixing rules.

Table 4.1: Lennard Jones parameters and value of the charges of the SWCNT and the TIP4P/ICE.

	Atom	σ [nm]	ϵ [kcal/mol]	$q[e]$
SWCNT	C	0.355	0.29288	–
	H_C	0.242	0.12552	–
Water	O	0.31668	0.1061	–
	H_W	–	–	0.5897
	M	–	–	–1.1794

We have studied water inside SWCNT for different sizes of the nanotubes. In Tab. 4.2 we report the characteristics of the different systems that we have studied: the diameter (d), the length (L) of the SWCNT, the number of water molecules N_W and the size of the initial simulation box. We reported also the value of the parameter n that is linked to the diameter of the SWCNT by the relation 4.5. The axis of the cylinder was oriented in our simulation parallel to the y axis. In all the cases the length of the SWCNT is much longer than the diameter.

We performed the simulations using the software GROMACS (version 5.0.7) [85], running the program on 8-core computer and on the INFN-Grid Roma Tre cluster¹.

The simulation box size was changed depending on the nanotube diameter in order to have the smallest box that still allows the water molecules to surround the SWCNT. Periodic boundary conditions along all the three axes were applied in all simulations. An example of a simulation box is reported in Fig. 4.3 for the system with a diameter of $d = 1.213$ nm.

We performed MD simulations of 5 pores with different diameters. For each pore we simulated from 20 to 36 different temperatures. Starting from the temperatures T_{max} reported in Tab. 4.2 we cooled each system with step of 10 K simulating a total of 130 state points for this study.

We performed our simulations in the isothermal-isobaric ensemble (NpT), that was described in the previous chapter 3.1. For each diameter chosen for the SWCNT we started from a high temperature where water is liquid inside the SWCNT. Each system was cooled until the same final temperature of 150 K, cooling the system with step of 10 K. The starting and the final temperatures for each system are reported in Tab. 4.2. We cooled each system along the $p = 1$ bar isobar. For each temperature we reach equilibrium using the Berendsen thermostat. For the pressure control we use the

¹<http://web-cluster.fis.uniroma3.it/>

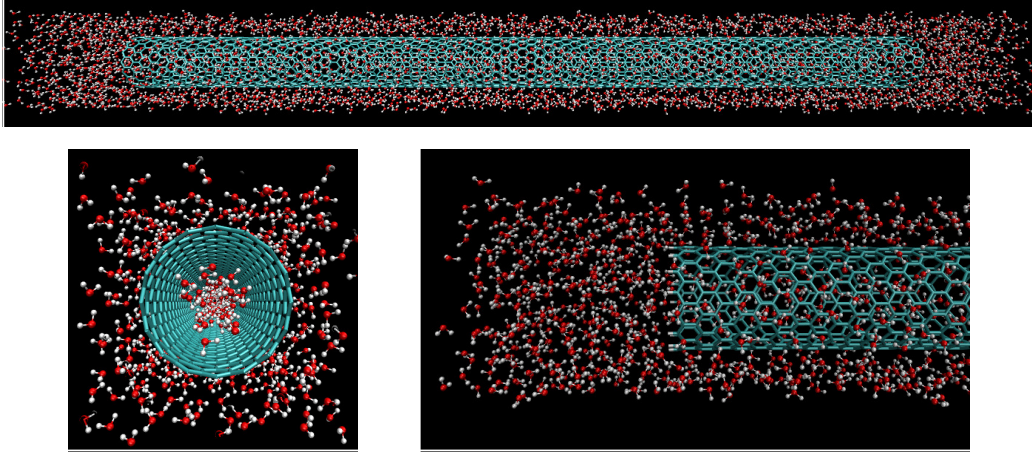


Figure 4.3: *Snapshots of the system with a SWCNT of diameter $d = 1.213$ nm ($n = 16$) for the equilibrated sample at the highest temperature investigated, $T = 450$ K. The three snapshots represent respectively, the side view of the whole simulation box (top figure), a cut and blow up of the frontal view (bottom left figure) and a cut and blow up of the side view (bottom right figure).*

Parrinello-Rahman barostat, since it suited to study the crystal structure.. The description of this thermostat and barostat can be found in the Sec. 3.2 . Since the simulations of such a large system are rather time consuming, we used the shifted force method with a cutoff at 0.9 nm for all interactions. Particle-Mesh Ewald (PME)(see Sec. 3.5) was used to determine the long range forces in the systems.

The typical time required for the dipolar reorientation of water molecules inside SWCNT has been reported to be in the order of 0.7 picoseconds [86], for this reason we choose a time step of 0.001 ps for our simulations. The length of each simulation run is 5 ns, major details on the simulations can be found in Tab. 4.2 .

The total computational time amounts to about 650 ns for the isobar of the five systems. The simulations were carried out on 8-core computer and on the INFN-Grid Roma Tre cluster² where we achieved an average simulation times that go from 12 ns/day for the system with the smaller diameter to 7 ns/day for the system with larger nanotube. After each run of equilibration a production run of 100 ps was performed to obtain the data used for the analyzes of the next section.

Table 4.2: Specifications of the different simulated systems. d is the diameter of the nanotubes. T_{max} and T_{min} are respectively the maximum and the minimal temperatures from which each system is cooled along the $p = 1$ bar isobar. N_r is the number of run performed at different temperatures, t_e is the time of each equilibration run and TOT t_e is the total time simulated. t_p is the length of the production run use to produce the data analyzed in the follow. L is the length of the nanotube, n is the structure index, N_W is the number of water molecules contained in the simulation box, N_C is the number of carbon atoms that form the SWCNT, and x , y and z are the lengths of the simulation boxes for the highest temperature investigated.

	d [nm]				
	0.978	1.056	1.213	1.291	1.369
T_{max} [K]	350	500	450	350	340
T_{min} [K]	150	150	150	150	150
N_r	21	36	26	21	20
t_e [ps]	5000	5000	5000	5000	5000
TOT t_e [ns]	105	180	130	105	100
t_p [ps]	100	100	100	100	100
L [nm]	19.246	19.246	19.246	19.246	19.246
n	13	14	16	17	18
N_W	1884	2624	2979	3213	3469
N_C	2340	2520	2880	3060	3240
x [nm]	2.018	2.096	2.252	2.330	2.410
y [nm]	23.282	23.438	23.750	23.906	24.066
z [nm]	2.018	2.096	2.252	2.330	2.410

4.2 Crystallization of water inside the SWCNT

In this part of the work we want to focus on the study of water liquid-solid phase transition inside SWCNTs. For this reason, we consider for the analysis of results only the water molecules present inside the SWCNT. To do that we take advantage of the extremely regular shape of the nanotube. Knowing the diameter and the length of the SWCNT (see Tab. 4.2) it is simple to establish from the coordinate of the different water molecules if it belongs or not to the interesting region of the system.

In order to find the temperature of crystallization of the water inside the SWCNT we choose to perform two distinct analyses. First of all we studied the trend of the potential energy, and then we have analyzed the behavior of

radial distribution functions of the inner water molecules.

Potential Energy Behavior

In Fig. 4.4 we can see the behavior of the potential energy of the water molecules that are inside the SWCNT at different temperatures. We identify the temperature where water freezes inside the SWCNTs, T_F , as the temperature where the potential energy shows a drastic change. When the system reach T_F the trend of the potential energy reported in Fig. 4.4 shows not only an abrupt decrease but also a changing in the slope.

It is interesting to note that for the four larger nanotubes the curves at low temperatures collapse on the same line, while the curve of the potential energy of water inside the smallest SWCNT is quite different. As was described in the Sec. 3.1, the potential energy of the system is the sum of the of radial potential between pairs of atoms. This mean that for systems that shows a similar behavior we expect to observe some similitude in the ice structure. Instead the water inside the smallest nanotube will probably shows a different structure. We will return on this point in the next chapter when we discuss about the formation of the so called “ice nanotube”.

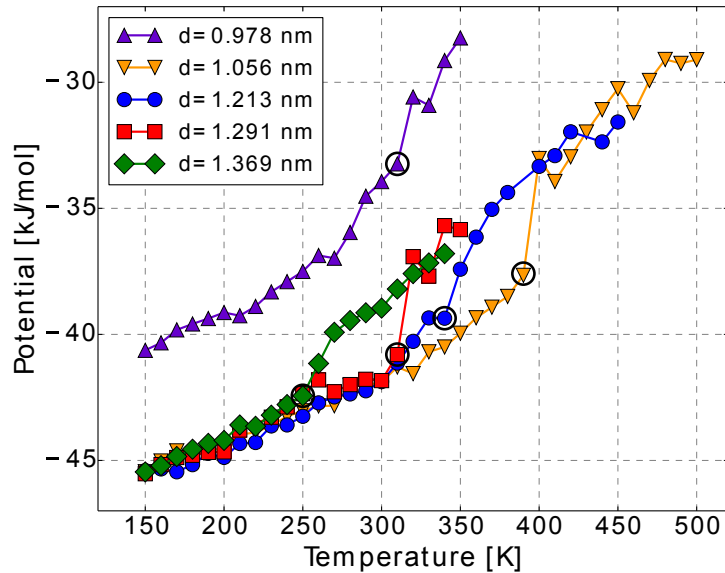


Figure 4.4: Potential energy of the water molecules that fill the SWCNTs as a function of the temperature T . The different curves are relative to the different diameters of the nanotube as reported in the legend. The black empty circle marks the freezing temperature.

Radial Distribution Functions

To support the results obtained for the potential energy we have studied also the behavior of the radial distribution functions of our systems. In Fig. 4.5 we report as an example the $g(r)$ for oxygen-oxygen, oxygen-hydrogen and hydrogen-hydrogen relative to the inner water of the nanotube with a diameter of $d = 1.291$ nm ($n = 17$) at the different temperatures investigated.

The analysis of the radial distribution function needed a more delicate approach. In fact it is known in literature that the $g(r)$ obtained by a molecular dynamic simulation in a confined system are generally different from the ones obtained in bulk water. In order to normalize the $g(r)$ in the correct way [87,88].

It is known that from simulation we can calculate the average number $n_{ab}^{(2)}(r)$ of atoms (or sites) b that are found in a spherical shell at distance r from an atom (or site) a . If $\Delta v(r)$ is the volume of the spherical shell we can calculate the *spherical* function

$$g_{ab}^{(s)}(r) = \frac{n_{ab}^{(2)}(r)}{n_b \cdot \Delta v(r)} \quad (4.6)$$

where $n_b = N_b/V_c$ is the density of the atoms (or sites) b in the cell of volume V_c . This quantity represents the deviation of the distribution of the interacting particles with respect to the ideal gas distribution in the spherical shell. In applying Eq. (4.6) The normalization of the $g_{ab}^{(s)}(r)$ is usually performed by assuming an homogeneous distribution of the particles in all the directions. In a normal simulation cell with periodic boundary conditions applied in all the directions this is a good approximation and $g_{ab}^{(s)}(r)$ coincides with the ab radial distribution function.

When we calculate a $g_{ab}^{(s)}(r)$ in a confined geometry that is non homogeneous in all the three directions, like our case, there is an excluded volume that is not taken in to account during the normalization.

More in general it must taken into account that the homogeneous distribution must be corrected with a function $g_u(r)$, the uniform distribution of ideal gas atoms inside a confined cell of simulation. Of course $g_u(r) = 1$ in the normal case, but for confined geometries the $g_u(r)$ must be evaluated.

In our case we must take into account the cylindrical geometry in which the water is confined. For this reason we approximated $g_u(r)$ as the Fourier transform of a cylindrical form factor. The site-site RDF can be obtained as

$$g_{ab}(r) = \frac{g_{ab}^{(s)}(r)}{f_c(r) \cdot g_u(r)} \quad (4.7)$$

where $f_c(r)$ is a correction factor. This latter function accounts for the uncertainty in the volume and the presence of periodic boundary conditions along the y direction. By imposing that the RDF must go asymptotically to oscillate around the constant unity value it is possible to find that $f_c(r)$ is an asymptotic linear correction weakly dependent on r . It is important to note that is useful investigate the $g(r)$ also when r became larger than the pore size because it give information also on the longitudinal distribution of the molecules. However since we set our cutoff in the interactions at 0.9 nm the $g(r)$ for $r > 0.9$ dose not provide useful informations.

In the Fig. 4.5, and in the following figures showing the radial distribution functions, we report directly the corrected functions. However we report in the inset of the top subfigure of Fig. 4.5 an example of a non-normalized oxygen-oxygen $g(r)$, for the highest and the lowest temperature investigated. In the inset we can observe that non-normalized $g(r)$ go to 0 upon the increasing of r , as we stated previously this is the effect of the exclude volume.

In Fig. 4.5 we can observe that for all the three $g(r)$ at the temperature $T_F = 310$ K sharp peaks abruptly arise. This temperature is the same where the potential energy behavior has a drop. This is a proof that there is a connection between the structures and the potential. The rise of these peaks is the proof of the formation of an ordered structure of the water molecules that are inside the nanotube.

The first peak in the g_{OO} is placed at $r = 0.279$ nm that is the standard distance of the hydrogen bond [89]. The presence of the HBs is also confirmed by the presence of th first peak in the g_{OH} . From this points we can conclude that the confinement dose not prevent the formation of an hydrogen bond network. The best evidence of the liquid solid transition in the $g_{HH}(r)$ where the changing is more evident. However in all the radial distribution functions the peaks are sharp and well defined.

From the $g_{OH}(r)$ and $g_{HH}(r)$ arise two of the important features that characterize the structure of the system. The first is the shoulder that the $g_{OH}(r)$ present near the second peak, the other is the presence of a second peaks of the $g_{HH}(r)$ extremely close to the first one. This feature was never observed in the other seventeen form of ice previously described. This feature will be discussed in detail in the next chapter.

The same phenomenon happens for all the different sizes of the nanotubes. In Fig. 4.6 we show the radial distribution functions $g_{OO}(r)$ $g_{OH}(r)$ and $g_{HH}(r)$ for all temperatures investigated and for all the different sizes of the SWCNT simulated. The abrupt change of structure with the appearance of sharp peaks always happens in correspondence with the temperatures highlighted in the Fig. 4.4 that correspond to the sharp drop of the potential energy. This finding confirms that those temperatures can be taken as the

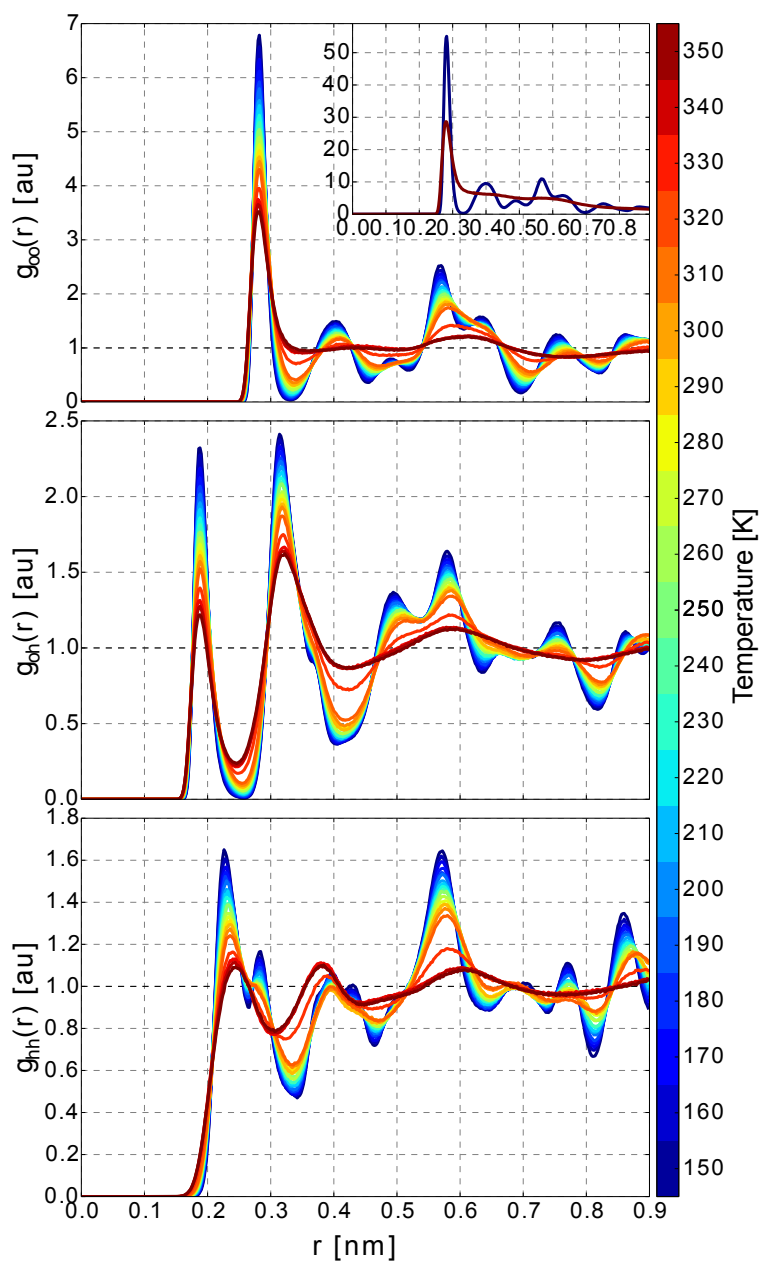


Figure 4.5: Oxygen-oxygen, oxygen-hydrogen, and hydrogen-hydrogen radial distribution function for different temperatures for the nanotube with a diameter of 1.291 nm for this system $T_F = 310$ K. In the subplot of the top figure are reported two $g_{OO}(r)$ without the correction on the normalization relative to the highest temperature (350 K) and the lowest temperature (150 K). In the color maps on the right it is possible to see the relation between the color and the temperature.

freezing temperatures of water in the different nanotubes.

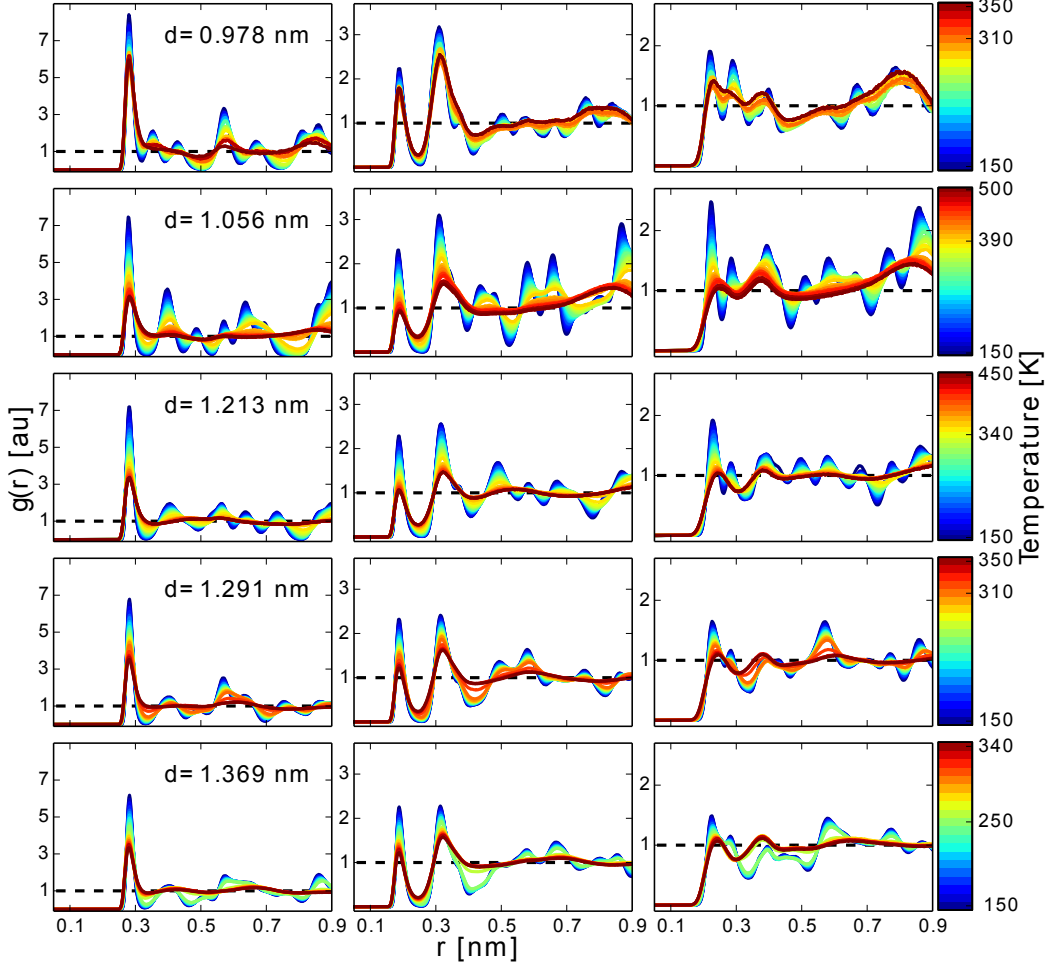


Figure 4.6: Oxygen-oxygen (left column), oxygen-hydrogen (center column) and hydrogen-hydrogen (right column) radial distribution functions for different temperatures for all the nanotubes investigated spanning from a diameter of 0.978 nm (top row) to a diameter of 1.369 nm (bottom row). In the color maps on the right it is possible to see the relation between the color and the temperature. The temperatures labeled in the color maps are respectively, T_{max} , T_F and T_{min} .

4.3 Analysis of the Freezing Temperatures

The freezing temperature observed with the two studies previously illustrated give the same results. The list of all the freezing temperatures as a function of the diameter investigated is reported in the Table 4.3. The first things

that we note is that the freezing temperature present a maximum values for $d = 1.056$ nm. It is really interesting to note how the freezing temperature increases when the pore becomes smaller, with the exception of the smallest one $d = 0.978$ nm, that has a T_F lower than the next larger one. This shows, together with the different qualitative behavior of the potential energy, that there is a cross over in the behavior of the water inside the nanotube around $d = 1$ nm.

Table 4.3: Freezing temperatures (T_F) for the different diameter (d) of the nanotubes.

d [nm]	0.978	1.056	1.213	1.291	1.369
T_F [K]	310	390	340	310	250

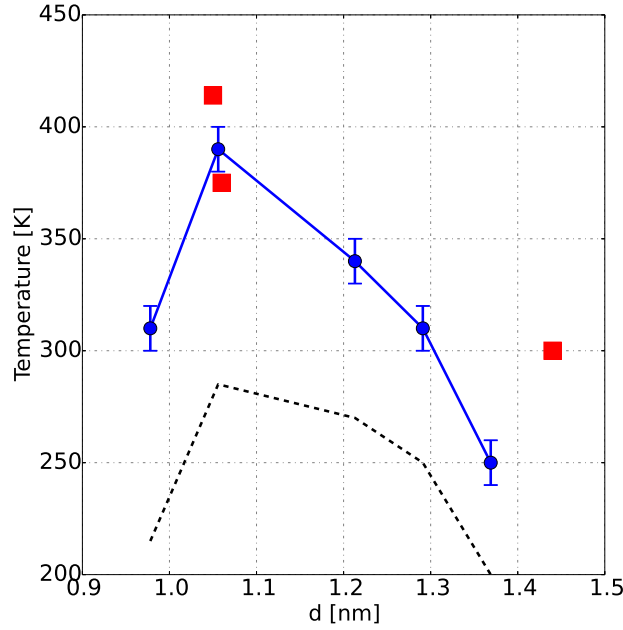


Figure 4.7: Freezing temperatures of water in SWCNTs obtained from our simulation data using TIP4P/ICE water (filled circles and continuous line), simulation data with TIP4P water reported by Koga *et al.* [25] (dashed line) and compared with experimental data given by Varoon *et al.* [26] (filled squares).

As was previously stated (see Sec. 3.6) we used for this simulation an extremely realistic potential for water, the TIP4P/ICE. For this potential the freezing temperature of bulk water is $T_F = 270 \pm 3$ K for $P = 1$ bar [29] so only 3.15 K below the experimental value. As can be seen in Table 4.3,

the freezing temperatures inside the SWCNT can happen, depending on the diameter of the nanotube, at much higher temperatures with respect to the bulk water.

We compare now the results of three freezing temperatures, for three different diameter of the SWCNTs, just recently measured by the Strano team at MIT [26] with our freezing temperatures and with the results of the freezing temperatures calculated in the pioneering paper by Koga *et al.* [25] using TIP4P water. We recall here that the freezing point of TIP4P bulk water is $T_F = 230.5 \pm 3$ K [29] so it is 42.65 K below the experimental water. Agrawal *et al.* [26] unexpectedly and interestingly found, for SWCNT and diameters of 1.05 nm and 1.06 nm. freezing temperatures close to and one even higher than the boiling temperature of bulk water. In Fig.4.7 we report these data. As we can see our qualitative trend of the freezing temperatures as a function of the pore diameter is similar to the Koga *et al.* results. Nonetheless the use of the TIP4P/ICE model gives results in much better quantitative agreement with experiments especially for the $d = 1.056$ nm SWCNT and succeeds in reproducing the interesting experimental high freezing temperatures. This confirms that the use of a potential that better reproduces the experimental freezing point in bulk water gives results in close agreement with experiments also inside the nanotube. The lines show a maximum and for the smallest diameter investigated the freezing temperature goes down showing a change of trend for the smallest pore as already previously noted.

4.4 Conclusions

In this chapter we have show our studies on the freezing process of water inside SWCNT. We extract the information about the freezing temperature from the behavior of the potential energy and from the study of the radial distribution function. Both this quantities shows a changing in the behavior when the temperature gos below the T_F value indicated in Tab.4.3. The comparison between our results with the pioneering work of Koga *et. al* [25] and the very recent experimental paper [26] shows how the use of a more realistic potential can provide better results. Our simulation performed with the TIP4P/ICE potential give results extremely in agreement with the experimental results as it is possible to see in Fig. 4.7 .

We also noticed that the behavior of the water inside the smallest nanotube seems to be quite different. This is probably due to a difference in the structure that water form inside the SWCNT with that diameter. We will discuss this issue in the next chapter where we go deeply in the analysis of the structures.

Chapter 5

Structure of Ice Nanotube

In this Chapter we presents our results on the study performed on the structures that water forms inside SWCNTs when freezes. The analysis performed in this chapter are performed on the same dataset of the previous one. An analysis on the distribution of the water molecules along the isobar inside the SWCNT is presentend in Sec. 5.1 . In Sec. 5.2 we present the results on our structures comparing our $g(r)$ with the theoretical structure of an ice nanotube. We face the issue of the proton ordering in the Sec. 5.3 . Using the radial distribution functions we can have a clue on the hydrogens behavior in the “ice nanotube”. Finally in Sec. 5.4 a summary of all the argument discussed in this chapter is presented.

5.1 Distribution of water molecules inside the SWCNT

In order to better understand the freezing process described in the previous chapter, can be usefull focussing on the distribution of the water molecules present inside the SWCNT during the cooling. We report in in Fig. 5.1 a scatter plot that describes the distribution of the different atoms inside the nanotube.

In the Fig. 5.1 for each nanotube we show four configurations at different temperatures: the highest and the lowest investigated and the two right above and right below the transition temperature. Just below the transition temperature we can see that the system starts to show an angular ordering. In all nanotubes, except the smallest one, it can be seen that the water molecules order forming the ice structure of an ice nanotube. In the right column of the Fig. 5.1 (the one at lowest temperature) we can clearly distinguish the different spots formed by the atoms that constitute the ice ring. We can

see that the number of the atoms that form the ice rings goes from 4 to 7. Differently, the smallest nanotube does not show any preferential ordering in the angular coordinate. In order to better understand what is happening in this smaller system we cannot limit ourselves to observe the projection on the xz plane and we will see later more details on this structure.

In Fig. 5.1 we can observe that the oxygen groups are connected by groups of hydrogens, these hydrogens are the ones that form the hydrogen bond between two water molecules of the same ring. The second hydrogen of the water molecule forms an hydrogen bond with other water molecules belonging to another ring. We do not clearly distinguish them in this plot because these hydrogens form a spot that has the same angular coordinate of the oxygen spots and they are superimposed in the figure.

Another useful quantity to study the behavior of water upon cooling in the SWCNTs is the radial density distribution ρ :

$$\rho(r) = \frac{N(r + \Delta r)}{2\pi r \Delta r}, \quad (5.1)$$

where $N(r + \Delta r)$ is the number of atoms in the crown of internal radius $r - \Delta r/2$ and external radius $r + \Delta r/2$. The area of the circular crown is the normalization factor $2\pi r \Delta r$.

The $\rho(r)$ are reported in the Fig. 5.2, in which the distribution for the oxygen and the hydrogen atoms are represented in the filled histogram and the sum of the two distributions is represented in the empty histogram.

For each nanotube we show the same temperatures of the Fig. 5.1 in order to compare the two figures. The black vertical line represent the wall of the SWCNT and the shaded region is the space outside.

In Fig. 5.2 we can clearly distinguish for each row in the four panels the two phases of water. If we look at the total radial density distribution we see that at high temperatures (leftmost panel) the water is in the liquid phase and the very central part of the SWCNTs is more filled by water molecules. We can observe that the hydrophobicity of the SWCNT creates an empty space between water molecules and the SWCNT internal surface. This implies that the accessible space for the water molecules is less than the diameter of the nanotube. At the lowest temperature the crystallization is complete and we see a single peak between the center and the wall of the nanotube. The largest pore still shows some defects, visible also in the projected snapshots of Fig. 5.1, even for the lowest temperature investigated.

In Fig. 5.2 we also report the radial density distribution $\rho(r)$ of the hydrogens and the oxygens separately in order to highlight the relative positions of the atoms. We can observe that in the plot at the lowest temperature $T = 150$ K there are two distinct peaks for the hydrogens distribution. One

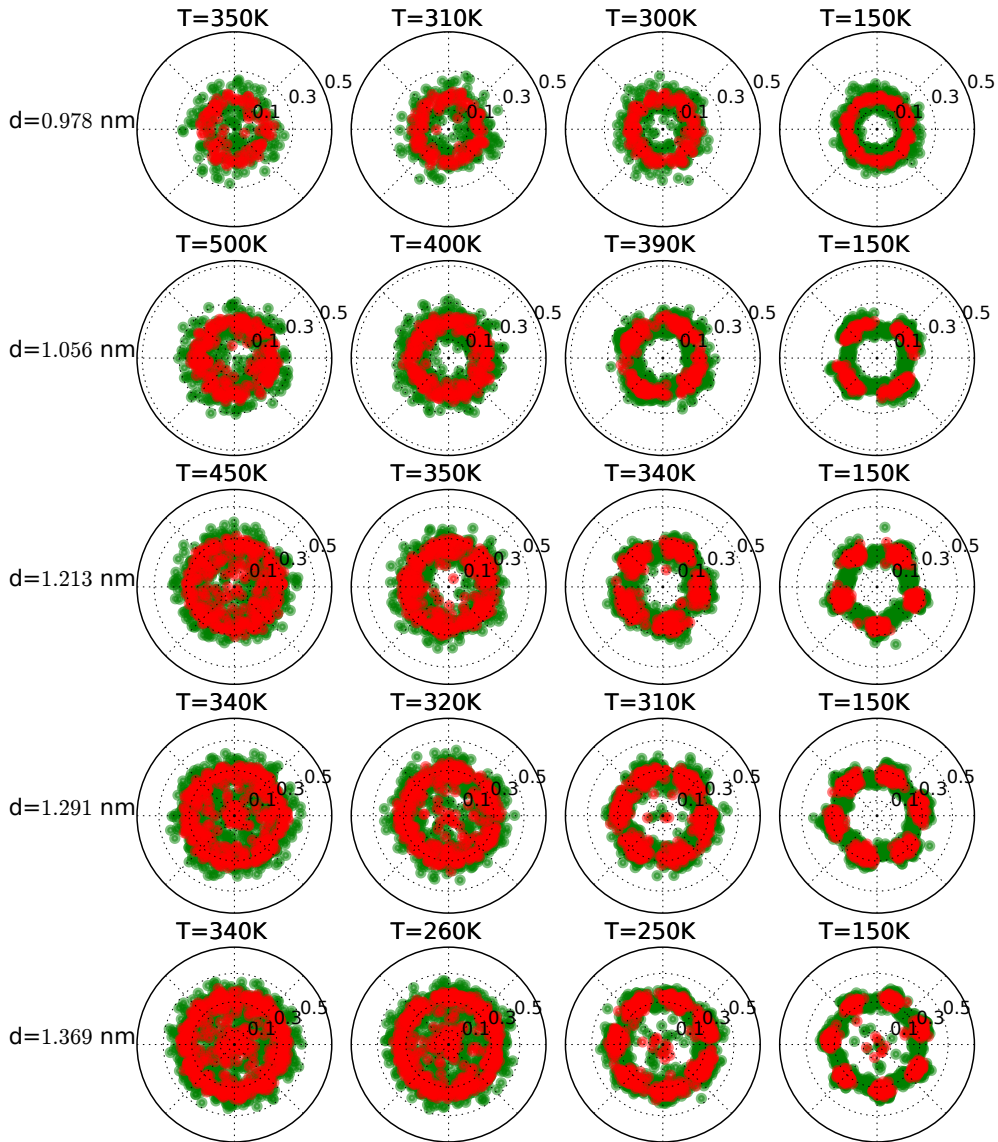


Figure 5.1: Scatter plot of the different steps in the cooling process for each diameter of SWCNT studied. The red points are the oxygen atoms and the green ones are the hydrogen atoms. In this plot each point is the projection of the coordinate of atom on the axial plane xz that is the transverse plane. In the left column we can see the system at the higher temperature where water is in the liquid phase. In the two central column we can see the systems just before (center left) and just below (center right) of the transition. In the right column we can see the system at the lowest temperature investigated ($T = 150$ K) that is the same for all the systems.

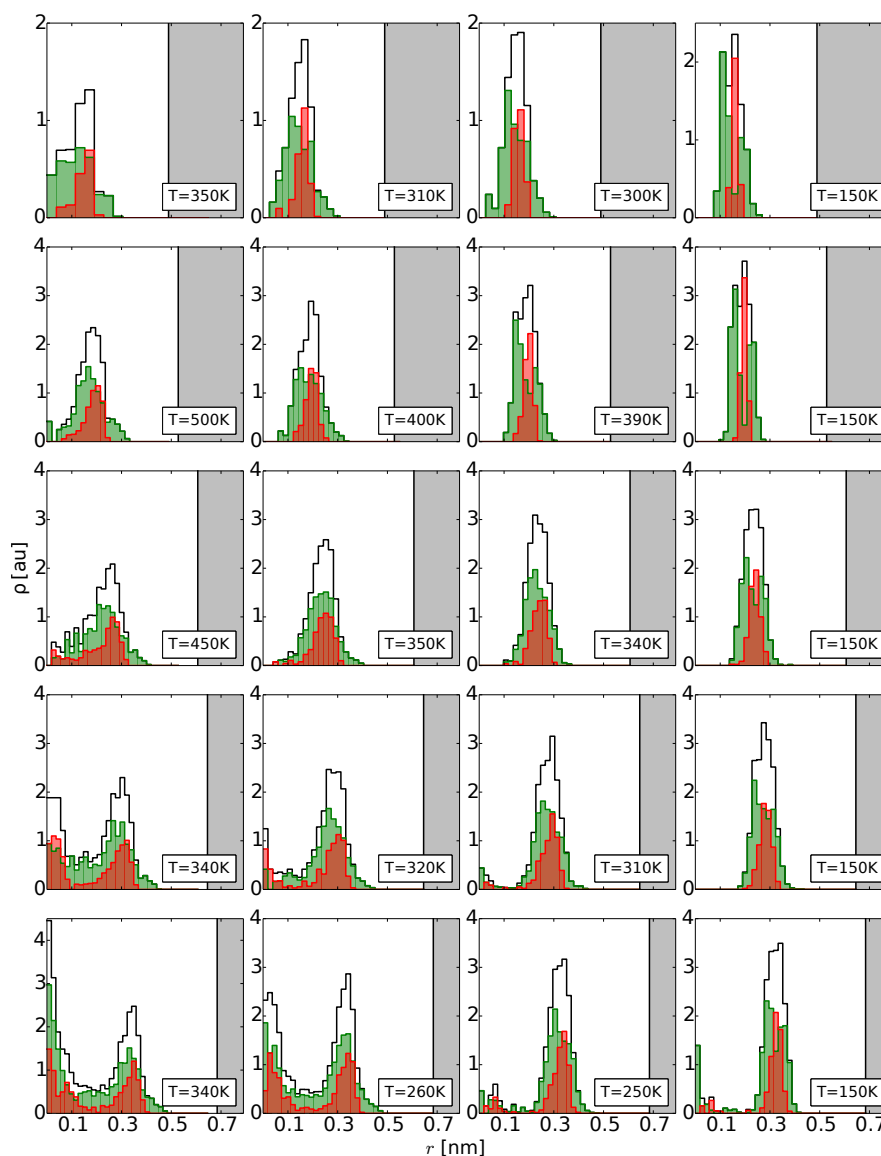


Figure 5.2: Radial density distribution of the water atoms. The red filled histograms are relative to the distribution of the oxygen atoms, the green filled histograms are relative to the distribution of the hydrogen atoms and the black empty histograms are relative to the distribution of all the atoms. Each row corresponds to a different diameter of the SWCNT investigated for four selected temperatures: the highest temperature, the closest temperature before freezing, the freezing temperature (T_F) and the lowest temperature. The white regions in the figures are the internal part of the nanotubes.

of these two peaks is closer to the center with respect to the oxygen peak, the other instead is closer to the SWCNT surface. The two peaks are relative to the two hydrogens of the water molecules and represent the radial position of the hydrogen bonds in the ice structure. As we will see better in the last part of this work, the external hydrogens are the ones that form the hydrogen bond between two adjacent rings while the internal ones are related to the intra-ring hydrogen bond. From Fig. 5.1 and Fig. 5.2 we see that the water molecules show a layering effect due to the SWCNT confinement at high temperatures and for the bigger pores.

5.2 Ice Nanotube

In the Fig. 5.3 it is possible to see the snapshots of the ice structure crystallized from liquid water in all the nanotubes of different size that we have investigated. All the snapshots are taken at the same temperature of $T = 150$ K that is the lowest temperature that we have simulated.

We can see that water inside nanotubes of diameter larger than 1 nm (from the second to the fifth row) forms an ordered stack of rings when it crystallizes. When the diameter of SWCNT grows the water rings become larger passing from rings formed by 4 molecules up to rings formed by 7 molecules. In this Fig. 5.3, it is clearly visualized, similar to what observed in the Fig. 5.1, that the water molecules that form the rings have two hydrogen bonds, one with a water molecule of the same ring and another one with an oxygen belonging to one of the two adjacent rings. Within the same nanotube in each ring there is always an hydrogen bond between two adjacent molecules, so these hydrogen bonds always point to the adjacent molecule. However, the hydrogen bonds between different rings present disordered orientations.

In the smallest nanotube ($d = 0.978$ nm) it is not observed the planar ordering of the water molecules that characterizes the structures at larger diameters. For this size of nanotube the ice structure is formed by three chains of water molecules twisted together and forming a spiral. This crossover at smaller diameters in the structure of ice is possibly connected to another interesting result. Thomas and McGaughey [14] in their pioneer theoretical work and X. Qin *et al.* [90] in their experimental work proved in fact that there is a crossover in the the flowing behavior of liquid water at exactly the diameter where we have a crossover in structure, namely 1 nm.

Our ordered structures are in agreement with those found in literature on this kind of SWCNT using different model potentials for water, see for example TIP4P [25], SPC/E [24]. This proves that the results on the structure of

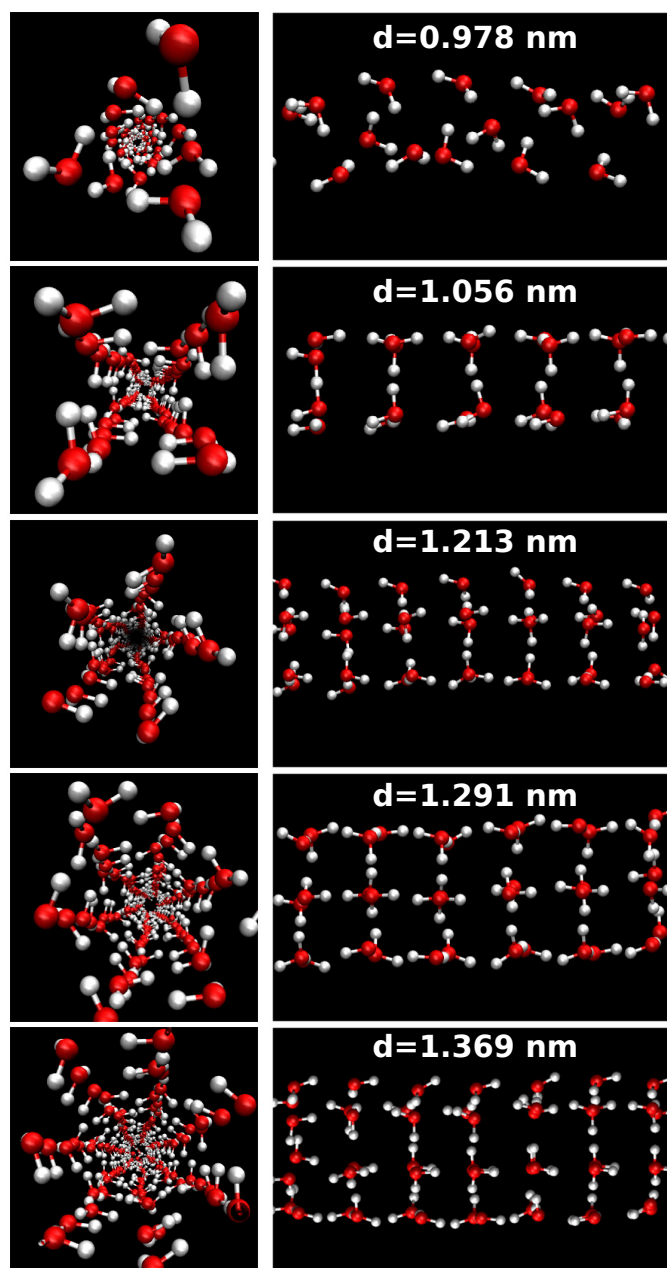


Figure 5.3: Snapshots of the ice structures obtained inside the SWCNT from our simulation results. All the snapshots are relative to the same temperature at 150 K and each row corresponds to a different size of the SWCNT. Frontal view (left) and side view (right) are shown.

the ice nanotubes are very robust, including the crossover in structure type for diameters below 1nm.

All the ice nanotube showed in Fig. 5.3 seems to share common features. In their pioneering work Koga *et al.* [23]. proposed that similarly to what happen for the SWCNTs the ice nanotube can be obtained by slicing a 2D lattice and than wrapping. If for the SWCNTs the starting lattice is the graphene one for describe ice nanotubes we need to start from a square lattice as shown in Fig. 5.4 .

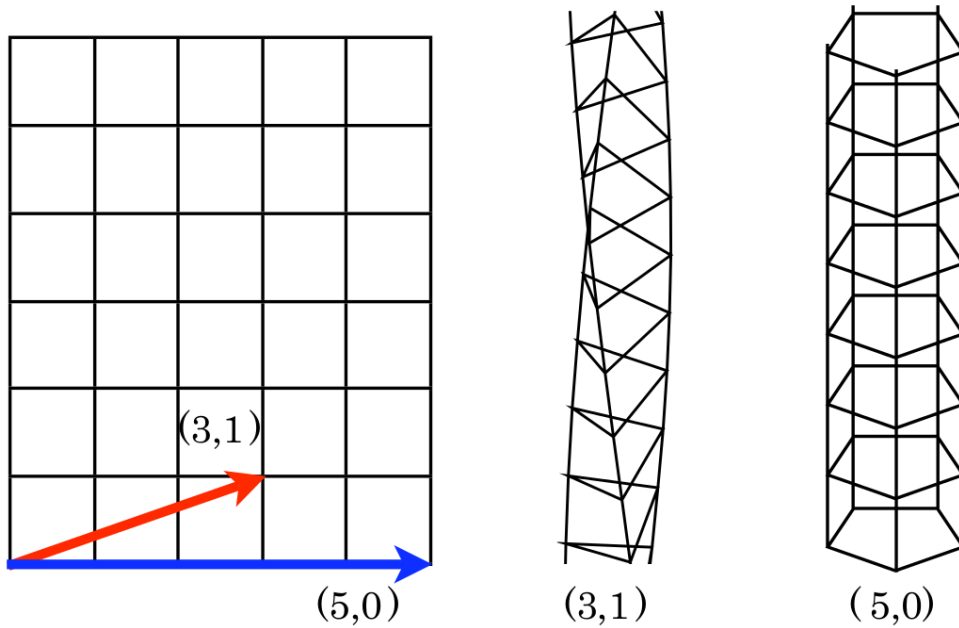


Figure 5.4: cartoon of a square lattice with the cut necessities to create the two folded structures presented on the right. Figure from [23]

In order to better understand the structure of the ice nanotubes we compare the oxygen-oxygen radial distribution function reported in the Fig. 4.5 with a cartoon of the ice structure obtained for the system with a diameter $d = 1.291$ nm.

This comparison is given by Fig. 5.5. In the cartoon we can see the equilibrium positions of the oxygens. The cartoon was made using the idea of Koga *et al.* [25] of starting from a square lattice. Assuming that the value of the nearest neighbors distance for two oxygen atoms is defined by l we can consequently calculate the other distances. The result of the distances calculation for the nearest atoms is reported in Tab. 5.1 .

Given the value of l , all the other distances are fixed by the geometry of the system. We can obtain the value of the nearest neighbors distance l by the first peak of the oxygen-oxygen $g(r)$. In Fig. 5.5 it be can seen how

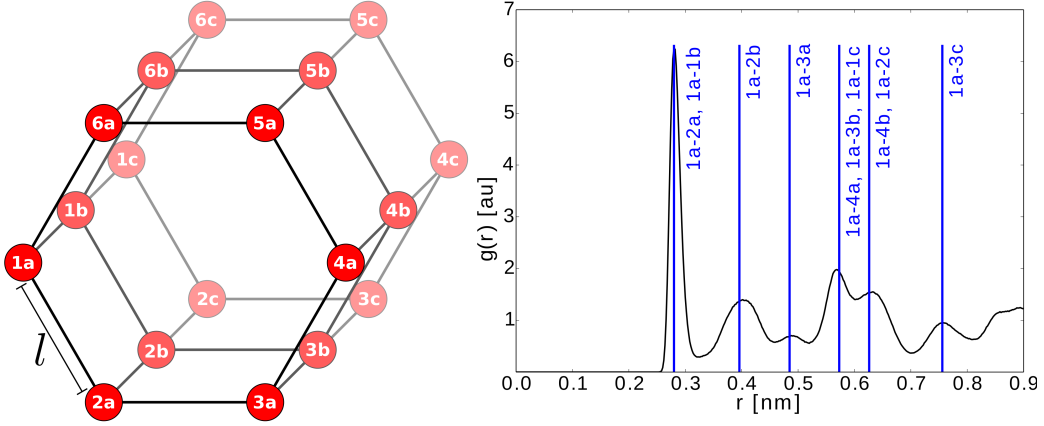


Figure 5.5: (Left) cartoon of the oxygen positions in a hexagonal ice nanotube. The distance between the two nearest oxygens is defined by l . This distance is the same for all the oxygens represented. The letters (a,b,c) correspond to the different rings and the numbers (1-6) refer to the position of the oxygens in each ring. (Right) $g_{OO}(r)$ as obtained by our simulations at $T = 150$ K for the $d = 1.291$ nm SWCNT. The blue vertical lines correspond to the oxygen-oxygen distances reported in the Tab. 5.1. Numbers and letters for each vertical line correspond to the distances in the lattice indicated in the top panel.

Table 5.1: Value of the distance between two different oxygen in the structure of hexagonal ice nanotube. The labels of the position are relative to the cartoon in Fig. 5.5.

Distance	Value
$1a - 2a$	l
$1a - 2b$	$\sqrt{2} \cdot l$
$1a - 3a$	$\sqrt{3} \cdot l$
$1a - 4a, 1a - 3b, 1a - 1c$	$2 \cdot l$
$1a - 4b, 1a - 2c$	$\sqrt{5} \cdot l$
$1a - 3c$	$\sqrt{7} \cdot l$

the peaks in the $g(r)$ are in exact correspondence to the distance reported in Tab. 5.1. We can not obtain information on high distance since the systems are at finite temperature and therefore phonons are present.

The second peak in the oxygen-oxygen $g(r)$ is relative to the diagonal of the square lattice that forms the ice nanotube. This gives us a confirmation

that the structure of the ice nanotube that we obtained is the one proposed by Koga *et al.* [25]. Moreover, the diagonal is exactly that of a square and since it coincides with our second peak in the $g(r)$ we have no distortion of the square lattice.

In Fig. 5.6 we reported oxygen-oxygen $g(r)$ for the other ice nanotube that present the non twisted structure. We do not report the exact calculation for the position all the peaks, but we provide a general way to easily calculate them.

With the index $\xi = \{a, b, c, \dots\}$ we identify the plane and with the index $i = 1, 2, \dots, N$ we identify the site of the ring with N atoms. The distance $\Delta_{\xi i}$ between the atom $(a, 1)$ and the atom (ξ, i) will be:

$$\Delta_{\xi i} = \sqrt{\Delta_{ai}^2 + \Delta_{\xi 1}^2} \quad (5.2)$$

where Δ_{ai} is the in-plane distance and $\Delta_{\xi 1}$ is the distance between the plane. As previously stated the distance between two adjacent plane is fixed to l and consequently $\Delta_{\xi 1}$ will be:

$$\Delta_{\xi 1} = m \cdot l. \quad (5.3)$$

The only things that we need to know for calculate each possible distance is the Δ_{ai} . The two distance $1a - 2a$ and $1a - Na$ are fixed to l and are the same for each geometry. The value of the in-plane distances for the geometry of the ice nanotubes considered in this work are reported in Tab. 5.2 .

Table 5.2: List of all the in-plane distance for the four type structure analyzed in this work.

Geometry	Δ_{ai}	Value
Square	$1a - 3a$	$\sqrt{2} \cdot l$
Pentagonal	$1a - 3a$ $1a - 4a$	$2 \sin\left(\frac{1}{5}\pi\right) \cdot l$
Hexagonal	$1a - 3a$ $1a - 5a$	$\sqrt{3} \cdot l$
Hexagonal	$1a - 4a$	$2 \cdot l$
Heptagonal	$1a - 3a$ $1a - 6a$	$2 \sin\left(\frac{1}{7}\pi\right) \cdot l$
Heptagonal	$1a - 4a$ $1a - 5a$	$\left[1 + 2 \sin\left(\frac{2}{7}\pi\right)\right] \cdot l$

5.3 Proton Ordering

We now concentrate on the position of the hydrogens in the lattice. Observing the behavior of the hydrogen-hydrogen radial distribution function for the

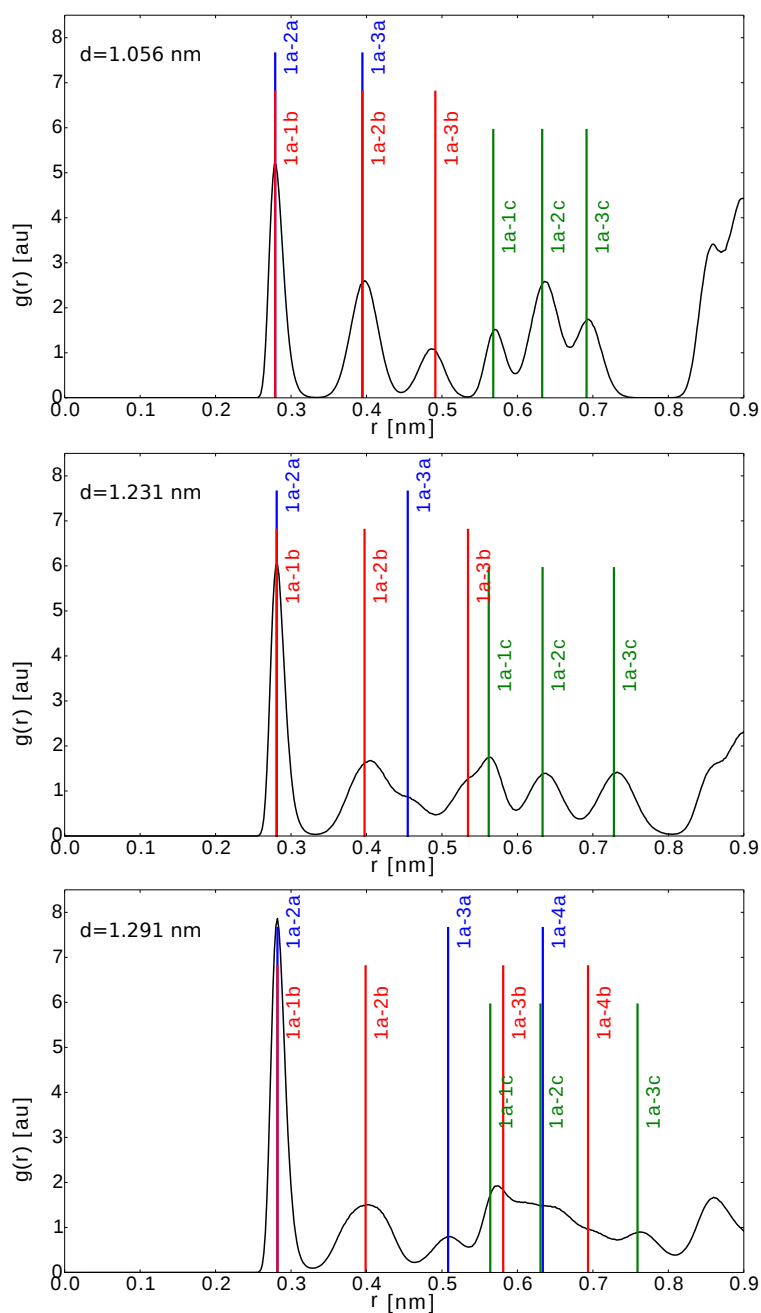


Figure 5.6: Comparison between oxygen-oxygen $g(r)$ at $T = 150$ K and the theoretical position of the peaks. The notation is the same of the Fig. 5.5, to improve readability we reported with different color the peak related to different plane.

lowest temperature showed in the Fig. 4.6, we notice that the second peak is placed in an anomalous position very near to the first one. This second peak was never observed in other form of ices and is a feature proper of this icy structures.

To understand where this peak comes from we compare in Fig. 5.7 the $g_{OO}(r)$ and the $g_{HH}(r)$ obtained at 150 K for the system with a diameter of the SWCNT $d = 1.291$ nm. In this figure we can clearly see that the second peak of the $g_{HH}(r)$ is in correspondence with the first peak of the $g_{OO}(r)$. This means that there is a significant number of hydrogens that are at the same relative distance of the two nearest neighbors oxygens. We can conclude that the hydrogens partially mimic the oxygen structure positioning at a relative distance that is the same of the typical for the oxygen 0.279 nm [89]. this means that there is a partial proton ordering so far never detected in literature.

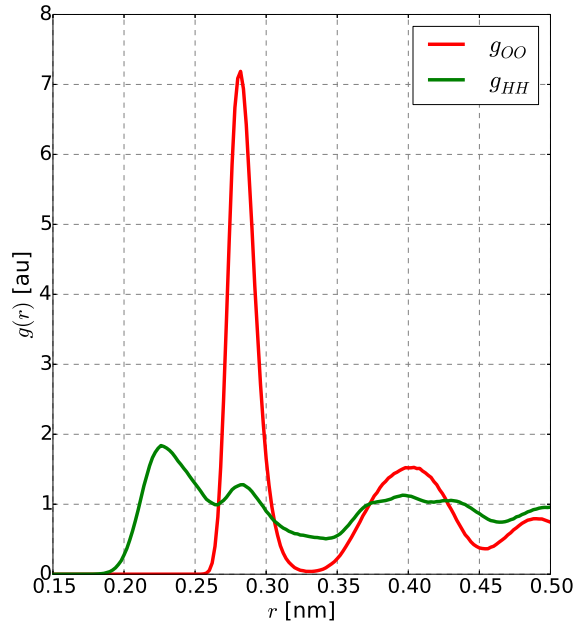


Figure 5.7: A blowup of the comparison of the $g_{OO}(r)$ and the $g_{HH}(r)$ relative to the SWCNT with diameter of 1.291 nm at 150 K. The second peak of the g_{hh} is situated in correspondence of the first peak of the g_{oo} . This is an evidence that there is a correlation between the relative position of the oxygen atoms and relative position of hydrogen atoms.

Finally, in the Fig. 5.8 we report the oxygen-oxygen, oxygen-hydrogen and hydrogen-hydrogen radial distribution functions for the lowest temperature investigated for all diameter sizes studied. In this figure we highlight

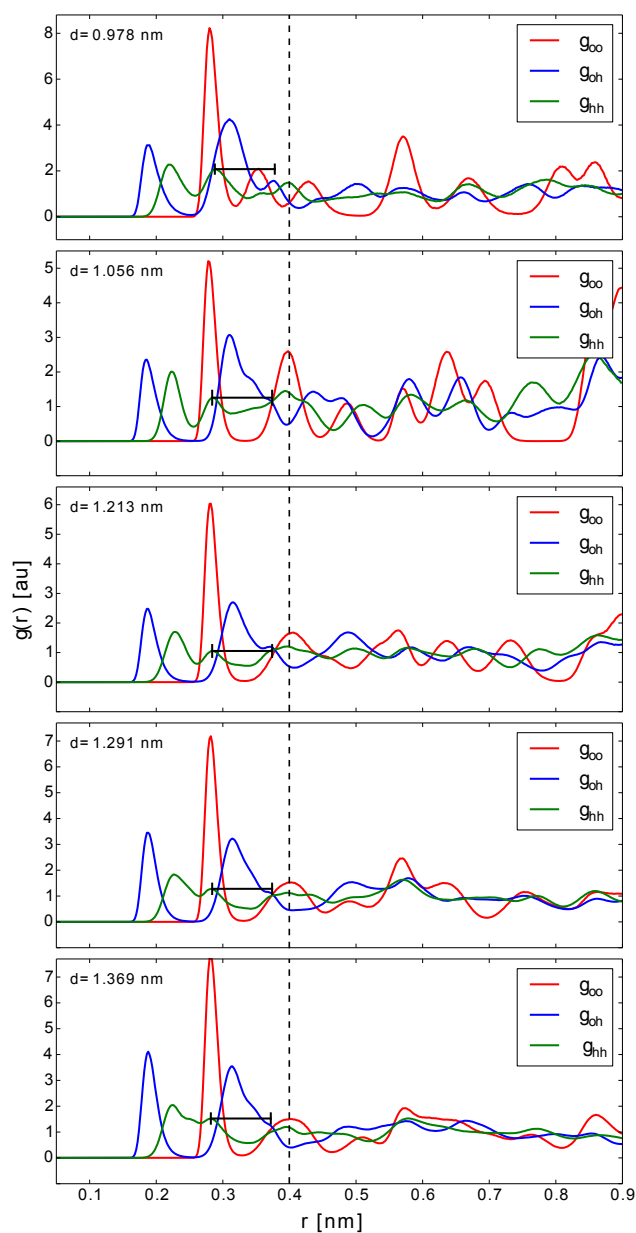


Figure 5.8: Radial distribution functions for all the nanotubes at the lowest temperature investigated ($T = 150$ K). Rows correspond to different diameters and columns, from the left, to oxygen-oxygen, oxygen-hydrogen and hydrogen-hydrogen $g(r)$. The vertical black dashed line marks the peak of the oxygen-oxygen $g(r)$ corresponding to the diagonal of the squares of the lattice. The horizontal black line represent the O-H distance in the TIP4P/ICE model.

with a black dashed line the position of the second peak of the $g_{OO}(r)$. As we previously discussed the second peak of the $g_{OO}(r)$ is relative to the diagonal of the square lattice. It is interesting to notice that the distance where the second peak is located is the same for the structure inside SWCNT with diameters larger than 1 nm. This means that all these ice nanotubes are ideally generated by the same square lattice. Differently, the ice formed in the smallest nanotube has a spiral structure, as previously discussed, leading to a split of the second peak. The first peak remains in the same position being the lattice parameter l not dependent from the nanotube sizes.

In the Fig. 5.8 we can also observe that the superposition between the first peak of the $g_{OO}(r)$ and the second peak of the $g_{HH}(r)$ is a feature common to all the systems investigated. We also note that the $g_{OH}(r)$ presents a shoulder in the position situated at distances around $l + \text{O-H}$, where O-H is the constant distance between oxygen and hydrogen within the water molecule in the TIP4P/ICE model. The O-H distances are reported as a black segment in the Fig. 5.8. The shoulder is therefore due to the extra alignment of the water molecules in the different layers of the ice structure and this strengthens our previous observation on proton ordering.

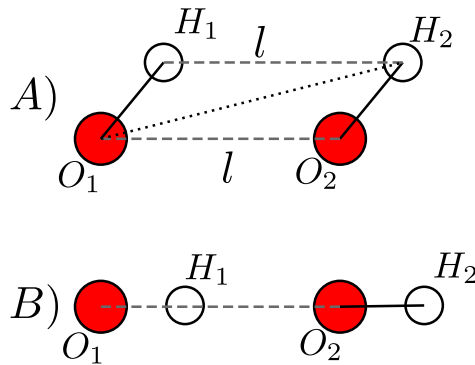


Figure 5.9: Proton ordering inside carbon nanotubes. The two configurations found in the simulations are reported in panel A) and B).

To better visualize the proton ordering structures that we found in our systems we report them in Fig.5.9. In the upper panel we report a general configuration in which the O-O distance is the same as the H-H distance while the intermolecular O-H distance depends on the angle. We know that there are a lot of molecules in which the H-H distance is the same as the O-O distance because of the clear second peak that we observe at that distance on the $g_{HH}(r)$, see Fig.5.7. These molecules are also visible in the snapshots, see Fig.5.3.

In the bottom panel we report the configuration that causes the previously

observed shoulder in the O-H distribution, see Fig.5.8, at distances $l+\text{O-H}$. The presence of a shoulder means that there is a significant number of water molecules aligned as shown in this second panel.

5.4 Conclusion

In this chapter we have studied in detail the structure that water forms inside the SWCNTs. This structure called “ice nanotubes” can be distinct in two different groups. In SWCNT with diameter higher than 1 nm the structures are characterized by a structure formed by rings of water molecules staked together forming the nanotube. The number of water molecules in each rings grow upon increasing the diameter of the SWCNT. The icy structure that forms inside the smallest SWCNT seems radically different. In the SWCNT of diameter $d = 0.978$ the “ice nanotube” look made by three twisted chain of water molecule. Following the idea proposed by Koga “et al.” to characterize the structures of the “ice nanotubes” we calculate the theoretical position of the peaks for the four bugger system comparing the results with our oxygen-oxygen radial distribution functions of the freed system. There is a remarkable agreement between the theoretical position of the peaks and the $g_{OO}(r)$ proving that this is the correct way to describe the “ice nanotubes”. Finally we face of the issue of the proton ordering. What arise from our $g_{OO}(r)$, $g_{OH}(r)$ and $g_{HH}(r)$ is that the hydrogen in this structures seems to mimic the position of the oxygen. These lead to the rise of a second peak in the hydrogen-hydrogen radial distribution function extremely close to the first one. This peak was never observed in other for of ice and is in correspondence of the firs peak of the $g_{OO}(r)$. This extremely interesting phenomena lead also to the arise of a shoulder in their g_{OH} do to an extra alignment of the water molecules. It is extremely important to remark that all this system are at finite temperature and therefor phonons are present.

Chapter 6

Ionic Solutions

In this chapter we want to present our work on the ionic aqueous solutions. In Sec. 6.1 we presented the potential used for these simulations and the technical details. The effects that different ions have on the structure of water are described in Sec. 6.2 where a review work is presented. In the last section Sec. 6.3 is discussed the relation between the issues of the hydration of the different ions and short range order.

6.1 Simulation Details

When we want to study the behavior of an ionic solution, we have to add in our model the ion-ion and water-ions interaction terms. A good model to study this kind of solution is the TIP4P water that we have introduced in Sec. 3.6 when we talk about TIP4P/ICE. We just recall now that in TIP4P the water molecule is represented by a four site rigid model with two hydrogen (H) sites with positive charge of $0.52e$. They are connected to the neutral oxygen (O) site, whose negative charge is attributed to a slightly shifted (0.015 nm) fourth site.

The oxygen sites interact with a Lennard-Jones potential, the other sites with the Coulomb forces. The ion-ion and the water sites-ions interactions were also modeled with the combination of the Coulombic 3.45 and the Lennard-Jones 3.4 potential. The Jensen and Jorgensen interaction parameters [91] were assumed for the LJ interaction of the ions. The ion-ion and the ion-water LJ parameters were calculated by using the geometrical mixing rules. Details about the values of the parameters can be found in the next section. These parameters were found to reproduce very well the structural characteristics and free energies of hydration of the ions.

The simulations were performed at constant ambient pressure ($p = 1$

atm) and different temperature with the use of appropriate thermostats. Periodic boundary conditions were applied. The interaction potentials were truncated at $0.9 \div 1.0$ nm. The long range electrostatic interactions were taken into account with the Ewald particle mesh method. The equilibration time was of 20 ns and the averages were calculated on production runs of 30 ns. The parallelized version of the GROMACS package has been used [92].

6.2 Modifications of The Water Structure

We show in Fig. 6.1 the radial distribution functions $g_{OO}(r)$ of the water oxygens in solution of NaCl(aq) and KCl(aq) at increasing concentrations at $T = 300$ K compared with the $g_{OO}(r)$ of pure water (TIP4P model). For the system with lower concentration the presence of ions does not perturb the short range order of liquid water. At intermediate concentration ($c = 1.36$ mol/kg) the first two shells are well defined. At the highest concentration instead there is evidence of a considerable change. In KCl(aq) the second OO shell is not well defined and in particular the first minimum almost disappears. In NaCl(aq) the second shell collapses on the first and all the OO structure appears quite different with respect to bulk water.

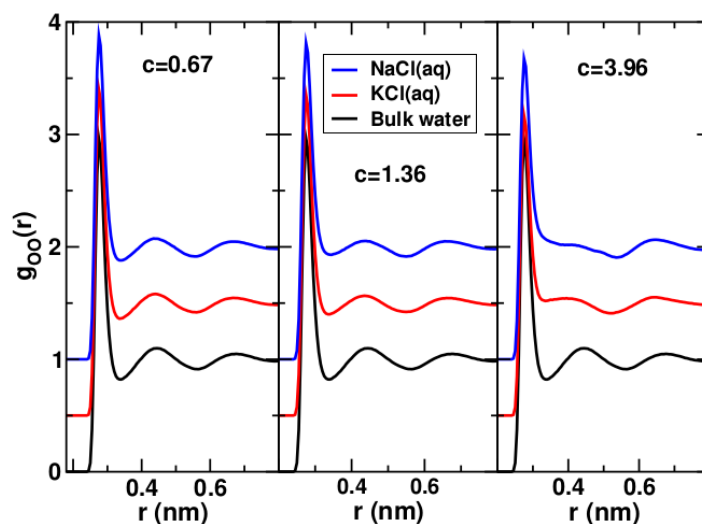


Figure 6.1: Oxygen-oxygen $g(r)$ of bulk water (unshifted) and for NaCl(aq) and KCl(aq) (vertically shifted) at $T = 300$ K at increasing concentrations (in mol/kg) as indicated. Data from Ref. [93]

We reported in Fig. 6.2 the $g_{OH}(r)$ of the solutions. We can observe that differently from the $g_{OO}(r)$ the $g_{OH}(r)$ do not present significant changes

with respect to bulk. These results indicate that at high concentration the HB network is still present but it is distorted by the interaction with the ions. This changes in the second shell of the $g_{OO}(r)$ with unbroken hydrogen bonds are similar to the effects of an high pressure on the liquid water [93].

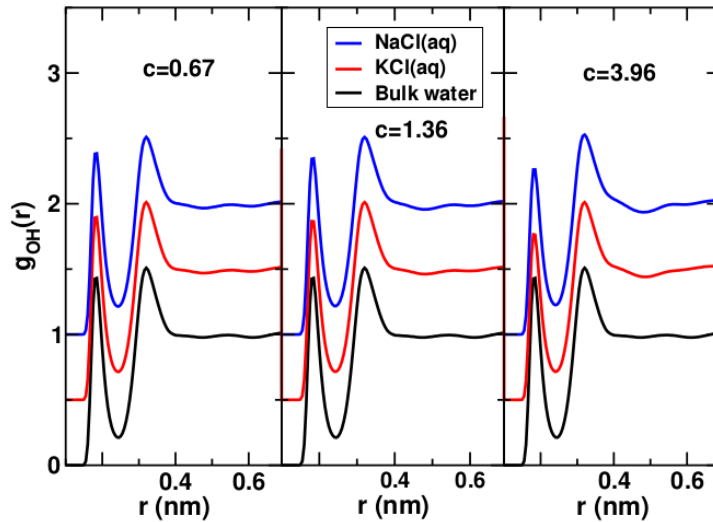


Figure 6.2: The $g_{OH}(r)$ of water in $\text{NaCl}(\text{aq})$ and $\text{KCl}(\text{aq})$ (vertically shifted) at $T = 300$ K at increasing concentrations (mol/kg) as indicated, the $g(r)$ are compared with bulk water (not shifted). Data from Ref. [93].

In Fig. 6.3 the supercooled regime at 220 K is reported. The peaks of the $g_{OO}(r)$ are more well defined for effect of the temperature and they are not changed by the ion interaction at low concentration. Instead at high concentration ($c = 3.96$ mol/kg), in particular for NaCl, the second shell is strongly distorted. The $g_{OH}(r)$ (not shown) are not modified by the presence of the ions with respect to the bulk.

The changes in the second peak of the $g_{OO}(r)$ in combination with the persistence of the HB order is the signature of an incipient HDL phase of water. From this point of view by assuming that the cations are dominating at high concentration, in spite of the different classification of K^+ as structure breaker and Na^+ as structure maker, both of them modify the O-O structure behind the first shell. This is in agreement with recent experiments [7]. We will discuss more this point below.

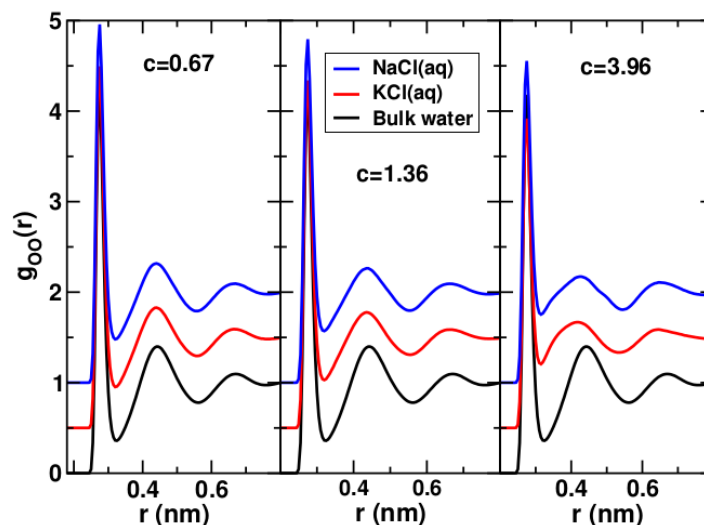


Figure 6.3: The $g_{OO}(r)$ of bulk water (unshifted) and for $\text{NaCl}(\text{aq})$ and $\text{KCl}(\text{aq})$ (vertically shifted) at $T = 220$ K at increasing concentrations (mol/kg) as indicated. Data from Ref. [93].

6.3 Hydration of Ions and Short Range Order

It is expected that the hydration of cations and anions have a strong effect on the solutions. In Fig. 6.4 we present the cation-oxygen and the anion-oxygen $g(r)$ in the case of $\text{NaCl}(\text{aq})$, $\text{KCl}(\text{aq})$ and $\text{KI}(\text{aq})$ at the concentration of 0.67 mol/kg at $T = 300$ K and $T = 220$ K. It is evident the formation of well defined shells of oxygens around the ions. The oxygen shells are closer to the cations as expected.

In $\text{KCl}(\text{aq})$ the potassium ions show a low hydration. The first K-O peak appears lower and the first minimum broader with respect to the first peak and the first minimum in $\text{KI}(\text{aq})$. The two shells of cations and anions in $\text{KCl}(\text{aq})$ are penetrating. The possibility of exchanging molecules between the first and the second shell are found in experiments [94] and also ab initio calculations on $\text{KCl}(\text{aq})$ [95]. The differences in the hydration shells of cations in $\text{KCl}(\text{aq})$ and $\text{KI}(\text{aq})$ indicate the interplay between charge and steric effects in the solutions. The role of cations and anions cannot simply be separated. The hydration of K^+ is enhanced in $\text{KI}(\text{aq})$ by the presence of I^- . Cations form more defined shells in $\text{KI}(\text{aq})$, where the I^- gives a steric contribution in keeping the charge ordering. In $\text{KI}(\text{aq})$, as in $\text{NaCl}(\text{aq})$ the anion-oxygen first peaks are exactly at the minimum of the cation-oxygen shells indicating a good charge ordering. Upon cooling similarities and differences between the solution properties are preserved. It is evident that the first shell of

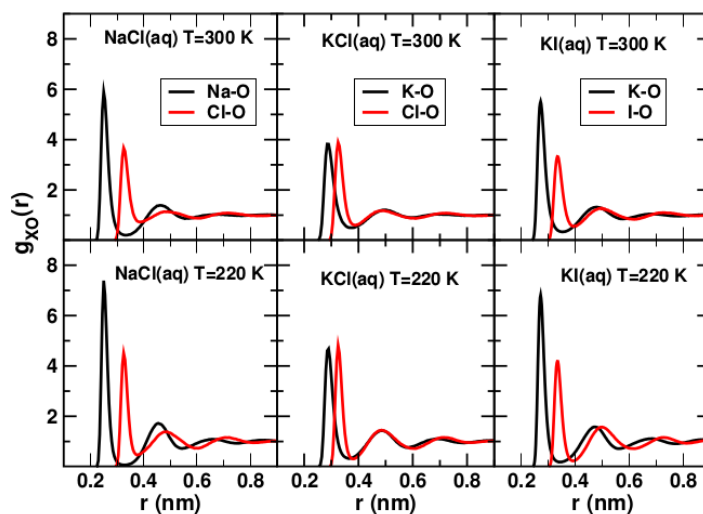


Figure 6.4: Cation-oxygen and anion-oxygen $g(r)$ for NaCl(aq) (left panels), KCl(aq) (central panels), KI(aq) (right panels) at concentration of $c = 0.67$ mol/kg and temperature $T = 300$ K (top) and $T = 220$ K (bottom). Data on NaCl(aq) and KCl(aq) from Ref. [93].

cation-oxygen $g(r)$ become even more rigid at $T = 220$ K both in NaCl(aq) and KI(aq) in comparison with the KCl(aq) . It is relevant to explore now more in details the effect on water. We show the three examples for NaCl(aq) , KCl(aq) and KI(aq) , that are representative of how the ions could be arranged in the water network. By considering Fig. 6.5 and Fig. 6.6 the first Na-O shell appears on the left of the O-O well separated from the Na-H shell. The Cl-O and Cl-H shells appear rigidly shifted with respect to the O-O shells. These results seem indicate that the Na^+ have the tendency to stay out from the HB network, while the Cl^- ions instead could be inserted in the network of water eventually substituting the oxygens. This is in agreement with recent computer simulation results on Na^+ and Cl^- inclusion in ice [96].

The $g_{\text{ClO}}(r)$ and the $g_{\text{ClH}}(r)$ are very similar in the three solutions, but in NaCl(aq) and KI(aq) the first peak is more rigid and well separated from the cation-oxygen first peak. In any case the $g_{\text{OO}}(r)$ is unchanged as already seen in Fig. 6.1. At the highest concentration instead we observe modifications of the $g_{\text{OO}}(r)$, as can be seen in Fig. 6.7, while the $g_{\text{OH}}(r)$, not shown, are very similar to the case $c = 0.67$ mol/kg. The O-O second shell in the three solutions though the effect is less pronounced in KCl(aq) . In NaCl(aq) the Na^+ ions present at least three well defined shells and it seems that they give the dominating effect. In KI(aq) the ions perturb the network

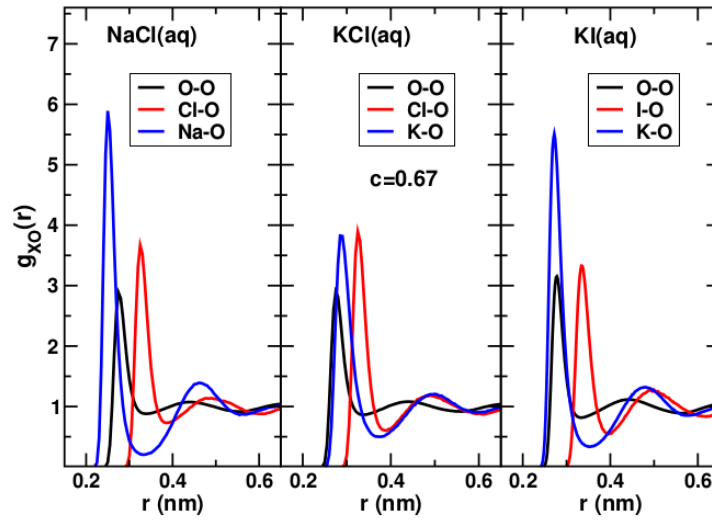


Figure 6.5: Oxygen-oxygen, anion-oxygen and cation-oxygen $g(r)$ at concentration of at $c = 0.67$ mol/kg and temperature $T = 300$ K for NaCl(aq) (left panel), KCl(aq) (central panel) and KI(aq) (right panel). Data on NaCl(aq) and KCl(aq) from Ref. [93].

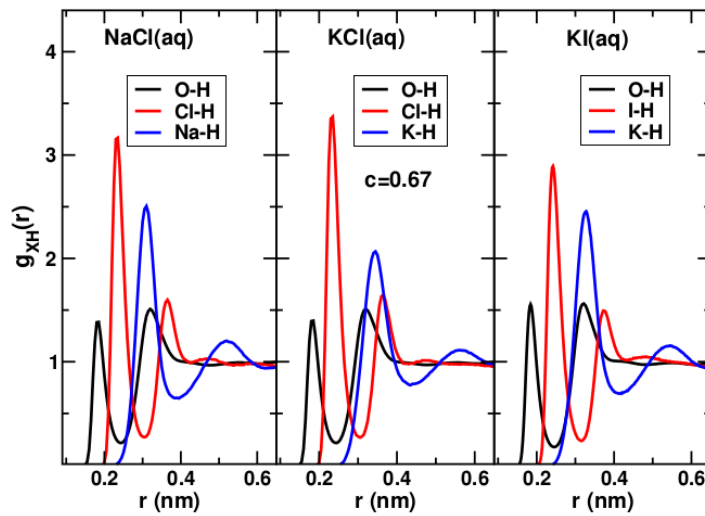


Figure 6.6: Oxygen-hydrogen, anion-hydrogen and cation-hydrogen $g(r)$ at concentration of at $c = 3.96$ mol/kg and temperature $T = 300$ K for NaCl(aq) (left panel), KCl(aq) (central panel) and KI(aq) (right panel). Data on NaCl(aq) and KCl(aq) from Ref. [93].

of water and the deformation of the O-O second shell is stronger than in KCl(aq) at the same concentration. It seems that water at this concentration

already at $T = 300$ K shows a prevalence of the HDL structure.

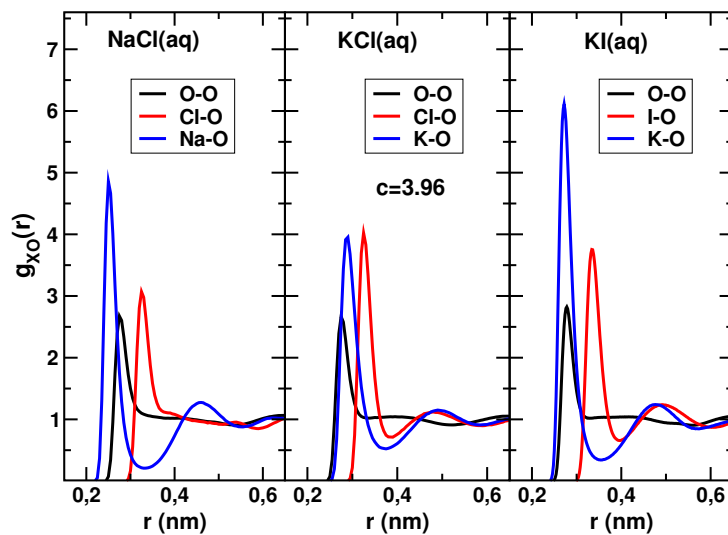


Figure 6.7: Oxygen-oxygen $g(r)$ of bulk water (unshifted) and for $\text{NaCl}(\text{aq})$ and $\text{KCl}(\text{aq})$ (vertically shifted) at $T = 300$ K at increasing concentrations (in mol/kg) as indicated. Data from Ref. [93].

Chapter 7

Confined Aqueous Solutions

We have seen in the previous chapter the effect that dilution of ions have on the structure of water. For this reason we choose to extend our study on water confined water in SWCNTs presented in the previous chapters including also aqueous solutions. We performed in parallel two study on different type of solution, one was about ionic solution of NaCl and the other is on the dilution of a neutral molecule that is CH₄. Our work on the ionic solution of NaCl inside SWCNT is reported in sections Sec. 7.1 and Sec. 7.2 that presents respectively the details of the simulation and the results. Simultaneously to the simulations on the ionic solution we perform a study on solution of water and methane in SWCNT. The details of the simulations are reported in Sec. 7.3 and the results are presented in Sec. 7.4 The results presented in this chapter are preliminary. More deeper study will be necessary in the future to have a complete picture.

7.1 NaCl Solutions: Simulation Setup

We performed the simulation of different systems of a solution of NaCl ions (Na⁺ Cl⁻) and TIP4P/ICE water inside SWCNT. The TIP4P/ICE model and SWCNT was described in the previous chapter (respectively Sec. 3.6 Sec. 4.1). As for the study illustrated in the previous chapter we choose for the ions the JJ parameters set. The interaction potential between particles is the sum of electrostatic 3.45 and LJ potential 3.4 as was described in the previous chapter. The ionic potential for this set of parameters was taken from Jensen and Jorgensen [91]. This potential was particularly tailored for use with the TIP4P model for solvent molecules. The ion-water parameters were obtained using geometric mixing rules

$$\sigma_{ij} = \sqrt{\sigma_{ii}\sigma_{jj}}, \quad (7.1)$$

$$\epsilon_{ij} = \sqrt{\epsilon_{ii}\epsilon_{jj}}, \quad (7.2)$$

The LJ parameters were obtained by Monte Carlo simulation with TIP4P water, reproducing the experimental free energies of hydration and the position of the first peak of the ion-oxygen radial distribution functions. In Tab. 7.1 was reported the value of the LJ parameters for all the possible combination of interacting atoms.

Table 7.1: Value of the LJ parameter for all the possible combination of atoms.

Atom pair	$\epsilon_{ij}[kJ/mol]$	$\sigma_{ij}[nm]$
Na-Na	0.00209	0.4070
Cl-Cl	2.97064	0.4020
O-O	0.88218	0.3167
C-C	0.29288	0.3550
H _{CNT} -H _{CNT}	0.12552	0.2420
Na-Cl	0.07879	0.4045
Na-O	0.02474	0.3590
Na-C	0.01620	0.3801
Na-H _{CNT}	0.01489	0.3353
Cl-O	1.61884	0.3568
Cl-C	0.93276	0.3778
Cl-H _{CNT}	0.61063	0.31190
O-C	0.50830	0.3353
O-H _{CNT}	0.33276	0.2768

We have studied the solution of water and Na Cl with two different concentrations, inside a SWCNT of diameter $d = 1.369$. We choose the bigger of the nanotube previously investigate because we are interested to possible inclusion of ions in the “ice nanotube”. In Tab. 7.2 we report the characteristics of the different systems that we have studied as the number of water molecules N_W , the number of carbon atoms N_C and the number of ions N_I , that is the sum of three number of Na and Cl atoms. The concentration c is express in mass fraction

$$c = \frac{m_I}{m_I + m_W} \quad (7.3)$$

where m_I is the mas of the ions

$$m_I = m_{Na} + m_{Cl} = 58.443 \text{ a.u.} \quad (7.4)$$

the mass is express in atomic units, in the same units

$$m_W = m_O + 2m_H = 14.011 \text{ a.u.} \quad (7.5)$$

In Tab. 7.2 is also reported the size of the initial simulation box. The axis of the cylinder was oriented in our simulation parallel to the y axis.

Table 7.2: Geometrical specifications of the different simulated systems. N_W is the number of water molecules contained in the simulation box, N_C is the number of carbon atoms that form the SWCNT, N_I Is the number of ions in the solution, this number count both Na and Cl . and x , y and z are the lengths of the simulation boxes for the highest temperature investigated.

C	N_W	N_C	N_I	x [nm]	y [nm]	z [nm]
2.13	3451	3240	18	2.018	23.282	2.018
3.97	3435	3240	34	2.096	23.438	2.096

We performed the simulations using the software GROMACS (version 5.0.7) [85], running the program on 8-core computer and on the INFN-Grid Roma Tre cluster¹.

The simulation box size was suited around the nanotube characteristics, as described in chapter 4, in order to have the smallest box that still allows the water molecules to surround the SWCNT. Periodic boundary conditions along all the three axes were applied in all simulations. An example of a simulation box is reported in Fig. 7.1 for the system with a diameter of $d = 1.369$ nm.

The range of temperature was decided in function on the result of the freezing temperature for pure water. We recall that for SWCNT of diameter $d = 1.369$ the freezing temperature for the water inside is $T_F = 250$ (see Tab. 4.3). The highest temperature investigated was $T_{max} = 300$ K and we have cooled the system to a temperature of $T_{min} = 200$ K. We choose to use a non uniform temperature step that start from a $\Delta T = 20$ when the system is far from the freezing point, to arrive to $\Delta T = 1$ when the temperature of the system is near to T_F . This choice was made in order to have the sensibility to observe a variation on T_F due to the concentration of salt. The variation in T_F for bulk solution id around 1 K.

We performed our simulations in the isothermal-isobaric ensemble (NpT), that was described in the previous chapter 3.1. For each diameter chosen for the SWCNT we started from a high temperature where water is liquid inside

¹<http://web-cluster.fis.uniroma3.it/>

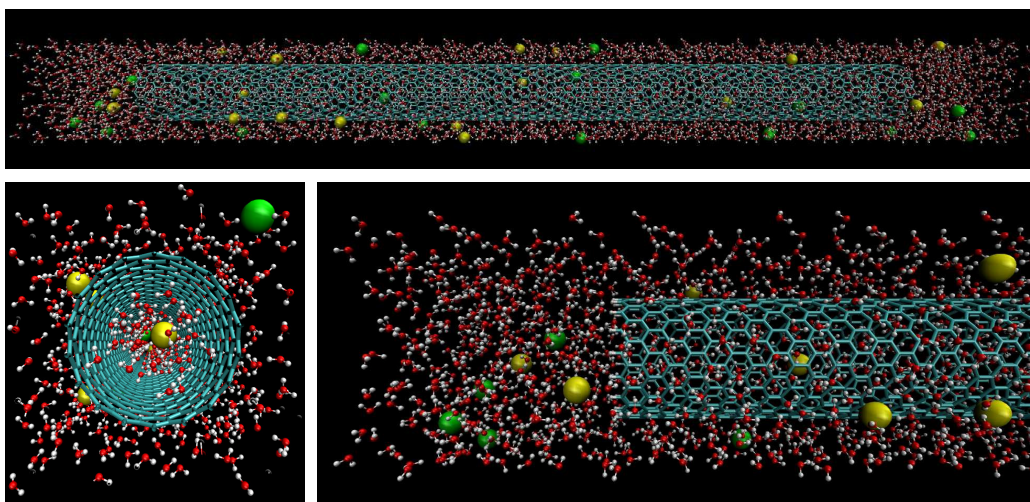


Figure 7.1: Snapshots of the system with a SWCNT of diameter $d = 1.369$ nm ($n = 18$) for the equilibrated sample at the highest temperature investigated, $T = 300$ K. The nanotube was filled and surrounded by a solution of TIP4P/ICE water and Na Cl with $c = 3.97$. The three snapshots represent respectively, the side view of the whole simulation box (top figure), a cut and blow up of the frontal view (bottom left figure) and a cut and blow up of the side view (bottom right figure).

the SWCNT. The time needed for the equilibration at low temperature is longer than the one for pure water. The length of the simulation was chosen also to avoid the quenching of the system,

We cooled each system along the $p = 1$ bar isobar. For each temperature we reach equilibrium using the Berendsen thermostat. For the pressure control we use the Parrinello-Rahman barostat, since it suited to study the crystal structure. The description of this thermostat and barostat can be found in the Sec. 3.2. Since the simulations of such a large system are rather time consuming, we used the shifted force method with a cutoff at 0.9 nm for all interactions. Particle-Mesh Ewald (see Sec. 3.5) was used to determine the long range forces in the systems.

The typical time required for the dipolar reorientation of water molecules inside SWCNT has been reported to be in the order of 0.7 picoseconds [86], for this reason we choose a time step of 0.001 ps for our simulations. The length of each simulation run was at least 5000 ps, in Tab. 7.3 was reported all the run time for different temperatures.

The total computational time amounts to about 105 ns for each of the isobar of the two systems and. The simulations were carried out on 8-core computer and on the INFN-Grid Roma Tre cluster² where we achieved an average simulation times that go from 7 ns/day for both the configuration.

Table 7.3: Report of the time for each system of TIP4P/ICE + NaCl investigated.

T [K]	$c = 1\%$	$c = 3.97\%$
	t_E [ps]	t_E [ps]
300	5000	5000
280	5000	5000
260	5000	5000
255	5000	5000
254	5000	5000
253	5000	5000
252	5000	5000
251	5000	5000
250	7000	7000
249	7000	7000
248	7000	7000
247	7000	7000
246	8000	8000
245	8000	8000
240	8000	8000
220	8000	8000
200	8000	8000

7.2 NaCl Solutions: Results

The idea behind this study is that we want to observe if there is any inclusion of the ions in the “ice nanotube” structure that was described in the previous chapter. The results of our simulation however show that there is no inclusion of the ions in the “ice nanotube” structure for both the concentration investigated. This is probably due to the extreme stability of the structure of that form of ice. We observed in the previous chapters 4 and 5 that this structure was extremely robust in the changing of the potential of water. The same structure was observed for TIP4P SPC/E and now for TIP4P/ICE. We reported for a visual inspection two snapshots for each of the concentration studied Fig. 7.2 and Fig. 7.2 . From that figure it is possible to note that the “ice nanotube” will form inside the SWCNT“ ejecting the ions outside.

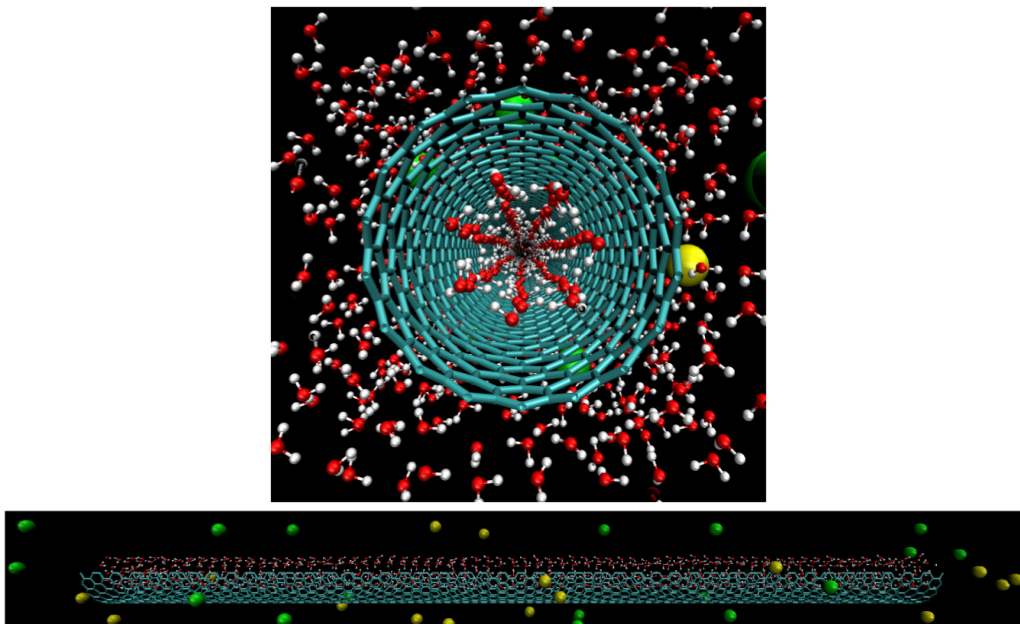


Figure 7.2: Snapshots of the system made by with a SWCNT of diameter $d = 1.369$ nm and a solution of TIP4P/ICE water and NaCl with concentration $c = 2.13$ for the lowest temperature investigated $T = 200$ K. The yellow and the green spheres are respectively Na and the Cl ions. In the top panel is presented a frontal view of the system. In the bottom panel is reported a lateral view of the system with the upper part of the SWCN hid to show the inner part. The external water was removed from this figure for better visualize the structure of ice nanotube.

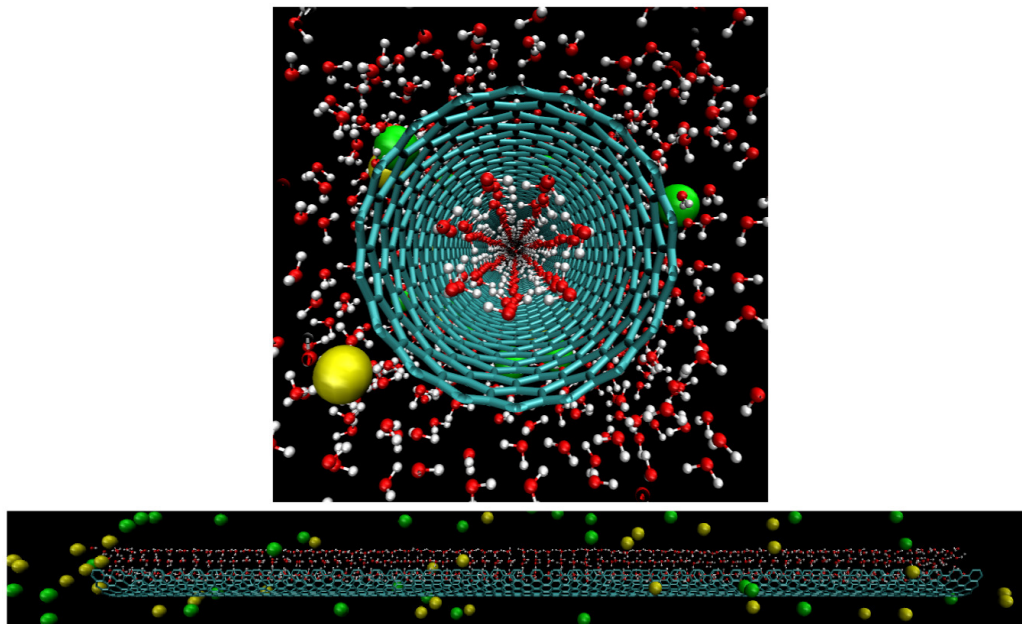


Figure 7.3: Snapshots of the system made by with a SWCNT of diameter $d = 1.369$ nm and a solution of TIP4P/ICE water and NaCl with concentration $c = 3.97$ for the lowest temperature investigated $T = 200$ K. The yellow and the green spheres are respectively Na and the Cl ions. In the top panel is presented a frontal view of the system. In the bottom panel is reported a lateral view of the system with the upper part of the SWCN hid to show the inner part. The external water was removed from this figure for better visualize the structure of ice nanotube.

7.3 Methane Solutions: Simulation Setup

In parallel with the study on the ions solutions, we start a work on the solution of CH_4 and TIP4P/ICE water inside SWCNTs. The focus of this study is investigate the possibility of the formation of hydrate in confined water. Therefore we performed the MD simulation of different system with different concentration of CH_4 and water. The model that describe TIP4P/ICE and SWCNT was described in the previous chapter (respectively Sec. 3.6 Sec. 4.1). Although methane is a non spherical molecule, it may be described reasonably well by using a spherical LJ interaction site. In our simulations we used the parameters proposed by Guillot and Guissani [?] and Paschek. [?] TraPPE Ref. [?] and OPLS-UA Ref. [?] are other popular models for methane.

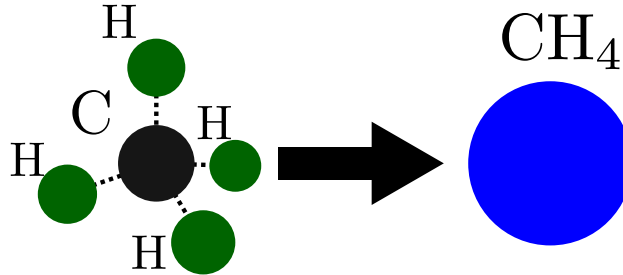


Figure 7.4: On the left there is a realistic picture of the methane. On the right there is a schematic representation of the one site model used to describe the methane molecule.

We report the potential parameters that we have used for this simulation in Tab. 7.4 . The cross-interaction parameters are calculated with the Lorentz-Berthelot mixing rules.

$$\sigma_{ij} = \frac{\sigma_{ii} + \sigma_{jj}}{2}, \quad (7.6)$$

$$\epsilon_{ij} = \sqrt{\epsilon_{ii}\epsilon_{jj}}, \quad (7.7)$$

We have studied the solution of water and CH_4 inside a SWCNT of two different diameter $d = 1.369$ nm and $d = 1.291$ nm. We choose the two bigger nanotubes previously investigate in order to have the enough space for the formation of hydrates. In Tab. 7.5 we report the characteristics of the different systems that we have studied as the number of water molecules N_W ,the number of carbon atoms N_C and the number of methane N_M . The concentration c is express in mass fraction

$$c = \frac{m_M}{m_M + m_W} \quad (7.8)$$

Table 7.4: Value of the LJ parameter for all the possible combination of atoms.

Atom pair	$\epsilon_{ij}[kJ/mol]$	$\sigma_{ij}[nm]$
CH ₄ -CH ₄	1.22640	0.3730
O-O	0.88218	0.3167
C-C	0.29288	0.3550
H _{CNT} -H _{CNT}	0.12552	0.2420
CH ₄ -O	1.04015	0.3448
CH ₄ -C	0.01620	0.3640
CH ₄ -H _{CNT}	0.39235	0.3075
O-C	0.59932	0.3353
O-H _{CNT}	0.33276	0.2768

where m_M is the mas of the methane molecule

$$m_M = m_C + 4 \cdot m_H = 16.043 \text{ a.u.} \quad (7.9)$$

the mass is express in atomic units, in the same units

$$m_W = m_O + 2m_H = 14.011 \text{ a.u.} \quad (7.10)$$

In Tab. 7.2 is also reported the size of the initial simulation box. The axis of the cylinder was oriented in our simulation parallel to the y axis.

Table 7.5: Geometrical specifications of the different simulated systems. c is the concentration express in max fraction. N_W is the number of water molecules contained in the simulation box, N_C is the number of carbon atoms that form the SWCNT, N_M Is the number of methane in the solution, and x , y and z are the lengths of the simulation boxes for the highest temperature investigated.

d [nm]	c	N_W	N_C	N_M	x [nm]	y [nm]	z [nm]
1.291	2.02	3156	3060	57	2.018	23.282	2.018
1.369	2.01	3408	3240	61	2.096	23.438	2.096

We performed the simulations using the software GROMACS (version 5.0.7) [85], running the program on 8-core computer and on the INFN-Grid Roma Tre cluster².

²<http://web-cluster.fis.uniroma3.it/>

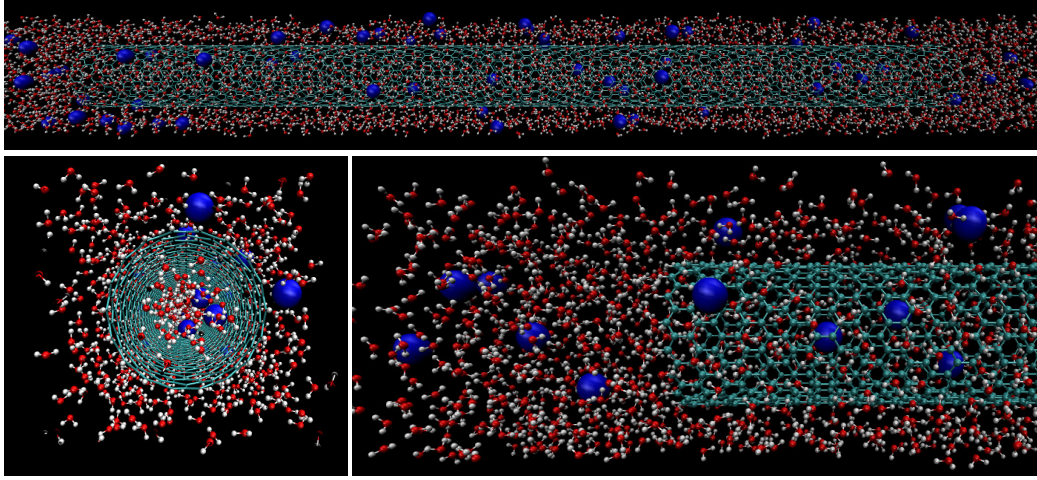


Figure 7.5: Snapshots of the system with a SWCNT of diameter $d = 1.369 \text{ nm}$ ($n = 18$) for the equilibrated sample at the highest temperature investigated, $T = 300\text{K}$. The nanotube was filled and surrounded by a solution of TIP4P/ICE water and CH_4 with $c = 2.01$. The three snapshots represent respectively, the side view of the whole simulation box (top figure), a cut and blow up of the frontal view (bottom left figure) and a cut and blow up of the side view (bottom right figure).

The simulation box size was suited around the nanotube characteristics, as described in chapter 4, in order to have the smallest box that still allows the water molecules to surround the SWCNT. Periodic boundary conditions along all the three axes were applied in all simulations. An example of a simulation box is reported in Fig. 7.5 for the system with a diameter of $d = 1.369 \text{ nm}$.

The range of temperature was decided in function on the result of the freezing temperature for pure water. We recall the freezing temperature for the water inside the two SWCNTs investigated in this part of the work:

$$d = 1.291\text{nm}; \quad T_F = 310\text{K}$$

$$d = 1.369\text{nm}; \quad T_F = 250\text{K}$$

The highest and the lowest temperatures investigate was different for the two system, but the choice of of the temperature step ΔT was the same.

$$\Delta T = 10\text{K}$$

We performed our simulations in the isothermal-isobaric ensemble (NpT), that was described in the previous chapter 3.1. For each diameter chosen for the SWCNT we started from a high temperature where water is liquid inside

the SWCNT. The time needed for the equilibration at low temperature is longer than the one for pure water.

We cooled each system along the $p = 1$ bar isobar. For each temperature we reach equilibrium using the Berendsen thermostat. For the pressure control we use the Parrinello-Rahman barostat, since it suited to study the crystal structure.. The description of this thermostat and barostat can be found in the Sec. 3.2 . Since the simulations of such a large system are rather time consuming, we used the shifted force method with a cutoff at 0.9 nm for all interactions. Particle-Mesh Ewald (PME)(see Sec. 3.5) was used to determine the long range forces in the systems.

The typical time required for the dipolar reorientation of water molecules inside SWCNT has been reported to be in the order of 0.7 picoseconds [86], for this reason we choose a time step of 0.001 ps for our simulations. The length of each simulation run was at least 10000 ps, in Tab. 7.6 was reported all the run time for different temperatures.

Table 7.6: Report of the time simulated for each system of TIP4P/ICE + CH₄ investigated.

$d = 1.291$ nm		$d = 1.369$ nm	
T [K]	t_E [ps]	T [K]	t_E [ps]
350	10000	300	10000
340	10000	290	10000
330	10000	280	10000
320	10000	270	10000
310	10000	260	10000
300	10000	250	10000
290	10000	240	10000
280	10000	230	10000
270	10000	220	10000
260	10000	210	10000
250	10000	200	10000

The total computational time amounts to about 100 ns for each of the isobar of the two systems and. The simulations were carried out on 8-core computer and on the INFN-Grid Roma Tre cluster² where we achieved an average simulation times that go from 8 ns/day for both the configuration.

7.4 Methane Solutions: Results

The idea behind this study is that we want to investigate the possibility of hydrates formation in confined water. The results of our simulations however shows that, as has happened in the case of the NaCl showed in the previous sections, the "ice nanotube" will form, ejecting the methane. This is another hint on the extreme stability of that kind of structure. We reported for a visual inspection two snapshots for each of the diameter studied Fig. 7.6 and Fig. 7.7 . From that figure it is possible to note that the "ice nanotube" will form inside the SWCNT" ejecting the methane outside.

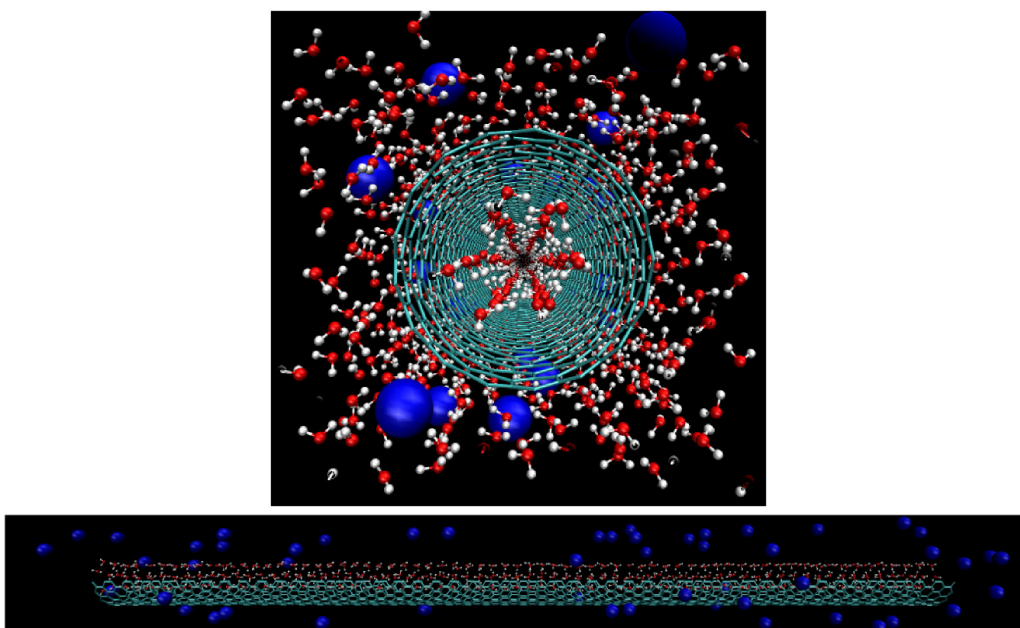


Figure 7.6: Snapshots of the system made by with a SWCNT of diameter $d = 1.291$ nm and a solution of TIP4P/ICE water and CH_4 with concentration $c = 2.02$ for the lowest temperature investigated $T = 200$ K. The blue spheres are the methane molecules. In the top panel is presented a frontal view of the system. In the bottom panel is reported a lateral view of the system with the upper part of the SWCN hided to show the inner part. The external water was removed from this figure for better visualize the structure of ice nanotube.

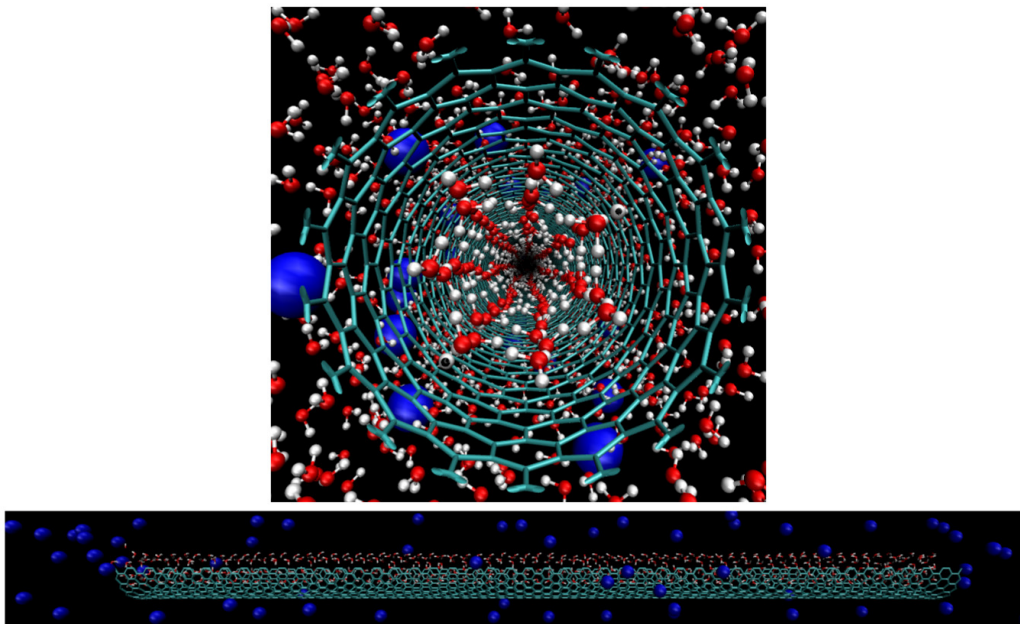


Figure 7.7: Snapshots of the system made by with a SWCNT of diameter $d = 1.369$ nm and a solution of TIP4P/ICE water and CH_4 with concentration $c = 2.01$ for the lowest temperature investigated $T = 250$ K. The blue spheres are the methane molecules. In the top panel is presented a frontal view of the system. In the bottom panel is reported a lateral view of the system with the upper part of the SWCNT hidid to show the inner part. The external water was removed from this figure for better visualize the structure of ice nanotube.

7.5 Conclusion

As we stated in the introduction of this chapter the result presented in this chapter are preliminary. In our simulations on aqueous solutions we have observed that the solute was ejected with the formation of the ice nanotube. This happen regardless to the nature of the of the solute: Na^+ and Cl^- are charged particles that interact also via LJ potential, instead CH_4 is represented as a single chargeless particle that have only the LJ interaction. The fact that all the solute particles are ejected is another hint on the extreme stability of that kind of structure. We observed previously that this structure was extremely robust in the changing of the potential of water. The same structure was observed for TIP4P SPC/E and now for TIP4P/ICE. The perturbation induce by the solute atoms are not enough to alter the structure. To improve this studies on the solution the are several possibility. The simple variation that can lead to different results is increase the concentrations of the solutions. Another possibility is try with different models, in particular for the CH_4 where it is possible to implement a more detailed representation of the solute molecule. We have studied system cooled among an isobar at ambient pressure (1 atm) can be interesting increase the pressure. The high pressure study needs however a similar studies for pure water to make a comparison.

Chapter 8

Conclusions and Future Outlooks

The goal of this PhD thesis is the study, through MD simulations, of the behavior of pure water and aqueous solutions inside SWCNTs upon cooling. This work can be conceptualized in two parts: the first in which it is studied the liquid solid transition of pure water inside SWCNTs of five different diameters and a second in which we focused on the behavior of NaCl or CH₄ aqueous solutions inside SWCNTs. To describe the water molecules at best we choose one of the potentials that better reproduces the freezing processes in bulk water: the TIP4P/ICE [28].

The first issue that we faced was the location of the freezing temperatures T_F of pure water for the different sizes of nanotubes investigated. In order to identify the temperature at which water freezes we analyzed the behavior of the potential energy. We identify T_F , as the temperature where the potential energy shows an abrupt decrease. To support this analysis we observed also the behavior of the water radial distribution function $g_{ij}(r)$. The $g_{ij}(r)$ show an abrupt change in correspondence of the freezing temperature predicted with the potential energy behavior. Among the five different pores that we have investigated we observed a maximum value of $T_F = 310$ K for the SWCNT of diameter $d = 1.056$ nm.

Importantly, with the potential model that we used, we obtained freezing temperatures in very good agreement with a recent experiment [26] that discovered for the first time that in these nanotubes water freezes when it boils in the bulk, namely at $T = 310$ K. This remarkable effect is much more consistent than what was expected. We recall here that for this potential, TIP4P/ICE, in the bulk phase the freezing point coincides with the freezing point of experimental water.

Among the different nanotubes that we simulated the ordered structures that we find below T_F are different. In particular we observed that for the SWCNT with diameter $d = 0.978$ nm the water molecules form three chains

wrapped together to form a spiral.

In the first part of Chapter 5 we have described the ordering processes of the water molecules upon cooling. What arise from this studies is that when the temperature drops below T_F for all the nanotubes with diameter larger than 1 nm the water molecules form an ordered stack of rings. When the size of the nanotube grows the water rings became larger passing from rings formed by 4 molecules up to those formed by 7 molecules. These structures are in agreement with those found on this kind of SWCNT using different model potentials for water [24, 25]. This proves that the results on the structure of the ice nanotubes are very robust.

In order to deepen and extend our knowledge of the ice nanotubes structure we have made an analysis of the oxygen-oxygen radial distribution function for the systems that shows a structures made by staked rings. With this analysis we were able to assign the peaks in the $g_{OO}(r)$ to the distance between atoms in the structures and observe the common features of the different structures obtained in the different pores. The result was that the peaks of the $g_{OO}(r)$ are in extremely good agreement with the theoretical structures.

As a novel result, we have found the presence of a partial proton ordering in the ice nanotube at finite temperature. This is an extremely interesting result since the proton ordering is relevant issue in the physics of ice [?]. The ordering effect is due to the fact that in the ice nanotubes the hydrogens mirror the structure of the oxygens. This produces an anomalous peak in the $g_{HH}(r)$ adjacent to the first one, and also a shoulder in the $g_{OH}(r)$.

In our analysis of the computer simulations results on the structure of non confined ionic aqueous solutions We focused on the result for NaCl making a comparison with the results on the potassium halides KCl, KI that have anions of different sizes. This analysis confirms that the traditional classification of ions as structure making/breaking dose not give a complete prediction of the way in which water structure changes under the effect of ions. On the other hand, taking into account that the ions could perturb water beyond the first shell it is of relevant interest to understand the role of the different ions in the study of ionic solutions.

As for the results of the simulations of the aqueous solution of NaCl ions confined in SWCNT, the goal of this study was the simulations of a possible inclusion of the ions in the “ice nanotube” structure. We chose the Jensen and Jorgensen parameters that were found to reproduce very well the structural characteristics and free energies of hydration of the ions. We studied different systems that are made by two different concentration of ions that fill a SWCNT with diameter $d = 1.369$ nm that is the largest nanotube investigate in the first part of this work. What we observed was that there

is no inclusion of the ions in the ice structures. This happened for both the concentration investigated. We will discuss our conclusions on this argument here below together with the ones relative the methane.

The idea behind the study of the solution of CH_4 was that we wanted to investigate the possibility of hydrates formation in confined water. We chose to describe methane with a total atomic potential. In this scenario the methane is only spherical Lennard-Jones interaction site. We simulated two different SWCNTs with diameter $d = 1.369$ nm and $d = 1.291$ nm and filled with a solution of CH_4 with concentration $c \approx 2$ (expressed in mass fractions). The results of our simulations were similar to the ones obtained for the solution with ions, the "ice nanotube" forms, ejecting the methane.

In our simulations on aqueous solutions we have observed, in both systems, that the solute was ejected with the formation of the ice nanotube. This happen regardless to the nature of the of the solute: Na^+ and Cl^- are charged particles that interact also via Lennard-Jones potential, instead CH_4 is represented as a single chargeless particle that has only the Lennard-Jones interaction. The fact that all the solute particles are ejected is another hint on the extreme stability of the "ice nanotube". We observed previously that this structure was extremely robust in the changing of the potential of water. The same structure was in fact observed for TIP4P, SPC/E and now for TIP4P/ICE. The perturbation induced by the solute atoms, in the solutions investigated so far, are not enough to alter the structure of the "ice nanotubes".

Future Outlooks

As for the study the pure water inside SWCNTs is concerned, there are several possibilities to develop our knowledge of the liquid-solid transition. We have simulated systems with five different diameters d of the SWCNT. The increase of the number of diameters could give us a better picture of the phase diagram in the $T - d$ plane. Another possibility is to perform simulations on the dynamics of the water molecule upon cooling to support what we found so far using structural and thermodynamical properties. This type of analysis can be useful in particular to investigate what happens at low values of the SWCNT diameter.

For our study on the confined solutions the possibility to improve our results are several. We have observed that all the solute atoms are ejected from the ice structure, a different result can be achieved increasing the concentration of the solutions. Different models for the ions can also lead to a different result in particular for the case of CH_4 where a more detailed representation of the solute molecule can be necessary. Another interesting future

study can be done by increasing the pressure. All our studies were in fact performed at ambient pressure and in particular for the hydrates formation this can be a modification that leads to interesting results.

More experiment on this type of systems would be helpful to have a clear picture of the physics. This is true both for the system with pure water and system with aqueous solution. In particular in this last case experiments could be useful for an improvement of the parameterization of the interaction between ions or methane with carbon nanotubes.

Appendix A

List of Activities

List of publications relative to the results presented in this Thesis

- P. Pugliese, M. Martin Conde, M. Rovere and P. Gallo. *Freezing Temperatures, Ice Nanotubes Structures and Proton Ordering of TIP4P/ICE Water Inside Single Wall Carbon Nanotubes*. Accepted by The Journal of Physical Chemistry B (2017).
- P. Gallo, M. Martin Conde, D. Corradini, P. Pugliese and M. Rovere. *Structural properties of ionic aqueous solutions*. In Many-body approaches at different scales: A tribute to Norman H. March on the occasion of his 90th birthday", G. G. N. Angilella and C. Amovilli, editors (New York, Springer, 2017 - to be published).

List of School and Conference

- **Roma Tre Workshop on Water Under Extreme Condition.**
Rome. 10-12 June 2015.
Member of the Local Organizing Committee.
- **CCP5 Summer School 2015 Methods in Molecular Simulations.**
Manchester, 12- 21 July 2015.
- **Water and Water Systems.**
Erice (Italy) 22-31 July 2016.
Poster Presented.

- **Roma Tre Workshop on Water Under Extreme Condition.**
Rome. 14-16 June 2017.
Member of the Local Organizing Committee and Poster Presented.
- **8th International Discussion Meeting on Relaxations in Complex Systems.**
Wisla (Poland) July 23-28 2017.
Poster Presented

Bibliography

- [1] P. Gallo, K. Amann-Winkel, C. A. Angell, M. A. Anisimov, F. Caupin, C. Chakravarty, E. Lascaris, T. Loerting, A. Z. Panagiotopoulos, J. Russo, J. A. Sellberg, H. E. Stanley, H. Tanaka, C. Vega, L. Xu, and L. G. M. Pettersson, “Water: A Tale of Two Liquids,” *Chemical Reviews*, vol. 116, no. 13, pp. 7463–7500, 2016. PMID: 27380438.
- [2] F. Franks and R. S. o. C. G. Britain), *Water: A Matrix of Life*. RSC paperbacks, Royal Society of Chemistry, 2000.
- [3] P. G. Debenedetti, *Metastable liquids: concepts and principles*. Princeton University Press, 1996.
- [4] P. G. Debenedetti, “Supercooled and glassy water,” *Journal of Physics: Condensed Matter*, vol. 15, no. 45, p. R1669, 2003.
- [5] A. Rahman and F. H. Stillinger, “Molecular Dynamics Study of Liquid Water,” *The Journal of Chemical Physics*, vol. 55, no. 7, pp. 3336–3359, 1971.
- [6] L. Liu, S.-H. Chen, A. Faraone, C.-W. Yen, and C.-Y. Mou, “Pressure Dependence of Fragile-to-Strong Transition and a Possible Second Critical Point in Supercooled Confined Water,” *Phys. Rev. Lett.*, vol. 95, p. 117802, Sep 2005.
- [7] P. Gallo, M. Rovere, and S.-H. Chen, “Dynamic Crossover in Supercooled Confined Water: Understanding Bulk Properties through Confinement,” *The Journal of Physical Chemistry Letters*, vol. 1, no. 4, pp. 729–733, 2010.
- [8] J. C. Rasaiah, S. Garde, and G. Hummer, “Water in Nonpolar Confinement: From Nanotubes to Proteins and Beyond,” *Annual Review of Physical Chemistry*, vol. 59, no. 1, pp. 713–740, 2008. PMID: 18092942.

- [9] M. F. L. De Volder, S. H. Tawfick, R. H. Baughman, and A. J. Hart, “Carbon Nanotubes: Present and Future Commercial Applications,” *Science*, vol. 339, no. 6119, pp. 535–539, 2013.
- [10] C. Hierold, A. Jungen, C. Stampfer, and T. Helbling, “Nano electromechanical sensors based on carbon nanotubes,” *Sensors and Actuators A: Physical*, vol. 136, no. 1, pp. 51–61, 2007. 25th Anniversary of Sensors and Actuators A: Physical.
- [11] Z. Liu, S. Tabakman, K. Welsher, and H. Dai, “Carbon nanotubes in biology and medicine: In vitro and in vivo detection, imaging and drug delivery,” *Nano Research*, vol. 2, no. 2, pp. 85–120, 2009.
- [12] Zanello Laura P., Zhao Bin, Hu Hui, and Haddon Robert C., “Bone Cell Proliferation on Carbon Nanotubes,” *Nano Letters*, vol. 6, no. 3, pp. 562–567, 2006.
- [13] J. R. Bordin and M. C. Barbosa, “Flow and structure of fluids in functionalized nanopores,” *Physica A: Statistical Mechanics and its Applications*, vol. 467, pp. 137–147, 2017.
- [14] J. A. Thomas and A. J. H. McGaughey, “Water Flow in Carbon Nanotubes: Transition to Subcontinuum Transport,” *Phys. Rev. Lett.*, vol. 102, p. 184502, May 2009.
- [15] Majumder Mainak, Chopra Nitin, Andrews Rodney, and Hinds Bruce J., “Nanoscale hydrodynamics: Enhanced flow in carbon nanotubes,” *Nature*, vol. 438, pp. 44–44, nov 2005. 10.1038/43844a.
- [16] D. Cohen-Tanugi and J. C. Grossman, “Water Desalination across Nanoporous Graphene,” *Nano Letters*, vol. 12, no. 7, pp. 3602–3608, 2012. PMID: 22668008.
- [17] B. Corry, “Designing Carbon Nanotube Membranes for Efficient Water Desalination,” *The Journal of Physical Chemistry B*, vol. 112, no. 5, pp. 1427–1434, 2008. PMID: 18163610.
- [18] Y. Maniwa, H. Kataura, M. Abe, S. Suzuki, Y. Achiba, H. Kira, and K. Matsuda, “Phase Transition in Confined Water Inside Carbon Nanotubes,” *Journal of the Physical Society of Japan*, vol. 71, no. 12, pp. 2863–2866, 2002.
- [19] Y. Maniwa, H. Kataura, M. Abe, A. Udaka, S. Suzuki, Y. Achiba, H. Kira, K. Matsuda, H. Kadowaki, and Y. Okabe, “Ordered water inside

- carbon nanotubes: formation of pentagonal to octagonal ice-nanotubes,” *Chemical Physics Letters*, vol. 401, no. 4–6, pp. 534–538, 2005.
- [20] S. Ghosh, K. V. Ramanathan, and A. K. Sood, “Water at nanoscale confined in single-walled carbon nanotubes studied by NMR,” *EPL (Europhysics Letters)*, vol. 65, no. 5, p. 678, 2004.
- [21] A. I. Kolesnikov, J.-M. Zanotti, C.-K. Loong, P. Thiyagarajan, A. P. Moravsky, R. O. Loutfy, and C. J. Burnham, “Anomalously Soft Dynamics of Water in a Nanotube: A Revelation of Nanoscale Confinement,” *Phys. Rev. Lett.*, vol. 93, p. 035503, Jul 2004.
- [22] O. Byl, J.-C. Liu, Y. Wang, W.-L. Yim, J. K. Johnson, and J. T. Yates, “Unusual Hydrogen Bonding in Water-Filled Carbon Nanotubes,” *Journal of the American Chemical Society*, vol. 128, no. 37, pp. 12090–12097, 2006. PMID: 16967958.
- [23] D. Takaiwa, I. Hatano, K. Koga, and H. Tanaka, “Phase diagram of water in carbon nanotubes,” *Proceedings of the National Academy of Sciences*, vol. 105, no. 1, pp. 39–43, 2008.
- [24] J. Shiomi, T. Kimura, and S. Maruyama, “Molecular Dynamics of Ice-Nanotube Formation Inside Carbon Nanotubes,” *The Journal of Physical Chemistry C*, vol. 111, no. 33, pp. 12188–12193, 2007.
- [25] K. Koga, R. D. Parra, H. Tanaka, and X. C. Zeng, “Ice nanotube: What does the unit cell look like?,” *The Journal of Chemical Physics*, vol. 113, no. 12, pp. 5037–5040, 2000.
- [26] A. K. Varoon, S. Steven, D. L. W., K. Daniel, and S. M. S., “Observation of extreme phase transition temperatures of water confined inside isolated carbon nanotubes,” *Nat Nano*, vol. 12, pp. 267–273, mar 2017.
- [27] L. Cabeza, H. Mehling, S. Hiebler, and F. Ziegler, “Heat transfer enhancement in water when used as {PCM} in thermal energy storage,” *Applied Thermal Engineering*, vol. 22, no. 10, pp. 1141–1151, 2002.
- [28] J. L. F. Abascal, E. Sanz, R. G. Fernández, and C. Vega, “A potential model for the study of ices and amorphous water: TIP4P/Ice,” *The Journal of Chemical Physics*, vol. 122, no. 23, p. 234511, 2005.
- [29] R. G. Fernández, J. L. F. Abascal, and C. Vega, “The melting point of ice Ih for common water models calculated from direct coexistence of the solid-liquid interface,” *The Journal of Chemical Physics*, vol. 124, no. 14, p. 144506, 2006.

- [30] J. B. Hasted, *Liquid Water: Dielectric Properties*, pp. 255–309. Boston, MA: Springer New York, 1972.
- [31] D. Eisenberg and W. Kauzmann, *The structure and properties of water*. Oxford University Press on Demand, 1996.
- [32] F. Martin and H. Zipse, “Charge distribution in the water molecule—A comparison of methods,” *Journal of Computational Chemistry*, vol. 26, no. 1, pp. 97–105, 2005.
- [33] F. J. Lovas, “Microwave spectral tables II. Triatomic molecules,” *Journal of Physical and Chemical Reference Data*, vol. 7, no. 4, pp. 1445–1750, 1978.
- [34] W. C. Cmglee, “Phase diagram of water as a log-lin chart with pressure from 1 pa to 1 tpa and temperature from 0 k to 650,” 2017. https://it.wikipedia.org/wiki/file:phase_diagram_of_water.svg.
- [35] Mishima Osamu and Stanley H. Eugene, “The relationship between liquid, supercooled and glassy water,” *Nature*, vol. 396, pp. 329–335, nov 1998. 10.1038/24540.
- [36] C. A. Angell, J. Shuppert, and J. C. Tucker, “Anomalous properties of supercooled water. Heat capacity, expansivity, and proton magnetic resonance chemical shift from 0 to -38%,” *The Journal of Physical Chemistry*, vol. 77, no. 26, pp. 3092–3099, 1973.
- [37] C. Vega, E. Sanz, and J. L. F. Abascal, “The melting temperature of the most common models of water,” *The Journal of Chemical Physics*, vol. 122, no. 11, p. 114507, 2005.
- [38] E. Sanz, C. Vega, J. L. F. Abascal, and L. G. MacDowell, “Phase Diagram of Water from Computer Simulation,” *Phys. Rev. Lett.*, vol. 92, p. 255701, Jun 2004.
- [39] P. H. Poole, F. Sciortino, U. Essmann, and H. E. Stanley, “Spinodal of liquid water,” *Phys. Rev. E*, vol. 48, pp. 3799–3817, Nov 1993.
- [40] C. Vega and J. L F Abascal, “Relation between the melting temperature and the temperature of maximum density for the most common models of water,” vol. 123, p. 144504, 11 2005.
- [41] S. Harrington, P. Poole, F. Sciortino, and H. Stanley, “Equation of state of supercooled water simulated using the extended simple point charge intermolecular potential,” vol. 107, 11 1997.

- [42] H. Kanno and C. Angell, "Water: Anomalous compressibilities to 1.9 kbar and correlation with supercooling limits," *Journal of Chemical Physics*, vol. 70, no. 9, pp. 4008–4016, 1979.
- [43] S. Sastry, P. G. Debenedetti, F. Sciortino, and H. E. Stanley, "Singularity-free interpretation of the thermodynamics of supercooled water," *Phys. Rev. E*, vol. 53, pp. 6144–6154, Jun 1996.
- [44] C. A. Angell, W. J. Sichina, and M. Oguni, "Heat capacity of water at extremes of supercooling and superheating," *The Journal of Physical Chemistry*, vol. 86, no. 6, pp. 998–1002, 1982.
- [45] F. W. Starr, F. Sciortino, and H. E. Stanley, "Dynamics of simulated water under pressure," *Phys. Rev. E*, vol. 60, pp. 6757–6768, Dec 1999.
- [46] H. L. Pi, J. L. Aragones, C. Vega, E. G. Noya, J. L. Abascal, M. A. Gonzalez, and C. McBride, "Anomalies in water as obtained from computer simulations of the TIP4P/2005 model: density maxima, and density, isothermal compressibility and heat capacity minima," *Molecular Physics*, vol. 107, no. 4-6, pp. 365–374, 2009.
- [47] Scala Antonio, Starr Francis W., La Nave Emilia, Sciortino Francesco, and Stanley H. Eugene, "Configurational entropy and diffusivity of supercooled water," *Nature*, vol. 406, pp. 166–169, jul 2000. 10.1038/35018034.
- [48] Errington Jeffrey R. and Debenedetti Pablo G., "Relationship between structural order and the anomalies of liquid water," *Nature*, vol. 409, pp. 318–321, jan 2001. 10.1038/35053024.
- [49] C. A. Angell, E. D. Finch, and P. Bach, "Spin-echo diffusion coefficients of water to 2380 bar and -20° C," *The Journal of Chemical Physics*, vol. 65, no. 8, pp. 3063–3066, 1976.
- [50] F. X. Prielmeier, E. W. Lang, R. J. Speedy, and H.-D. Lüdemann, "Diffusion in supercooled water to 300 MPa," *Phys. Rev. Lett.*, vol. 59, pp. 1128–1131, Sep 1987.
- [51] P. C. Hemmer and G. Stell, "Fluids with several phase transitions," *Phys. Rev. Lett.*, vol. 24, pp. 1284–1287, Jun 1970.
- [52] E. A. Jagla, "Core-softened potentials and the anomalous properties of water," *The Journal of Chemical Physics*, vol. 111, no. 19, pp. 8980–8986, 1999.

- [53] M. R. Sadr-Lahijany, A. Scala, S. V. Buldyrev, and H. E. Stanley, "Liquid-state anomalies and the stell-hemmer core-softened potential," *Phys. Rev. Lett.*, vol. 81, pp. 4895–4898, Nov 1998.
- [54] E. A. Jagla, "Phase behavior of a system of particles with core collapse," *Phys. Rev. E*, vol. 58, pp. 1478–1486, Aug 1998.
- [55] Dudalov D. E., Tsiok E. N., Fomin Yu. D., and Ryzhov V. N., "Effect of a potential softness on the solid-liquid transition in a two-dimensional core-softened potential system," *The Journal of Chemical Physics*, vol. 141, no. 18, p. 18C522, 2014. doi: 10.1063/1.4896825.
- [56] D. E. Dudalov, Y. D. Fomin, E. N. Tsiok, and V. N. Ryzhov, "How dimensionality changes the anomalous behavior and melting scenario of a core-softened potential system?," *Soft Matter*, vol. 10, pp. 4966–4976, 2014.
- [57] J. R. Bordin, A. Diehl, and M. C. Barbosa, "Relation between flow enhancement factor and structure for core-softened fluids inside nanotubes," *The Journal of Physical Chemistry B*, vol. 117, no. 23, pp. 7047–7056, 2013. PMID: 23692639.
- [58] M. Hus and T. Urbic, "Core-softened fluids as a model for water and the hydrophobic effect," *The Journal of Chemical Physics*, vol. 139, no. 11, p. 114504, 2013.
- [59] Sellberg J. A., Huang C., McQueen T. A., Loh N. D., Laksmono H., Schlesinger D., Sierra R. G., Nordlund D., Hampton C. Y., Starodub D., DePonte D. P., Beye M., Chen C., Martin A. V., Barty A., Wikfeldt K. T., Weiss T. M., Caronna C., Feldkamp J., Skinner L. B., Seibert M. M., Messerschmidt M., Williams G. J., Boutet S., Pettersson L. G. M., Bogan M. J., and Nilsson A., "Ultrafast X-ray probing of water structure below the homogeneous ice nucleation temperature," *Nature*, vol. 510, pp. 381–384, jun 2014.
- [60] H. Kanno, R. J. Speedy, and C. A. Angell, "Supercooling of Water to -92°C Under Pressure," *Science*, vol. 189, no. 4206, pp. 880–881, 1975.
- [61] Johari G. P., Hallbrucker Andreas, and Mayer Erwin, "The glass-liquid transition of hyperquenched water," *Nature*, vol. 330, pp. 552–553, dec 1987. 10.1038/330552a0.
- [62] A. Hallbrucker, E. Mayer, and G. P. Johari, "Glass-liquid transition and the enthalpy of devitrification of annealed vapor-deposited amorphous

- solid water: a comparison with hyperquenched glassy water," *The Journal of Physical Chemistry*, vol. 93, no. 12, pp. 4986–4990, 1989.
- [63] V. Velikov, S. Borick, and C. A. Angell, "The Glass Transition of Water, Based on Hyperquenching Experiments," *Science*, vol. 294, no. 5550, pp. 2335–2338, 2001.
- [64] C. A. Angell, "Liquid Fragility and the Glass Transition in Water and Aqueous Solutions," *Chemical Reviews*, vol. 102, no. 8, pp. 2627–2650, 2002. PMID: 12175262.
- [65] T. Loerting, C. Salzmann, I. Kohl, E. Mayer, and A. Hallbrucker, "A second distinct structural," *Phys. Chem. Chem. Phys.*, vol. 3, pp. 5355–5357.
- [66] E. Mayer, "New method for vitrifying water and other liquids by rapid cooling of their aerosols," *Journal of Applied Physics*, vol. 58, no. 2, pp. 663–667, 1985.
- [67] Mishima O., Calvert L. D., and Whalley E., "Melting ice' I at 77 K and 10 kbar: a new method of making amorphous solids," *Nature*, vol. 310, pp. 393–395, aug 1984. 10.1038/310393a0.
- [68] K. Winkel, M. Seidl, T. Loerting, L. E. Bove, S. Imberti, V. Molinero, F. Bruni, R. Mancinelli, and M. A. Ricci, "Structural study of low concentration LiCl aqueous solutions in the liquid, supercooled, and hyperquenched glassy states," *The Journal of Chemical Physics*, vol. 134, no. 2, p. 024515, 2011.
- [69] Poole Peter H., Sciortino Francesco, Essmann Ulrich, and Stanley H. Eugene, "Phase behaviour of metastable water," *Nature*, vol. 360, pp. 324–328, nov 1992. 10.1038/360324a0.
- [70] L. Xu, P. Kumar, S. V. Buldyrev, S.-H. Chen, P. H. Poole, F. Sciortino, and H. E. Stanley, "Relation between the Widom line and the dynamic crossover in systems with a liquid–liquid phase transition," *Proceedings of the National Academy of Sciences of the United States of America*, vol. 102, no. 46, pp. 16558–16562, 2005.
- [71] L. Xu, S. V. Buldyrev, C. A. Angell, and H. E. Stanley, "Thermodynamics and dynamics of the two-scale spherically symmetric Jagla ramp model of anomalous liquids," *Phys. Rev. E*, vol. 74, p. 031108, Sep 2006.

- [72] Mishima Osamu and Stanley H. Eugene, "Decompression-induced melting of ice IV and the liquid-liquid transition in water," *Nature*, vol. 392, pp. 164–168, mar 1998. 10.1038/32386.
- [73] L. Pauling, "The Structure and Entropy of Ice and of Other Crystals with Some Randomness of Atomic Arrangement," *Journal of the American Chemical Society*, vol. 57, no. 12, pp. 2680–2684, 1935.
- [74] B. J. Alder and T. E. Wainwright, "Studies in Molecular Dynamics. I. General Method," *The Journal of Chemical Physics*, vol. 31, no. 2, pp. 459–466, 1959.
- [75] A. Rahman, "Correlations in the Motion of Atoms in Liquid Argon," *Phys. Rev.*, vol. 136, pp. A405–A411, Oct 1964.
- [76] A. Leach, *Molecular Modelling: Principles and Applications*. Pearson Education, Prentice Hall, 2001.
- [77] M. Allen and D. Tildesley, *Computer Simulation of Liquids*. Oxford Science Publ, Clarendon Press, 1989.
- [78] H. J. C. Berendsen, J. P. M. Postma, W. F. van Gunsteren, A. DiNola, and J. R. Haak, "Molecular dynamics with coupling to an external bath," *The Journal of Chemical Physics*, vol. 81, no. 8, pp. 3684–3690, 1984.
- [79] Y. Liu, A. Z. Panagiotopoulos, and P. G. Debenedetti, "Low-temperature fluid-phase behavior of ST2 water," *The Journal of Chemical Physics*, vol. 131, no. 10, p. 104508, 2009.
- [80] N. Narita, S. Nagai, S. Suzuki, and K. Nakao, "Optimized geometries and electronic structures of graphyne and its family," *Phys. Rev. B*, vol. 58, pp. 11009–11014, Oct 1998.
- [81] A. K. Gupta, T. J. Russin, H. R. Gutiérrez, and P. C. Eklund, "Probing Graphene Edges via Raman Scattering," *ACS Nano*, vol. 3, no. 1, pp. 45–52, 2009.
- [82] Qin Lu-Chang, Zhao Xinluo, Hirahara Kaori, Miyamoto Yoshiyuki, Ando Yoshinori, and Iijima Sumio, "Materials science: The smallest carbon nanotube," *Nature*, vol. 408, pp. 50–50, nov 2000. 10.1038/35040699.
- [83] C. W. Bauschlicher, "High Coverages of Hydrogen on a (10,0) Carbon Nanotube," *Nano Letters*, vol. 1, no. 5, pp. 223–226, 2001.

- [84] G. A. Kaminski, R. A. Friesner, J. Tirado-Rives, and W. L. Jorgensen, "Evaluation and Reparametrization of the OPLS-AA Force Field for Proteins via Comparison with Accurate Quantum Chemical Calculations on Peptides," *The Journal of Physical Chemistry B*, vol. 105, no. 28, pp. 6474–6487, 2001.
- [85] M. J. Abraham, T. Murtola, R. Schulz, S. Páll, J. C. Smith, B. Hess, and E. Lindahl, "GROMACS: High performance molecular simulations through multi-level parallelism from laptops to supercomputers," *SoftwareX*, vol. 1–2, pp. 19–25, 2015.
- [86] Best Robert B. and Hummer Gerhard, "Reaction coordinates and rates from transition paths," *Proceedings of the National Academy of Sciences of the United States of America*, vol. 102, pp. 6732–6737, may 2005.
- [87] M. D. Marzio, G. Camisasca, M. M. Conde, M. Rovere, and P. Gallo, "Structural properties and fragile to strong transition in confined water," *The Journal of Chemical Physics*, vol. 146, no. 8, p. 084505, 2017.
- [88] P. Gallo, M. A. Ricci, and M. Rovere, "Layer analysis of the structure of water confined in vycor glass," *The Journal of Chemical Physics*, vol. 116, no. 1, pp. 342–346, 2002.
- [89] U. Bergmann, A. Di Cicco, P. Wernet, E. Principi, P. Glatzel, and A. Nilsson, "Nearest-neighbor oxygen distances in liquid water and ice observed by x-ray Raman based extended x-ray absorption fine structure," *The Journal of Chemical Physics*, vol. 127, no. 17, p. 174504, 2007.
- [90] X. Qin, Q. Yuan, Y. Zhao, S. Xie, and Z. Liu, "Measurement of the Rate of Water Translocation through Carbon Nanotubes," *Nano Letters*, vol. 11, no. 5, pp. 2173–2177, 2011. PMID: 21462938.
- [91] K. P. Jensen and W. L. Jorgensen, "Halide, Ammonium, and Alkali Metal Ion Parameters for Modeling Aqueous Solutions," *Journal of Chemical Theory and Computation*, vol. 2, no. 6, pp. 1499–1509, 2006. PMID: 26627020.
- [92] B. Hess, C. Kutzner, D. van der Spoel, and E. Lindahl, "GROMACS 4: Algorithms for Highly Efficient, Load-Balanced, and Scalable Molecular Simulation," *Journal of Chemical Theory and Computation*, vol. 4, no. 3, pp. 435–447, 2008. PMID: 26620784.

- [93] P. Gallo, D. Corradini, and M. Rovere, “Ion hydration and structural properties of water in aqueous solutions at normal and supercooled conditions: a test of the structure making and breaking concept,” *Phys. Chem. Chem. Phys.*, vol. 13, pp. 19814–19822, 2011.
- [94] R. W. Impey, P. A. Madden, and I. R. McDonald, “Hydration and mobility of ions in solution,” *The Journal of Physical Chemistry*, vol. 87, no. 25, pp. 5071–5083, 1983.
- [95] L. M. Ramaniah, M. Bernasconi, and M. Parrinello, “Ab initio molecular-dynamics simulation of K^+ solvation in water,” *The Journal of Chemical Physics*, vol. 111, no. 4, pp. 1587–1591, 1999.
- [96] M. M. Conde, M. Rovere, and P. Gallo, “Spontaneous NaCl-doped ice at seawater conditions: focus on the mechanisms of ion inclusion,” *Phys. Chem. Chem. Phys.*, vol. 19, pp. 9566–9574, 2017.